

UNIVERSITÀ DI NAPOLI “FEDERICO II”  
INTERNATIONAL PHD  
IN  
*Novel Technologies for Materials, Sensors and Imaging*  
XXIII CYCLE



Development and test of sensors and actuators  
to control a Michelson interferometer  
suspended by means of a multipendular system

**Supervisor**

Prof. Rosario De Rosa

**Author**

Gianluca Persichetti

# Contents

<b>Introduction</b>	<b>1</b>
<b>1 Gravitational Wave Detection</b>	<b>3</b>
1.1 Gravitational Waves . . . . .	3
1.2 Generation of Gravitational Waves . . . . .	6
1.3 Sources of Gravitational Waves . . . . .	7
1.3.1 Coalescing binaries . . . . .	8
1.3.2 Spinning Neutron Stars (Pulsars) . . . . .	8
1.3.3 Supernovae . . . . .	10
1.3.4 Gamma Ray Burst . . . . .	11
1.3.5 Stochastic Background . . . . .	11
1.4 Detection of Gravitational Waves . . . . .	12
<b>2 The Seismic Attenuation System</b>	<b>17</b>
2.1 Ground vibrations . . . . .	17
2.1.1 Seismic noise . . . . .	18
2.1.2 Newtonian noise . . . . .	18
2.1.3 Seismic attenuation . . . . .	19
2.2 The inverted pendulum . . . . .	22
2.3 Mechanical description of the inverted pendulum . . . . .	23
2.4 Inverted pendulum with counterweight . . . . .	26
2.5 Vertical attenuation system . . . . .	29
2.6 Control strategies . . . . .	32
2.7 Sensors and actuators system . . . . .	32
2.7.1 LVDT . . . . .	33
2.7.2 Magnet coil actuators . . . . .	36
2.7.3 Accelerometers . . . . .	38
<b>3 Diagonalization procedure</b>	<b>40</b>
3.1 Introduction . . . . .	40
3.2 The diagonalization method . . . . .	41

3.3	Sensors and actuators on simple pendulum . . . . .	45
3.4	The diagonalization results . . . . .	45
<b>4</b>	<b>Control design</b>	<b>51</b>
4.1	Transfer function measurements . . . . .	51
4.2	The control design . . . . .	53
4.3	Sensor blending . . . . .	54
<b>5</b>	<b>Mechanics of the accelerometer</b>	<b>61</b>
5.1	Folded pendulum . . . . .	62
5.1.1	Potential energy of a folded pendulum . . . . .	67
5.2	Realistic folded pendulum mechanical model . . . . .	69
5.2.1	Stiffness contribution . . . . .	69
5.2.2	Tuning mass contribution . . . . .	71
5.3	Mechanical design . . . . .	75
5.3.1	Gap opening . . . . .	75
5.3.2	Material choice . . . . .	76
5.3.3	Elliptical hinges . . . . .	76
<b>6</b>	<b>Accelerometer performances</b>	<b>83</b>
6.1	Optical readout . . . . .	83
6.2	Preliminary measurements . . . . .	85
6.3	Sensitivity curve . . . . .	88
6.3.1	Thermal noise . . . . .	88
6.3.2	Optical noise . . . . .	89
6.3.3	Electronic noise . . . . .	91
6.4	Measurements at atmospheric pressure . . . . .	92
6.4.1	Monolithic FP sensor as <i>seismometer</i> . . . . .	92
6.4.2	Monolithic FP sensor as <i>accelerometer</i> . . . . .	94
6.5	Measurements in vacuum . . . . .	97
6.5.1	Internal quality factor in a folded pendulum . . . . .	97
6.5.2	Folded pendulum and internal and external damping in coexistence . . . . .	97
6.5.3	Quality factor measurements . . . . .	98
<b>7</b>	<b>Electrostatic actuators</b>	<b>101</b>
7.1	Magnet-coil actuation drawbacks . . . . .	101
7.2	Electrostatic actuation . . . . .	103
7.2.1	Electrostatic actuator model . . . . .	105
7.2.2	Stray charge contribution . . . . .	106
7.2.3	Bias modulation technique . . . . .	106

7.3	Characterization of electrostatic actuators in air . . . . .	108
7.4	Characterization of electrostatic actuators in high vacuum . .	111
7.5	Spurious charge detection technique . . . . .	116
7.6	EA application on suspended Michelson interferometer control	119
<b>Conclusions</b>		<b>122</b>
<b>A Viscous and internal damping</b>		<b>125</b>
A.1	Viscous damping . . . . .	126
A.2	Internal damping . . . . .	127
A.3	Internal and external damping . . . . .	128
<b>B Optical levers</b>		<b>130</b>
<b>Acknowledgments</b>		<b>135</b>
<b>Bibliography</b>		<b>136</b>

# Introduction

The purpose of the VIRGO experiment is to detect gravitational waves produced by astrophysical sources in a frequency range between 10 Hz and some KHz. VIRGO is the unique interferometric detector devoted to detect signals below 50 Hz and one of its main goals is to extend the low frequency detection threshold down to a few Hz (to enlarge the potentially detectable sources number). In this frequency range, the seismic noise limits the detector sensitivity. One of the most efficient Seismic Attenuation System (**SAS**) for gravitational waves interferometers is a chain of pendula suspended from a very low-frequency stage called Inverted Pendulum.

Each optical component of the interferometer is supported by means of this particular suspension system. In the Naples VIRGO laboratory a simplified prototype of this interferometric detector will be soon available.

It is a 3 m arm long interferometer and it will make possible to develop and test new sensors and actuators as to design new control system to be adopted by the VIRGO interferometer.

The aim of this work is strictly connected to the building of this prototype and to test and develop innovative sensors and actuators which equipped the seismic attenuation system. All the sensors and actuators are special purpose devices and no commercial devices are available with same features.

In order to show the framework at which this research activity is related, in *Chapter 1* gravitational waves and the interferometric detection principle will be illustrated. In the same chapter, a brief list of potentially detectable sources will be described.

The seismic attenuation system will be the topic of *Chapter 2*. Its necessity will be explained as the elements of this particular structure will be described. Sensors and actuators employed in order to control the seismic attenuation system will be also described in the same chapter.

An original experimental procedure for determining the attenuation system diagonalization (i.e. the disentanglement of its normal modes) will be defined in *Chapter 3*. Preliminary test has been performed on a different physical system in order to validate the procedure.

Besides the vibration isolation offered by the seismic attenuation system, the residual motion of the optical elements composing the interferometer and of the elements of the pendula chain have to be damped. For this purpose a feedback system, using inertial sensors (accelerometers) and position sensors has been designed.

Taking advantage from the original diagonalization procedure, it has been possible to design a digital control system, illustrated in *Chapter 4*, able to satisfy the characteristics required.

To improve feedback control system performance and more generally the whole interferometric gravitational waves detector, new monolithic accelerometers has been developed.

The mechanics of this sensor is explained in *Chapter 5* where models useful to describe its characteristics are also illustrated.

Those innovative sensors, shaped with electric-discharge-machining are characterized by a new design with respect the model presently used in our laboratory.

The monolithic mechanical design has the great advantage of avoiding the shear effects at the contact surface among mechanical parts that can generate hysteresis and dissipation in a non monolithic structure increasing the sensor mechanical performances.

The same mechanical structure of this device can find two different employment: as accelerometer and seismometer.

In both of the configuration, a characterization of this sensors is showed in *Chapter 6*.

One of the most important parameter to determine the performance of this sensor is the mechanical quality factor. To this purpose, a vacuum chamber has been set up and mechanical quality factor measurements has been performed on different accelerometers model.

Another parameter which determines the overall performance is the frequency resonance. The accelerometers are expressly designed to change this frequency because of the presence of a tuning mass. The measurements have shown very low frequency resonance values.

Electrostatic actuators (EA) are one of the most promising devices for mirror control in advanced gravitational waves detectors. The designing of an innovative actuation system have to satisfy the requirement of the control system, both in term of low noise content as well as to fit the required dynamical range. To accomplish this task an accurate characterization of such actuators has been performed. This is the topic of *Chapter 7* where it will be described the technique employed to drive this actuators and the very promising results found.

# Chapter 1

## Gravitational Wave Detection

One of the most fascinating consequences of the General Theory of Relativity is the coupling between mass and the geometry of space. This connection leads to the prediction that changes in the mass distribution can produce a perturbation of the geometry which propagates through space like a wave. These ripples in spacetime, are called *gravitational waves*. They propagate at the speed of light and carry with them information about the dynamics of those cosmological objects that created them.

The detection of gravitational waves has the potential for an alternative type of astronomy, complementing the conventional optical, infrared, radio and x-ray astronomy.

In the following we will describe briefly the theory of the gravitational waves, referring the reader to [1] and [2] for details.

### 1.1 Gravitational Waves

A fundamental concept express in the Special Theory of Relativity is that the *space time interval*  $ds$  between any two neighboring points is given by the expression:

$$ds^2 = -c^2 dt^2 + dx^2 + dy^2 + dz^2 \quad (1.1)$$

or

$$ds^2 = \eta_{\mu\nu} dx^\mu dx^\nu \quad (1.2)$$

where  $\eta_{\mu\nu}$  is the Minkowski metric which, in Cartesian coordinates, can be written as:

$$\eta_{\mu\nu} = \begin{pmatrix} -1 & 0 & 0 & 0 \\ 0 & -1 & 0 & 0 \\ 0 & 0 & -1 & 0 \\ 0 & 0 & 0 & 1 \end{pmatrix}$$

In the General Theory of Relativity *space-time* is no longer necessarily *flat* as happens in the Minkowski metric. The *space-time* will be in general curved and the curvature represents the *gravitation*.

A more general definition of *space-time* interval will be:

$$ds^2 = g_{\mu\nu} dx^\mu dx^\nu \quad (1.3)$$

where the metric  $g_{\mu\nu}$  carry all the information about *space-time* curvature.

The structure and the evolution of metric tensor  $g_{\mu\nu}$  are regulated by the Einstein field equations, which determine the  $g_{\mu\nu}$  tensor and its derivatives as a function of the impulse-energy tensor of matter  $T_{\mu\nu}$ :

$$R_{\mu\nu} - \frac{1}{2}g_{\mu\nu}R = \frac{8\pi G}{c^4}T_{\mu\nu} \quad (1.4)$$

where  $R_{\mu\nu}$  is the Ricci tensor: contraction over two indices of the Riemann tensor  $R_{\mu\nu\rho\sigma}$  ( $R_{\mu\nu} = g^{\rho\sigma}R_{\mu\nu\rho\sigma}$ )  $G$  is the Newton's gravity constant and  $R$  is the scalar curvature  $R = g^{\mu\nu}R_{\mu\nu}$ , contraction of the Ricci tensor. These equations are non linear and in the general case cannot be analytically solved. In vacuum ( $T_{\mu\nu} = 0$ ), the Einstein equation is simplified as:

$$R_{\mu\nu} - \frac{1}{2}g_{\mu\nu}R = 0 \quad (1.5)$$

The General Theory of Relativity contains the Special Relativity and then the Minkowski metric  $\eta_{\mu\nu}$  represents a particular solution of the above equation (1.5).

The Gravitational Waves are extremely weak, for this reason, in the following we will consider only a simple case of the (1.3) the one in which there is only a small perturbation in a flat *space-time*. In this case the metric  $g_{\mu\nu}$  can be written as:

$$g_{\mu\nu} = \mu_{\mu\nu} + h_{\mu\nu} \quad (1.6)$$

in which  $h_{\mu\nu}$  is the metric perturbation with respect to the flat Minkowski space.

To the first order, with respect to  $h_{\mu\nu}$ , the field equations are linear. With a suitable choice of gauge (harmonic gauge) Einsteins equations assume the familiarly form of a wave equations:

$$(\nabla^2 - \frac{1}{c^2} \frac{\partial^2}{\partial t^2})h_{\mu\nu} = 0 \quad (1.7)$$

which describe the perturbation  $h_{\mu\nu}$  as a wave propagating at speed  $c$  or, in other words, a Gravitational Wave. The freedom in the choice of the coordinate system can be used again to impose the tensor  $\mathbf{h}$  to be transverse and traceless (*TT gauge*)<sup>1</sup>.

Let  $\hat{z}$  be the propagation direction, the statement that  $\mathbf{h}$  has to be transverse and traceless means that it has the form [3]:

$$\mathbf{h} = \begin{pmatrix} 0 & 0 & 0 & 0 \\ 0 & a & b & 0 \\ 0 & b & -a & 0 \\ 0 & 0 & 0 & 0 \end{pmatrix}$$

and this means also that we can write the wave as a sum of two components  $h = ah_+ + bh_\times$  where:

$$h_+ = \begin{pmatrix} 0 & 0 & 0 & 0 \\ 0 & 1 & 0 & 0 \\ 0 & 0 & -1 & 0 \\ 0 & 0 & 0 & 0 \end{pmatrix}$$

and

$$h_\times = \begin{pmatrix} 0 & 0 & 0 & 0 \\ 0 & 0 & 1 & 0 \\ 0 & 1 & 0 & 0 \\ 0 & 0 & 0 & 0 \end{pmatrix}$$

The tensors  $\hat{h}_+$  and  $\hat{h}_\times$  ("h plus" and "h cross") are two orthogonal polarization states for a gravitational wave travelling along the  $\hat{z}$  direction. They represent a basis in which is possible to decompose a generic gravitational wave.

In the figure (1.1) it is shown how two components of the gravitational wave act on a circle of "free falling" masses. The effect of  $\hat{h}_+$  is the alternately stretching and contracting of the distances along  $x$  and  $y$  direction. The effect of  $\hat{h}_\times$  is similar but with a rotation of  $\frac{\pi}{4}$ .

---

<sup>1</sup>In this gauge the coordinates are marked by the world lines of freely falling masses, that is, the coordinates of freely falling test masses are constant.

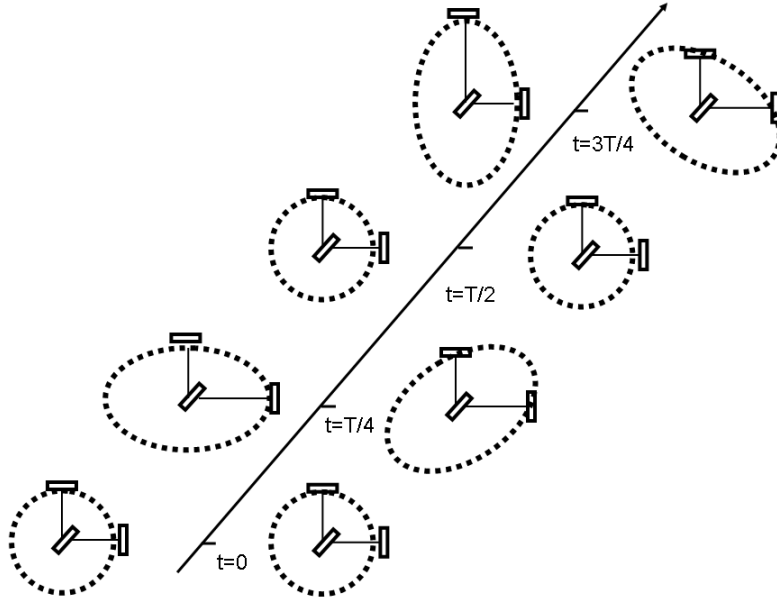


Figure 1.1: Effect of a Gravitational Wave on a ring of masses in case of plus polarized and cross polarized wave.

## 1.2 Generation of Gravitational Waves

The formal analogy between Newton's law of gravitation and Coulomb's law suggests the chance of developing the gravitational radiation in a multipolar expansion, as it happens in electrodynamics. For instance, it is possible defining a gravitational dipole moment as [3]:

$$d_g = \int dV \rho(r)r \quad (1.8)$$

where  $\rho(r)$  is the mass density of the source and  $r$  is the distance from the origin. However the equivalence between inertial mass and gravitational mass requires the classical mechanics conservation laws. In any isolate system the quantity  $\dot{d}_g$ , which represents the momentum, has to remains constant. For this reason, no radiation can be associated to this mass distribution moment. The first term able to generate gravitational waves is the quadrupole moment. In a typical case, where motions within the source can be considered slow compared with the speed of light, it can be written as:

$$I_{\mu\nu} \equiv \int dV (x_\mu x_\nu - \frac{1}{3} \delta_{\mu\nu} r^2) \rho(r) \quad (1.9)$$

The expression (1.9) shows that quadrupole momentum is proportional to the mass source but also depends on the asymmetry of its density:  $I_{\mu\nu}$  has components different from zero only if its mass distribution is different from the spherical one.

It is possible to show [3] that the field amplitude associated to the (1.9) in the TT gauge is:

$$h_{\mu\nu} = \frac{2G}{rc^4} \ddot{I}_{\mu\nu} \quad (1.10)$$

where the right hand side is evaluated at the retarded time  $(t - \frac{r}{c})$  with  $r$  the distance from the source.

A rough estimation of  $h$  can be obtained considering the case of a binary star. As we will see in the next subsection, they are one of the most promising gravitational wave sources. For simplicity's sake let consider a circular motion characterized by a radius  $r_0$ , a frequency  $f_{orb}$  and the same mass  $M$  for both components.

Applying (1.9) and (1.10) we get:

$$h_{xx} = -h_{yy} = \frac{32\pi^2 G}{Rc^4} M_0^2 f_{orb}^2 \cos[2(2\pi f_{orb})t] \quad (1.11)$$

$$h_{xy} = -h_{yx} = -\frac{32\pi^2 G}{Rc^4} M_0^2 f_{orb}^2 \sin[2(2\pi f_{orb})t] \quad (1.12)$$

Taking into account that  $f_{orb}^2 = \frac{GM}{16\pi^2 r_0^3}$  reordering (1.11) and (1.12) we obtain [3] an estimation of  $h$ :

$$|h| \sim \frac{r_{s1} r_{s2}}{r_0 R} \quad (1.13)$$

where  $r_{s1} = r_{s2} = \frac{2GM}{c^2}$  are the Schwarzschild radii of the two stars. Using typical values for a binary system constituted by neutron stars ( $M \sim 1.4M_\odot$ ,  $f_{orb} \sim 400Hz$ ,  $r_0 = 20Km$ ), located in the galaxy cluster closest to the Earth (Virgo,  $R \sim 18Mpc$ ), we obtain:

$$|h| \sim 10^{-21} \quad (1.14)$$

### 1.3 Sources of Gravitational Waves

As underlined as a comment of equation (1.9) the amplitude of a gravitational wave is not zero only if there is an asymmetry in the mass distribution of the source. For this reason, each source briefly described in the following will have such a characteristic.

Depending on their emitted wave forms, the sources of gravitational waves can be classified in three categories:

- Periodic sources: coalescing binaries, spinning neutron stars (pulsars).
- Impulsive sources: supernovae, gamma ray bursts.
- Stochastic sources: cosmological background, white dwarf binaries.

### 1.3.1 Coalescing binaries

Coalescing binaries are binary systems constituted by very compact objects, as neutron stars or black holes, that lose energy emitting gravitational radiation. Their orbital period constantly decreases and, after a time  $\tau_c$ , called coalescing time, they eventually merge. Among all gravitational wave sources, the coalescing binaries are the ones the scientific community looks at with more confidence.

A well known example is *PSR1913 + 16*: their observation furnished an indirect proof of Gravitational Waves existence. In the 1974 Russel Hulse and Joseph Taylor, using the Arecibo 305m antenna, observed pulsed radio emission. They identified such emission as coming from a neutron star bound to a dark companion in a binary system [4].

After more than 20 years of observations (see figure (1.2)), data collected was useful to test General Relativity to an high level of accuracy [5].

For this reason Hulse and Taylor were awarded the 1993 Nobel Prize in Physics: "*for the discovery of a new type of pulsar, a discovery that has opened up new possibilities for the study of gravitation*".

### 1.3.2 Spinning Neutron Stars (Pulsars)

Spinning neutron stars, like pulsars, are expected to be the main sources of continuous gravitational radiation, which are long-lasting, quasi-monochromatic Gravitational Waves with slowly varying frequency. Although current models of stellar evolution predict the presence of approximately  $10^9$  neutron stars in our galaxy, of which  $10^5$  are expected to be spinning and actively emitting radiation, only about 1700 pulsars have been observed so far. This is due to the high variability in the intensity of the generated radiation.

Three mechanism are usually considered for gravitational Waves emission from pulsars:

- *Non-axisymmetric distortions of the neutron star.* Magnetic fields or elastic tension of the pulsar's crust can generate deformations on its

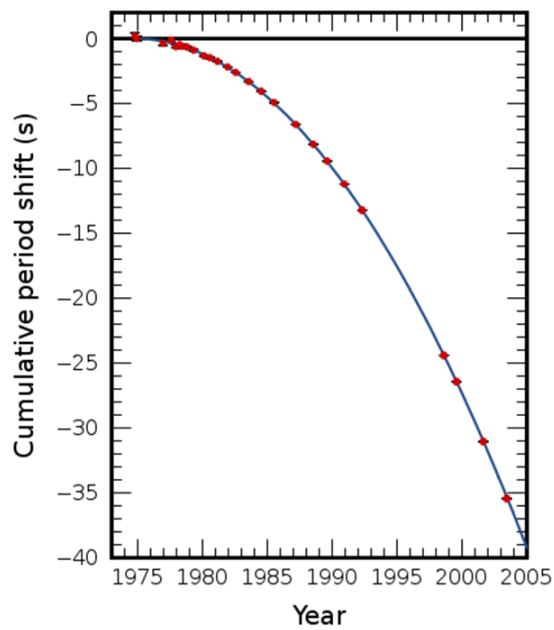


Figure 1.2: Orbital decay of PSR B1913+16 [5]. The data points indicate the observed change in the epoch of periastron with date while the curve shows the theoretically expected change in epoch for a system emitting gravitational radiation, according to general relativity.

surface, called mountains, that are asymmetric with respect to the rotation axis. Considering a star with inertia tensor  $I_{ij}$ , spinning at frequency  $\nu$ , the pulsar will generate monochromatic waves with frequency  $2\nu$  and amplitude:

$$h = \frac{16\pi^2 G I_{zz} \nu^2}{c^4 d} \epsilon \quad (1.15)$$

where  $d$  is the distance from the Earth and  $\epsilon = \frac{I_{xx} - I_{yy}}{I_{zz}}$  is a parameter, called equatorial ellipticity, that express the star deformation. The range of possible values of  $\epsilon$  is presently very uncertain.

- *Unstable oscillation modes in the fluid part of the star.* Spinning neutron stars can be subject to non-axisymmetric instabilities, during their birth and accretion phase, a period in which the star is growing gravitationally attracting matter from an other body. These instabilities can be divided in two broad categories depending on their timescales: dynamic and secular. In the first case the unstable modes grows in a time comparable with the oscillation period, while in the second the growth is much longer.
- *Free precession.* The neutron star rotation axis is misaligned whit respect to its symmetry axis forming an angle  $\theta_\omega$ . For a star at a distance  $d$  from the Earth and rotating at frequency  $\nu$  it is possible to write:

$$h = 10^{-27} \left( \frac{\theta_\omega}{0.1 rad} \right) \left( \frac{1 kpc}{d} \right) \left( \frac{\nu}{500 Hz} \right) \quad (1.16)$$

The gravitational radiation is emitted at the three frequencies  $f_1 = \nu + \nu_{prec}$ ,  $f_2 = 2\nu$ ,  $f_3 = 2\nu + 2\nu_{prec}$ , where  $\nu_{prec}$  is the precession rate, with decreasing amplitude. While the first and third frequencies emissions are caused by the precession, the second oscillation is caused by the star deviation from axisymmetry in an analogous way as we have seen before.

### 1.3.3 Supernovae

When a massive star begin to finish their nuclear fuel, it can not be any more able to sustain its own gravity. The subsequent explosion of the star originates what it is called a *supernova*.

The star core collapsing generates a shockwave responsible of the external shell expulsion. This expulsion occurs with a huge electromagnetic emission but the gravitational radiation is emitted because of the core collapsing.

Several years ago, the supernovae were considered as the most easily detectable gravitational wave sources. Nowadays it is known that their emission intensity could vary considerably depending on the stellar mass percentage that is converted in radiation and by the type of symmetry of the collapse itself. The expected rate for these events is between 1/30 years and 1/40 years per galaxy. The Virgo cluster, that is around  $18Mpc$  distant and constituted by about 2000 galaxies, could therefore generate a rate of several events per year.

### 1.3.4 Gamma Ray Burst

Gamma ray bursts are intense flashes of  $\gamma$  rays which occur approximately once per day and are isotropically distributed over the sky. Their time scale variability is ranging from a millisecond to several seconds. Such a variability indicates that the sources are very compact and their measured red shifts have shown that they are generated outside our galaxy.

It is possible to divided Gamma Ray Bursts in two broad classes depending on their duration:

- *Short burst* ( $\lesssim 2s$ ), that are thought to be caused by merging of binaries as *neutron star/neutron star* or *black hole/black hole*.
- *Long events* ( $\gtrsim 2s$ ) probably associated with the core collapse of supernovae.

As we have seen, the emission of gravitational radiation is expected in both scenarios. Although, no experimental evidence of gravitational wave emission associated with Gamma Ray Bursts has been found yet, upper limits have been recently given for several events [7].

### 1.3.5 Stochastic Background

The stochastic gravitational radiation is foreseen by many present cosmological models. This radiation consists on many individual components which are randomly superimposed and some of its components were produced during the early expansion of the universe. The stochastic background detection could have extraordinary impact on cosmology and high-energy physics: it should carry unique signatures from the earliest epochs in the evolution of the Universe, currently inaccessible to standard astrophysical observations. Recently, an upper limit on the amplitude of the stochastic gravitational wave background has been set by using the data from a two-year science run of the Laser Interferometer Gravitational-wave Observatory [8].

## 1.4 Detection of Gravitational Waves

The first experiments for gravitational wave detection was performed in the 1960's by J.Weber using two resonant bars.

His idea was to measure the normal modes of oscillation of a cylindrical metal mass, cooled at cryogenic temperatures, using extremely sensitive magnetic sensors.

Even though Weber's claims, detections using resonant bars have never been confirmed. Nowadays, the highest expectations of the scientific community are for another kind of instrument: the Michelson interferometer.

A Michelson interferometer is an instrument sensitive to very small changes in the distances between its mirrors. The mirrors can ideally be used as proof masses, while the distance variation between them is measured very accurately through interference of laser light. The working principle of interferometric gravitational wave antennas is to set the mirrors in a condition as close as possible to free fall, minimizing all not-gravitational perturbations, in order to detect a gravitational wave as a phase variation of the interference pattern of the interferometer. This requires extremely complex and sophisticated technology but this will be the topic of a next chapter.

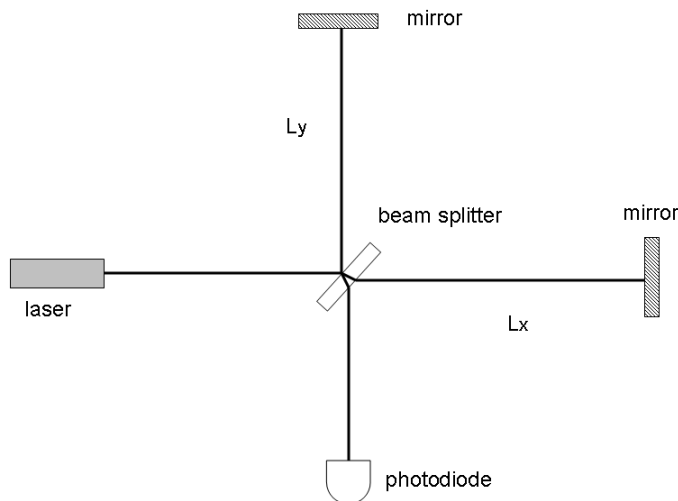


Figure 1.3: Outline of a Michelson interferometer.

In the figure (1.3) a Michelson interferometer is sketched. A laser beam is emitted and split at the surface of the beam splitter into two orthogonal

directions. At the end of each arm, a mirror reflects the beam back to the beam splitter. The two reflected beams recombine and interfere on the beam splitter surface. A photodetector will give the signal output of the interferometer.

Let's now describe the effects of a gravitational wave on a Michelson interferometer with its arms aligned along  $\hat{x}$  and  $\hat{y}$  axes with the beam splitter placed at the origin.

It is known that light connects only events in the space-time that are separated by a null interval. This means  $ds^2 = 0$ . Since the paths followed by the light in each arm will have only either  $dx$  or  $dy$  non-zero, we will only consider the 11 and 22 components of  $h$  (along with the trivial component 00).

Considering light in the arm along the  $\hat{x}$ -axis and setting the (1.3) equal to zero we obtain:

$$\begin{aligned} ds^2 &= g_{\mu\nu} dx^\mu dx^\nu = \\ &= (\eta_{\mu\nu} + h_{\mu\nu}) dx^\mu dx^\nu = \\ &= -c^2 dt^2 + \left(1 + h_{11}(2\pi f_{gw} t - \vec{k} \cdot \vec{x})\right) dx^2 = 0 \end{aligned} \quad (1.17)$$

which shows as the effect of wave is to modulate the distance between two neighboring points with separation  $dx$  by a fractional amount  $h_{11}$ .

We can evaluate the time the light takes to travel from the beam splitter to the end of the  $\hat{x}$  arm, integrating the square root of the previous expression:

$$\tau_x^{(1)} = \int_0^{t_1} dt = \frac{1}{c} \int_0^L \sqrt{1 + h_{11}} dx \approx \frac{1}{c} \int_0^L \left(1 + \frac{1}{2} h_{11}\right) dx \quad (1.18)$$

where we expanded the square root at first order, since we will consider only situation in which  $h \ll 1$ . In a similar way the return trip can be written as:

$$\tau_x^{(2)} \approx -\frac{1}{c} \int_L^0 \left(1 + \frac{1}{2} h_{11}\right) dx \quad (1.19)$$

The resulting total time will be:

$$\tau_x = \tau_x^{(1)} + \tau_x^{(2)} \quad (1.20)$$

Therefore taking into account (1.18) and (1.19):

$$\tau_x = \frac{2L}{c} + \frac{1}{2c} \int_0^L h_{11} dx - \frac{1}{2c} \int_L^0 h_{11} dx \quad (1.21)$$

If we consider the simplest case of a sinusoidal wave propagating along the  $\hat{z}$  axis, with frequency  $f_{gw}$ , polarization  $+$  and amplitude  $h_{11} = -h_{22} = h_0$ . The two integrals in the previous (1.21) can be easily calculated, by calling  $h(t) = h_0 e^{i2\pi f_{gw} t}$  and remembering that  $t = \frac{x}{c}$  in the (1.18) and  $t = \frac{2L-x}{c}$  in the (1.19). The total time  $\tau_x$  will be:

$$\tau_x = \tau_0 + \frac{h_0}{4\pi i f_{gw}} \left[ e^{i2\pi f_{gw} \tau_0} - 1 \right] \quad (1.22)$$

where  $\tau_0 = \frac{2L}{c}$  is the classical round trip time.

In a very similar way it is possible to consider photons travelling along the  $\hat{y}$  direction (the other interferometer arm). The corresponding expression of the photons time of flight will be the same but depending on  $h_{22}$  instead of  $h_{11}$ .

$$\tau_y = \tau_0 - \frac{h_0}{4\pi f_{gw}} \left[ e^{i2\pi f_{gw} \tau_0} - 1 \right] \quad (1.23)$$

From the observer point of view in a laboratory reference frame this difference in the travel time with respect to the classical time  $\tau_0 = \frac{2L}{c}$  can be interpreted as a variation of the interferometer arm lengths,  $L_x$  and  $L_y$ :

$$L_x = \frac{1}{2} c \tau_x = L \left( 1 + \frac{h(t)}{2} \right) \quad (1.24)$$

$$L_y = \frac{1}{2} c \tau_y = L \left( 1 - \frac{h(t)}{2} \right) \quad (1.25)$$

When the two waveforms arrive to the the beam splitter they are thus *out of sync* and a photodiode at the output of the interferometer would measure a time difference:

$$\Delta\tau(t) = h(t) \tau_0 e^{i\pi f_{gw} \tau_0} \frac{\sin(\pi f_{gw} \tau_0)}{\pi f_{gw} \tau_0} \quad (1.26)$$

which corresponds to a phase variation on the output port of the interferometer:

$$\delta\phi(t) = \frac{4\pi L}{\lambda} h(t) e^{i\pi f_{gw} \tau_0} \text{sinc}(\pi f_{gw} \tau_0) \quad (1.27)$$

where  $\lambda$  is the laser wavelength and  $\text{sinc}(x) = \frac{\sin(x)}{x}$ . From the above description it is clear that an interferometer can be used as a gravitational wave detector.

The interferometer response is plotted in figure (1.4) as a function of the impinging gravitational wave frequency  $f_{gw}$ . Those plots shows that the

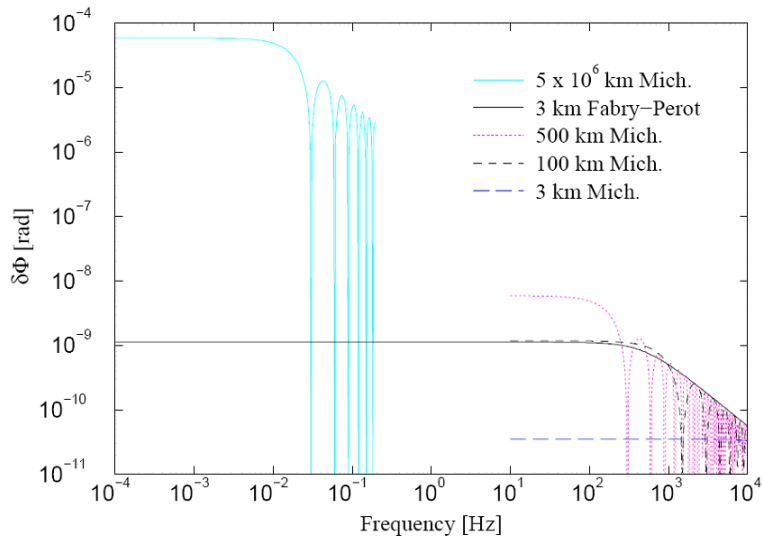


Figure 1.4: Phase response of an interferometer to gravitational waves of fixed amplitude  $10^{-21}$ , for different lengths of the arms. In the figure is also shown that the performance of a 3 km FabryPerot interferometer like VIRGO (FabryPerot cavities are used to increase the photons optical path) is comparable to that of a 100 km Michelson and the response of a  $5 \cdot 10^6$  long Michelson (like the forthcoming space interferometer LISA [9]). In any case the phase shift increases with increasing arms length, at the cost of a bandwidth reduction.

interferometer acts as a low pass filter which starts attenuating at frequencies  $f \sim \frac{c}{2L}$ , that is when the period of the wave is comparable to the travel time  $\tau_0$ .

In the low frequency range where  $f_{gw}\tau_0 \ll 1$  the interferometer response is flat and can be approximated as:

$$\delta\phi(t) = \frac{4\pi L}{\lambda}h(t) \quad (1.28)$$

The latter equation shows straightforwardly that the longer the arms of the interferometer, the bigger the phase shift due to a gravitational wave.

In the low frequency approximation the (1.24) and (1.25) can be used to obtain the "arm length variation" measured in the laboratory frame:

$$\delta x(t) = \frac{L}{2}h(t) \quad (1.29)$$

$$\delta y(t) = \frac{L}{2}h(t) \quad (1.30)$$

For an interferometer 1 Km long, assuming  $h \sim 10^{-21}$ , this variation is  $\delta x(t) \sim 10^{-18}m!$

## Chapter 2

# The Seismic Attenuation System

The seismic vibrations of the ground are many order of magnitude greater than the displacements needed to detect gravitational waves. For this reason a very efficient seismic attenuation system is required.

At the same time a quasi-inertial frame should be provided for the test masses in order to consider them as in a free fall condition as required in the Chapter 1.

In the present Chapter it will be shown that both of those requirements could be provided suspending the optical components of the Michelson interferometer by means of a mechanical structure.

### 2.1 Ground vibrations

Ground motion is a noise source for interferometers built on the Earth's crust. Typical sources are natural phenomena like tectonic motions of the earth's crust, storms, wind and water in motion (including ocean waves) and artificial sources such as traffic, machinery and general industrial activity as well as the human activities.

But there are two way in which this disturbances can affect the interferometer performance: a direct mechanical connection between optical components and ground (*seismic noise*) and a local fluctuation of the gravitational field (*Newtonian noise*).

### 2.1.1 Seismic noise

The signal of an interferometer is disturbed by the continuous and random ground motion: *the seismic noise*. The ground motion transmitted through the mechanical connection between the ground and the test masses results in perturbations of the test masses separation.

Obviously with such a wide variety of potential noise sources, the level of seismic noise can vary greatly from place to place. In particular in the geophysical "high frequency" regime ( $> 0.5Hz$ ) seismic noise is mostly generated by local disturbances such as wind, moving water and so-called "cultural noise". The level of seismic noise between a very quiet site and a noisy site can vary by at least two or even three orders of magnitude. The quietest sites are those away from man-made sources and the coastline, and below the earth's surface (e.g. down a mine).

Measurements of the spectrum of seismic noise at frequencies  $> 0.5Hz$  have been carried out by many groups [14], [15], [55], and it seems that the levels of seismic noise in the vertical and horizontal directions are essentially of the same order of magnitude.

Taking into account those papers, above some Hz, the spectrum of seismic vibrations is well approximated by means of the empirical expression:

$$x_t = \frac{a}{f^2} \frac{m}{\sqrt{Hz}} \quad (2.1)$$

where  $f$  is the frequency and  $a$  is a constant varying in the range  $10^{-9} < a < 10^{-7}$  depending on sites.

As we have seen in the first Chapter, the expected gravitational wave signal should produce an arm length variation less than  $10^{-18}$  m. If we consider a ground motion amplitude around  $10^{-6}$  m, the required attenuation factor should be at least  $10^{-12}$ .

### 2.1.2 Newtonian noise

Because of its  $\frac{1}{f^2}$  behavior, the seismic noise affects the low frequency threshold of the Earth-based interferometric gravitational wave detectors. But, as it will be explained in a while, suspending the mirrors it is possible to lower this threshold (towards zero in a very hypothetical circumstances). The real limit is related to the fluctuation of the mass density which arising from seismic motion itself. The mass density variation has obvious consequences on the local gravitational field.

Those unshielded variations of gravitational field directly couple to the mirrors producing an equivalent gravitational noise given by [17]:

$$\tilde{h}_n = \frac{2}{3\sqrt{\pi}} \frac{G\rho}{L} \frac{x_s(f)}{f^2} \quad (2.2)$$

where  $L$  is the interferometer length,  $G$  is the gravitational constant,  $\rho$  is the average soil density and  $x_s(f)$  is the local seismic spectrum.

Because of the impossibility to shield gravitational field *any vibration isolation system is ineffective on this noise source.*

### 2.1.3 Seismic attenuation

The simplest seismic filter we can consider is a simple pendulum. It is well known that the equation of motion of a pendular system can be written as:

$$\ddot{x} + \frac{mg}{L}(x - x_0) = F_{ext} \quad (2.3)$$

where  $L$  is the pendulum length,  $m$  is the mass,  $g$  is the gravitational acceleration,  $x$  and  $x_0$  are the position of the mass and the suspension point respectively and  $F_{ext}$  an external force applied to the mass.

Defining the natural frequency  $f_0$  (and pulsation  $\omega_0 = 2\pi f_0$ ) of the pendulum:

$$f_0 = \frac{1}{2\pi} \sqrt{\frac{g}{L}} \quad (2.4)$$

and solving the (2.3) in the frequency domain we obtain:

$$x(\omega) = \frac{\omega_0^2 x_0(\omega) + \frac{F_{ext}(\omega)}{m}}{\omega_0^2 - \omega^2} \quad (2.5)$$

In absence of external forces  $F_{ext}$  the system transfer function is:

$$\frac{x(f)}{x_0(f)} = \frac{f_0^2}{f_0^2 - f^2} \quad (2.6)$$

It is easy to understand why a simple pendulum acts as a low-pass mechanical filter:

- At low frequencies  $f \ll f_0$  the pendulum is a short circuit for ground vibrations:  $x(f) \approx x_0(f)$ .
- At high frequencies  $f \gg f_0$  the ground motion is attenuated like:

$$\left| \frac{x(f)}{x_0(f)} \right| \approx \frac{f_0^2}{f^2} \quad (2.7)$$

If an external force  $F_{ext}$  is applied to the mass, the effect for  $\omega \gg \omega_0$  is described by the equation:

$$m\omega^2x(\omega) + F_{ext} \approx 0 \quad (2.8)$$

which is an equation describing a *free* mass. This means that, for any practical aspect, a gravitational wave do not make distinction between a free mass and a suspended one in a certain frequency range.

In addition, the low-pass behavior can be "amplified": in order to achieve a suitable attenuation factor, several pendula can be chained . This is the reason why in the VIRGO interferometer (and in the Naples interferometer too) all the optical components are suspended by means of a pendula chain.

The resulting transfer function between the top point of suspension and the lowest mass has the form [18]  $f_1^2 \cdot f_2^2 \dots \cdot f_n^2 / f^{2n}$  for an  $n$ -stage suspension system at frequencies above the highest resonant frequency of the coupled system, where the  $f_n$ 's are the normal modes of the pendula chain elements.

We have said that the isolation achievable increases as  $f^{2n}$ , but its actual value at any particular frequency also depends on the normal mode frequencies, which will be a function of the resonant frequencies of each stage separately and of the ratios of the masses of each stage. For example, for a two-stage system with upper and lower resonant frequencies of each stage separately being  $f_1$  and  $f_2$  and masses  $m_1$  and  $m_2$ , respectively, the transfer function is given by [18]:

$$\frac{\tilde{x}_{out}(f)}{\tilde{x}_{in}(f)} = \left(1 + \frac{m_2}{m_1}\right) \frac{f_1^2 \cdot f_2^2}{f^4} \quad (2.9)$$

at frequencies  $f$ , above the highest normal mode. Thus to achieve the best isolation one would like to have  $m_2 \ll m_1$  which also has the beneficial effect of keeping the highest normal mode low.

The figure (2.1) shows a comparison between the transfer function of a simple pendulum and a pendula chain composed by three pendulum in series.

The actual attenuation system built in our laboratory is obviously a more complex structure. It is composed by 5-stage (see Figure 2.2).

Schematically, we can describe our system in terms of four elements:

- The pre-isolation stage (the inverted pendulum).
- The vertical filters.
- The pendula chain.
- The mirror.

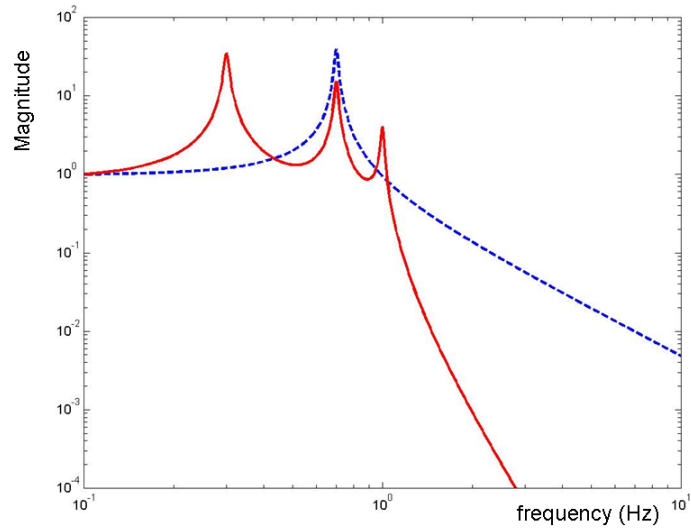


Figure 2.1: Simple pendulum transfer function (dotted line) and pendula chain transfer function (continuous line).

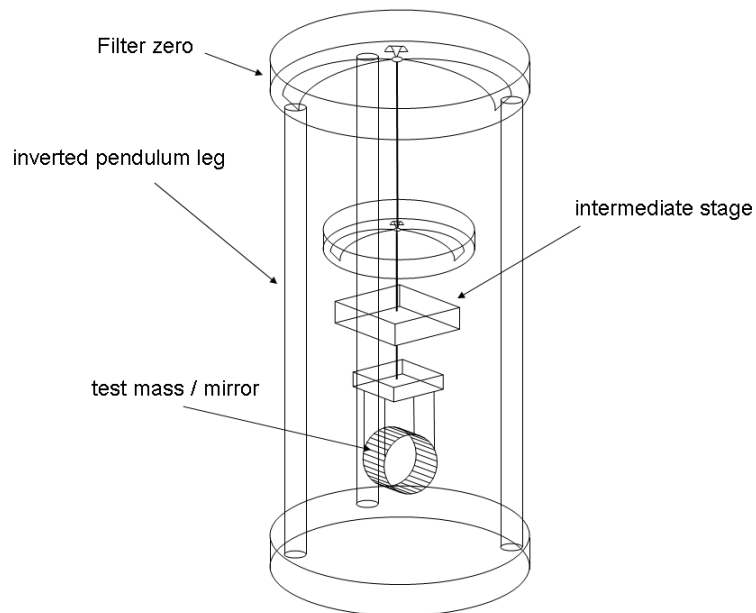


Figure 2.2: Seismic Attenuation System outline.

In the following we will briefly describe the inverted pendulum and the way to control the mirror.

## 2.2 The inverted pendulum

As explained in the previous Chapter, the interferometer optical elements (mirrors and beam splitter) are suspended by means of a pendula chain. Obviously, the pendula chain itself need to be sustained. An additional stage is devoted to this purpose: the *Inverted Pendulum (IP)*.

The IP is in many ways an ideal system for vibration attenuation in the horizontal plane, in spite of its sensitivity to ground tilts. It allows achievement of very low resonant frequencies, and therefore a large seismic noise attenuation factor, with the simple tuning of its payload weight, permits micro positioning with negligible forces, while obtaining the gain of altitude necessary to suspend the attenuation chain.

In order to create a stable support for the vertical static load, our IP is constructed with three rigid cylindrical legs supporting a rigid table. The use of the tri-legged IP table has the fundamental advantage of providing a platform, which has movements confined in the horizontal plane, while being extremely soft inside that plane (translations and rotation). The property of having only horizontal movements is very important when active controls are applied to provide inertial damping for the attenuation chain resonant modes. Any off-plane actuation force would be neutralized by the systems rigidity.

It is of importance to separate the horizontal degrees of freedom from the vertical ones. In order to avoid translation/tilt couplings, it is very important to construct the IP legs perfectly straight and of identical length. Both requirements can be achieved with machining and assembly precision of less than  $0.1mm$ . All three legs of the IP are attached to a platform via identical, precision-machined maraging steel [20] cylindrical flexures, serving as pivot points for the IP and providing the harmonic restoring force to keep the IP table straight up.

On the top, the three legs are connected to a rigid table by means of small flexures. Such a rigid table is called *Filter Zero (FO)*. It is a vertical filter which uses blades to suspend the pendula chain.

Summarizing, the IP has a triple function:

- Pre-filtering low frequency seismic noise, providing attenuation at frequencies of microseismic peak.

- Providing a quasi-inertial stage to actively damp the motion of the suspended chain, avoiding actuation noise re-injection (taking advantage of the passive attenuation between the IP itself and the test mass).
- Providing a mean to allow precision positioning of the mirror and the pendula chain using small forces.

## 2.3 Mechanical description of the inverted pendulum

An inverted pendulum can be described, in a simplified model, as a rigid cylindrical leg having length  $l$  and mass  $m$ , supported by a perfectly elastic element having spring constant  $k_\theta$  fixed to the ground. On the top of the leg, a payload of mass  $M$  (which is modelled as a point mass) is the object being isolated from the ground motion. A schematic model of the IP is shown in figure (2.3). The IP leg is represented as a completely rigid body and its internal resonances are omitted in the following model.

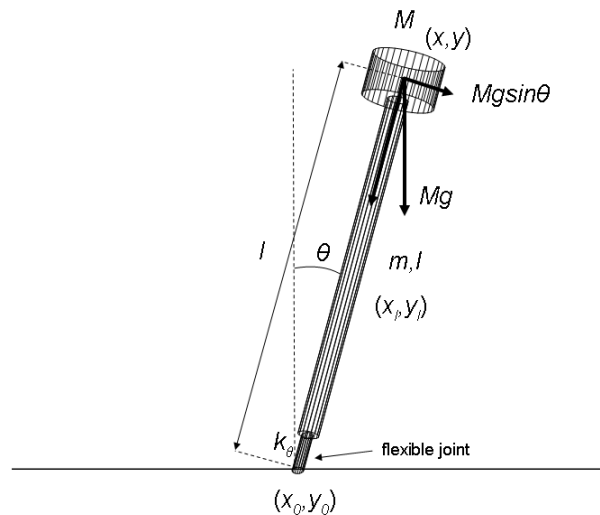


Figure 2.3: Inverted pendulum.

The lagrangian of the system as a function of the parameters shown in table 5.1 is expressed as:

$l$	length of the IP leg
$m$	mass of the IP leg
$I$	momentum of inertia about the center of mass of the IP leg
$M$	mass of the payload
$k_\theta$	rotational spring constant of the flex joint
$(x, y)$	position of the payload
$(x_l, y_l)$	position of center of the mass of the IP leg
$(x_0, y_0)$	position of the flex joint attached to the ground
$\theta$	angle of the IP leg with respect to the vertical axis

Table 2.1: Parameters for the simple inverted pendulum model.

$$L = K - U \quad (2.10)$$

where the contribute of the kinetic energy  $K$  is:

$$K = \frac{1}{2}M(\dot{x}^2 + \dot{z}^2) + \frac{1}{2}m(\dot{x}_l^2 + \dot{z}_l^2) + \frac{1}{2}I\dot{\theta}^2 \quad (2.11)$$

and the potential energy is:

$$U = Mgz + mgz_l + \frac{1}{2}k_\theta\theta^2 \quad (2.12)$$

with the geometrical constraints:

$$\begin{aligned} x_l &= \frac{1}{2}(x + x_0) \\ z_l &= \frac{z}{2} \\ x &= l \sin \theta + x_0 \\ z &= l \cos \theta \end{aligned} \quad (2.13)$$

Using these conditions, the kinetic and potential terms in the Lagrangian are simplified, by omitting the vertical component of the velocity we have:

$$K = \frac{1}{2}M\dot{x}^2 + \frac{1}{8}m(\dot{x} + \dot{x}_0)^2 + \frac{1}{2}I\left(\frac{\dot{x} - \dot{x}_0}{l}\right)^2 \quad (2.14)$$

and

$$U = Mgl \cos\left(\frac{x - x_0}{l}\right) + \frac{mgl}{2} \cos\left(\frac{x - x_0}{l}\right) + \frac{1}{2}k_\theta\left(\frac{x - x_0}{l}\right)^2 \quad (2.15)$$

As well known, the equation of motion of our system are given by the *Euler-Lagrange equations*:

$$\frac{d}{dt} \frac{\partial K}{\partial \dot{x}} = \frac{\partial U}{\partial x} \quad (2.16)$$

applying the (2.16) on (2.14) and (2.15) we obtain:

$$\left(M + \frac{m}{4} + \frac{I}{l^2}\right)\ddot{x} + \left(\frac{m}{4} - \frac{I}{l^2}\right)\ddot{x}_0 = -\left[\frac{k_\theta}{l} - \left(\frac{m}{2} + M\right)g\right]\frac{x - x_0}{l} \quad (2.17)$$

At the first order the equation (2.17) has the form of the equation of motion of a harmonic oscillator, with an effective spring constant:

$$k_{eff} = \frac{k_\theta}{l^2} - \left(\frac{m}{2} + M\right)\frac{g}{l} \quad (2.18)$$

where the first term in  $k_{eff}$  corresponds to the elastic restoring force of the flex joint, the other terms represent a repulsive force, the so called *gravitational anti-spring force*. With the gravitational anti-spring effect the cumulative spring constant is effectively reduced.

It is important to note that the effect of the anti-spring is proportional to the mass of the leg and the payload and can be tuned by changing the payload. The resonance frequency of the IP can be determined using the equation (2.17) as:

$$f_0 = \frac{1}{2\pi} \sqrt{\frac{k_{eff}}{M + \frac{m}{4} + \frac{I}{l^2}}} \quad (2.19)$$

By solving equation (2.17) in the Fourier domain we obtain the motion transfer function between the ground and the payload:

$$H_{IP}(\omega) = \frac{k_{eff} + \left(\frac{m}{4} - \frac{I}{l^2}\right)\omega^2}{k_{eff} - \left(M + \frac{m}{4} + \frac{I}{l^2}\right)\omega^2} \quad (2.20)$$

The Bode plot of the transfer function of the simple IP is shown in figure (2.4).

The transfer function of the IP behaves similarly to that of the harmonic oscillator up to somewhere above the resonant frequency. While the ideal, massless oscillator shows infinite capability of attenuation, the IP transfer function saturates at a certain level of attenuation originating a plateau.

From the equation (2.20) it is possible to find the plateau level of the transfer function:

$$\lim_{\omega \rightarrow +\infty} H_{IP}(\omega) = \frac{\frac{m}{4} - \frac{I}{l^2}}{M + \frac{m}{4} + \frac{I}{l^2}} \quad (2.21)$$

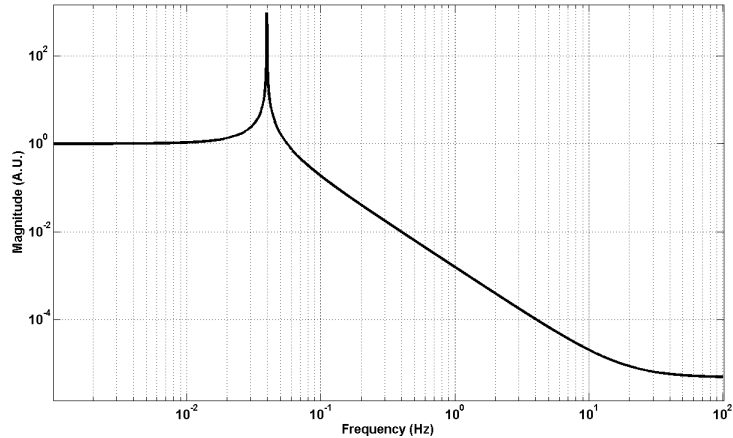


Figure 2.4: Inverted pendulum transfer function.

This behavior is physically related to the *center of percussion effect* (COP). When an external force is applied onto a free rigid body, it accelerates both translationally and rotationally around its center of mass. However a rigid body like the IP leg, is not allowed to rotate freely as it is connected to the payload at one end and to the ground by the flex joint at the other end. The flex joint though is a negligible constraint at frequencies higher than the resonant frequency, and the leg will rotate around a well defined point. In this case the ratio of the translational motion of the payload and the ground is determined only by the geometry of the flex joint and the center of rotation.

## 2.4 Inverted pendulum with counterweight

To mitigate the center of percussion effect (i.e. reducing the level of the plateau), the mass distribution of the leg must be arranged that the center of rotation coincides with the payload suspension point.

This can be achieved providing the leg with a counterweight (CW) below the elastic joint to move the percussion point at the height of the hinging point of the flexible joint. A schematic representation is shown in figure (2.5).

The transfer function of a model of the IP with this CW is plotted in figure (2.6). The model is parameterized using the following variables:

In the model with the counterweight, the equation of motion and the IP transfer function can be written as [21]:

$$-C\omega^2x - B\omega^2x_0 = -A(x - x_0) \quad (2.22)$$

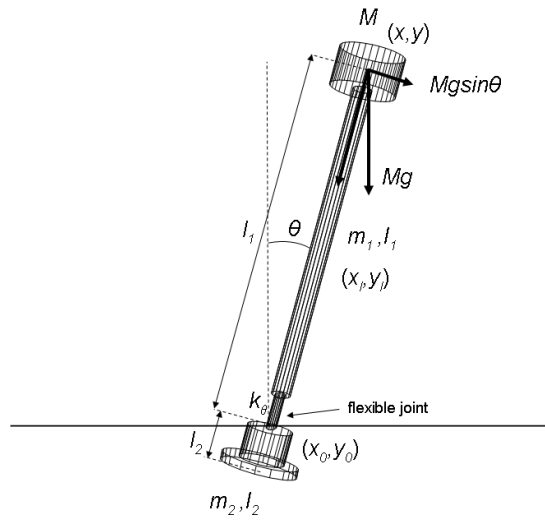


Figure 2.5: A schematic view of the IP with the CW mounted at the bottom of the leg. The counter-weight is mounted at the bottom of a bell, coaxially with the leg.

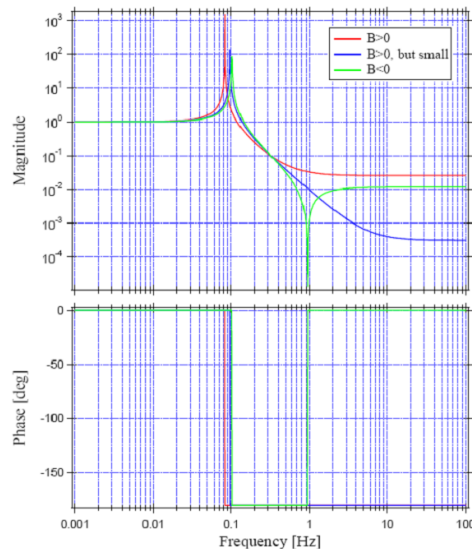


Figure 2.6: Transfer function of the IP with excessive (blue and green [black and grey in *black and white printed version*]) and without (red [light grey]) CW. The attenuation performance at high frequencies is substantially improved with a CW close to the ideal one (blue [black]).

$l_1$	length of the IP leg
$m_1$	mass of the IP leg
$I_1$	momentum of inertia about the center of mass of the IP leg
$M$	mass of the payload
$l_2$	length of bell
$m_2$	mass of bell
$I_2$	momentum of inertia about the center of mass of the bell
$M_3$	mass of the CW
$k_\theta$	rotational spring constant of the flex joint
$(x, y)$	position of the payload
$(x_0, y_0)$	position of the flex joint attached to the ground
$\theta$	angle of the IP leg with respect to the vertical axis

Table 2.2: Parameters for an inverted pendulum model with counterweight.

and then:

$$H_{IPCW}(\omega) = \frac{A + B\omega^2}{A + C\omega^2} \quad (2.23)$$

where  $A$ ,  $B$  and  $C$  are:

$$A = \frac{k_\theta}{l_1^2} - \frac{g}{l_1} \left( M + \frac{m_1}{2} - \frac{m_2 l_2}{2l_1} - \frac{M_3 l_2}{l_1} \right) \quad (2.24)$$

$$B = -\frac{I_1 + I_2}{l_1^2} + \frac{m_1}{4} - \frac{m_2 l_2 (2l_1 + l_2)}{4l_1^2} - \frac{M_3 l_2 (l_1 + l_2)}{l_1^2} \quad (2.25)$$

$$C = M + \frac{m_1}{4} + \frac{m_2 l_2^2}{4l_1^2} + \frac{M_3 l_2^2}{l_1^2} + \frac{I_1 + I_2}{l_1^2} \quad (2.26)$$

The plateau level in the transfer function is determined by the terms  $B$  and  $C$ . The parameters related to the CW can be used to tune the maximum attenuation at high frequencies and higher attenuation levels. Particularly the IP realizes ideal attenuation when  $B$  is made null with the optimal CW. Too much CW over-compensates the mass of the leg and brings the center of percussion point below the flex joint, then the IP leg rotates in differential mode with respect to the translational motion. The tip of the leg moves in the opposite direction of the perturbation motion and a notch appears in the transfer function. At this point the phase of the transfer function changes sign (180° rotation). The counterweight makes the IP leg virtually massless and, in principle, it permits to completely eliminate the attenuation saturation due to the COP effect.

## 2.5 Vertical attenuation system

Theoretically, just the seismic oscillations along the interferometer optical axis should have some practical effect. But in the real system, all degrees of freedom motion have to be attenuated because of the unavoidable coupling between translational and rotational components. This means, for instance, that a vertical displacement (which should be ineffective on the interferometer alignment, at least for plane mirrors) has effect along the beam direction.

In addition, the inverted pendulum is not intended to filter out vertical vibration because the flexible joints of the IP are rigid along the vertical direction.

Cross-coupling between vertical and horizontal (longitudinal) modes potentially limits the performance of mechanical isolation systems. Thence the vertical isolation must be designed at least not to be the limiting factor of the overall performance. Geometric Anti-Spring (GAS) is the solution developed for our seismic attenuation system. Such a solution realizes low frequency resonance, typically about a few hundreds of  $mHz$ , based on linear anti-spring effect. The GAS is a set of radially arranged cantilever springs, mounted from a common retainer ring structure and opposing each other via a central disk. The payload to be isolated is connected to the central part. The blades are completely flat when manufactured and flex like a fishing rod under load. They are mounted on clamping devices with an appropriated initial angle to accommodate the bending. The clamping devices are positioned to introduce a suitable radial and horizontal compression of the blades.

The radial stress tends to release itself by pushing the system up or down, thus generating a negative spring constant. In other words, the constrained geometry produces a nonlinear force vs. displacement behavior with a flat region around the point of operation. The geometric antispring (GAS) effect can then be tuned and, in principle, an arbitrarily low vertical resonant frequency can be achieved.

To describe the macroscopic behavior of the GAS a numerical computation with a sophisticated non-linear finite element model is needed.

However, a simple analytical model is quite useful to understand its working principle. At the same time this simple model is able to analyze the behavior of GAS around its equilibrium (working) position with good precision.

The figure (2.8) shows the idea beyond the *linear* model for GAS.

A long cantilever spring can be represented as a simple vertical spring with a horizontal component. At the same time, a set of two spring tied at their tips can be represented as a linear combination of vertical and horizontal linear springs. Because of the symmetry of the system, the model can be truncated to a single blade with the constraint that the tip of the blade can

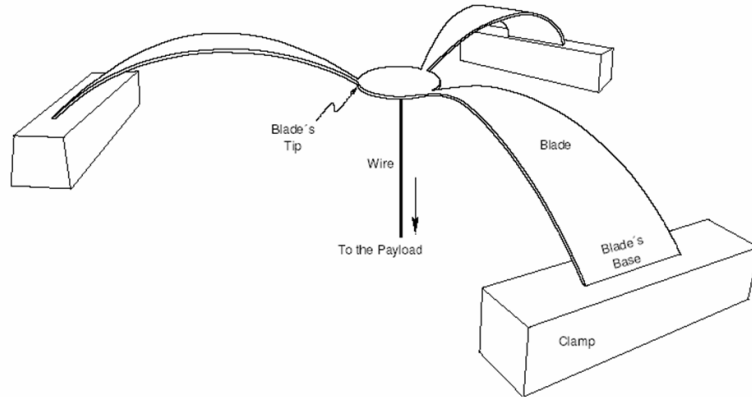


Figure 2.7: Transfer function of the IP with excessive (blue and green) [Schematic representation of the blades which compose the Geometric Anti-Spring system.

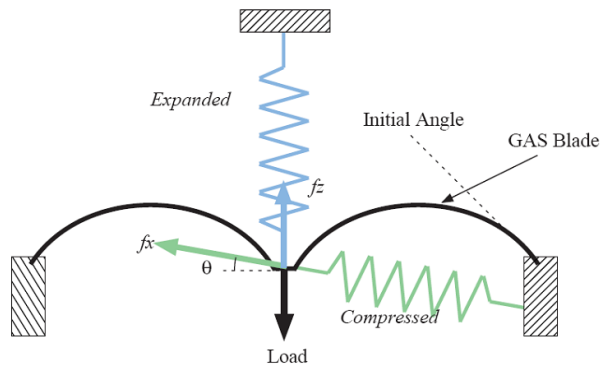


Figure 2.8: Linear model for GAS.

move only along the vertical axis. This constraint describes the compensation of the horizontal component of the spring force in a real system. The cantilever spring system is best viewed as composed of two separate spring, one in the horizontal and one in the vertical direction.

Our model for the GAS filter can be represented as: a payload of mass  $m_0$  suspended by means of a vertical spring of elastic constant  $k_z$  and rest length  $l_{0z}$  and by two horizontal springs opposing each other of constant  $k_x$  and rest length  $l_{0x}$ .

The working (equilibrium) position of the tip is represented by  $z_{eq}$ , and  $z$  is defined as the difference between the actual tip height and the working position, while the horizontal position is fixed. The length of the horizontal spring is  $\sqrt{x_0^2 + z^2}$  and the angle made by the horizontal springs is  $\theta$ . The equation of motion for the system along the vertical axis is then:

$$m\ddot{z} = k_z(z_{eq} - z - l_{0z}) - k_x(l - l_{0z}) \cos \theta - mg \quad (2.27)$$

Removing the constant forces which correspond to the equilibrium, the equation will be:

$$m\ddot{z} = -k_z z - k_x \left( l - l_{0x} \right) \frac{z}{l} \quad (2.28)$$

Expanding the equation of motion (2.28) around the working point ( $z = 0$ ) to the first order on  $z$ , we obtain:

$$m\ddot{z} = - \left[ k_z + k_x \left( 1 - \frac{l_{0x}}{x_0} \right) \right] z \quad (2.29)$$

We can see that at the first order the system behaves like a linear harmonic oscillator with effective spring constant:

$$k_{eff} = k_z + k_x \left( 1 - \frac{l_{0x}}{x_0} \right) \quad (2.30)$$

The last term of (2.30) is referred as the Geometric Anti-Spring contribute because it introduces a negative spring constant into the system when the horizontal spring is under compression ( $x_0 < l_{0x}$ ). As consequence of it the effective stiffness is reduced, and so the resonant frequency, by just compressing the horizontal springs. The systems response is equivalent to a second order low pass filter with a very low resonance frequency (using appropriate materials as maraging steel). Compared with an equivalent spring with same frequency, it is much more compact and with motion limited to only one direction.

## 2.6 Control strategies

As previously mentioned, on the top of the IP there is the *Filter Zero* in which is placed the suspension point of the pendula chain.

The *Filter Zero* is actively controlled. The reason to control actively the system is the following: the attenuation system elements described until now and the results they are able to perform are not sufficient to the interferometer locking requirements. Each element furnish a passive filtering out. In particular:

*$f < IP\ resonance\ frequency$ .* The seismic noise is completely transmitted to the mirror (because no filter is present). In the VIRGO case the displacement produced by tidal effects can be even  $60\ \mu m$ .

*$IP\ resonance\ frequency < f < some\ Hz$ .* Normal modes of the attenuation system itself (IP and pendula chain elements) are responsible of mirror oscillation that in the VIRGO case can exceed  $10\ \mu m$ }

In both of cases amplitude oscillation exceeds design limit for several orders of magnitude (8 in the VIRGO case). The solution is offered by an *active* control. This control should not act directly on the mirror because the attenuation amplitude to perform is too expensive (in terms of dynamical range). This is the reason why the control is realized in a hierarchical [23] way acting in different point of the system and each control acting at its competence bandwidth. In our system those points are:

*The inverted pendulum.* Thanks to its peculiar structure it is possible obtaining displacement of  $\pm 1\ cm$  in the frequency range  $f < 0.1\ Hz$  without injecting electronic noise.

*The intermediate stage.* On this element is possible to apply forces which produce displacement of  $\pm 10\ \mu m$  in the bandwidth  $0.1-1\ Hz$ .

*The mirror.* For  $f > 1\ Hz$  forces can be applied directly on the reference mass which holds the mirror.

## 2.7 Sensors and actuators system

As we have seen in the previous section, the passive isolation provided by the seismic attenuation system is not sufficient for our purposes. To provide a position control, an inertial damping of the pendula chain and the final control of the mirror for the locking requirements, the seismic attenuation

system is provided with a set of sensors and actuators placed in different points of the structure.

In particular, in this section we will describe the set of sensors and actuators devoted to the control of the inverted pendulum.

The inverted pendulum is a three degree of freedom system. For this reason we need (at least) three sensor to detect its position (or acceleration) and three actuator to act on it.

Those sets of sensors and actuators are placed on the *Filter Zero* which is the table connected to the top of the IP (as previously mentioned) and containing in its structure the GAS system. A schematic view of the position of sensors and actuators is in figure (2.9).

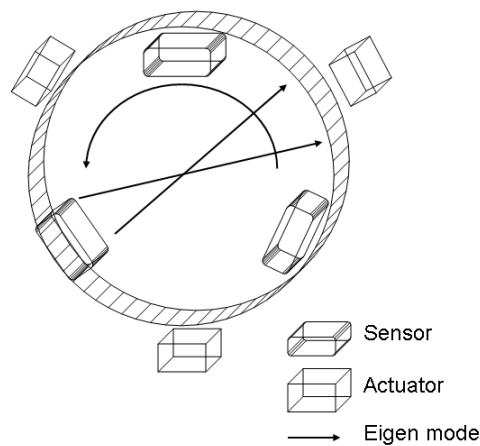


Figure 2.9: Simplified scheme of sensors and actuators system placed on the Filter Zero. Top view.

### 2.7.1 LVDT

To detect the position of the Filter Zero (which is mechanically connected to the inverted pendulum) **LVDT** [24] *linear variable differential transformer* are used.

This set of high-precision position sensors is mounted in a triangular configuration (2.9).

Commercial LVDT are quite usual as position sensors, they employing the principle of induction shown in figure (2.10).

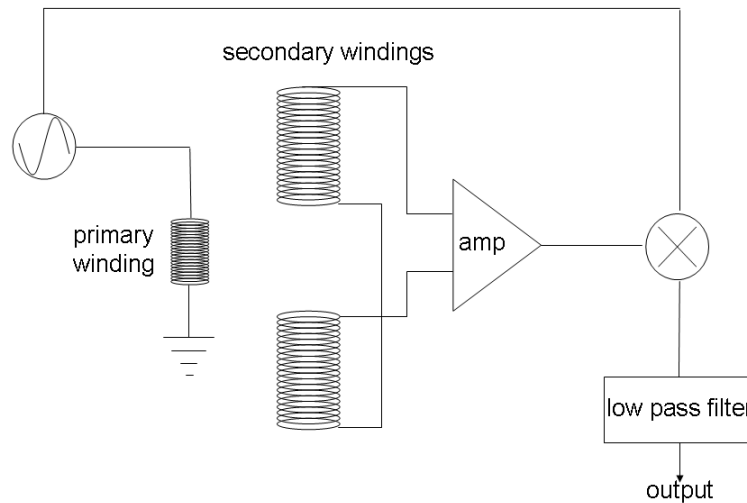


Figure 2.10: Scheme of an LVDT (linear variable differential transformer).

An LVDT is composed by a primary and two secondary windings. The moving central coil (*the exciter*) is driven by a 20 kHz signal; the two secondary coils, symmetric with respect to the primary, are in series and oppositely wound. A displacement of the exciter induces current changes in the windings proportional to the displacement amplitude (2.11). The signal from the receiver is amplified, then demodulated in phase and lowpass filtered.

LVDTs are used to measure the relative motion of the IP with respect to the ground. For this purpose the exciter is mounted on the *Filter Zero* and the secondary coils are connected to an external frame (mechanically connected to the ground).

Such a position transducers have been expressly designed to this purpose. The specifications of these position sensors are the following:

- Linearity within 1% over  $\pm 10mm$  to match the typical dynamic range of the inverted pendulum.
- Insensitivity to movements in the directions. orthogonal to the sensing axis, to allow for free movements of the IP on the horizontal plane and

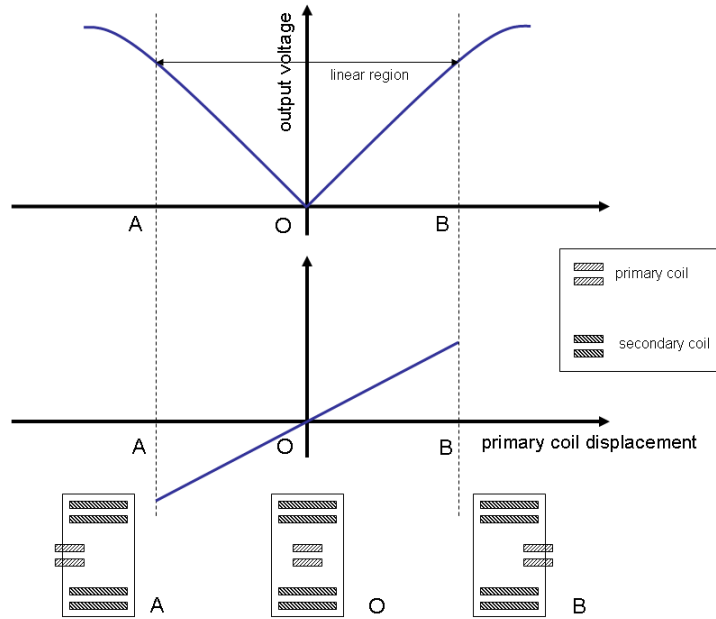


Figure 2.11: Typical output voltage of LVDT.

not to re-inject seismic signals from the orthogonal directions in the feed back loop.

- Force-free and contact-free, to avoid short circuiting of the seismic excitation to the IP table.
- Fully Ultra-High-Vacuum (UHV) compatible, to prevent the contamination of the vacuum conditions.
- Position resolution  $\sim 10nm$  r.m.s. to allow the reduction of mirror residual motion.

Unlike conventional magnetic core LVDTs, this sensor has no ferromagnetic components and does not generate unwanted forces when exposed to external magnetic fields.

The coils are made of Kapton-coated copper wire, wound around Peek supports, and are, therefore, completely UHV compatible. A picture of the LVDT used is shown in figure (2.12)

A vertical LVDT, based on same principle and made of same materials is placed near the GAS system and used to detect the vertical position of the suspension point of pendula chain with respect the Filter Zero.

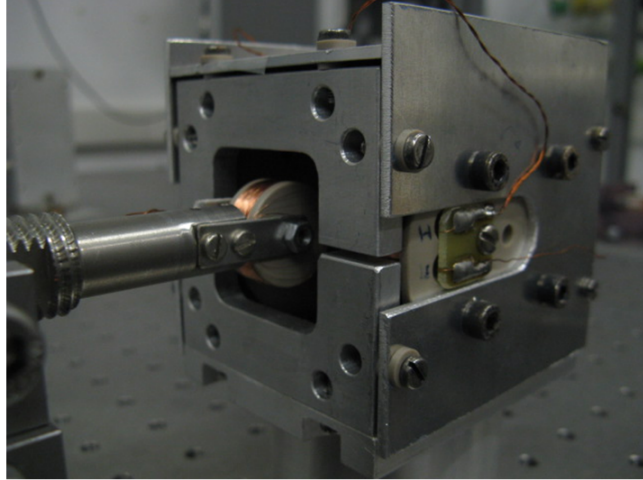


Figure 2.12: LVDT used to detect the inverted pendulum position.

### 2.7.2 Magnet coil actuators

The horizontal actuation system is realized by a triplet of magnet-coil actuators [29]. Those actuators, also named voice-coil actuators (because the inventor got the idea from a speaker) are quite common as commercial device. Our actuators are special purpose device: UHV-compatible, low-noise and non-contacting.

As happens for position sensors, the windings are connected to the Filter Zero and magnets are placed on the external frame. Actuators are mounted in a triangular configuration as the LVDT but, for practical reason, not in the same position.

The instrumentation is shown in figure (2.13). It consists of a coil which has a track-shaped cross section and a yoke that leads magnetic field of the permanent magnets. As the coil is flattened at the center, its magnetic field can be considered, approximately, the same as the one produced by two parallel planes with current in opposite direction (constant field at given distance from the surface).

The actuators used in the control of the IP have very wide linear range over  $20\text{mm}$  which is more than necessary comparing with the range of the IP. The calibration of the actuator is about  $0.01\text{N/A}$ .

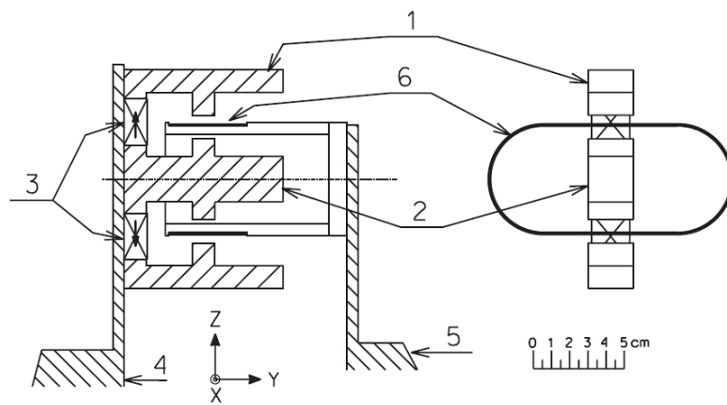


Figure 2.13: Schematic view of the non-contacting actuator. Side view (left side) and front view (right side): (1) yoke jaws; (2) yoke central bar; (3) permanent magnets (the arrows in the magnet indicate the field direction); (4) mechanical support on the fixed structure; (5) mechanical support on the IP; and (6) racetrack coil. For simplicity the mechanical supports are only sketched on the side view [29].

### 2.7.3 Accelerometers

The position of the inverted pendulum at which is connected the pendula chain and then the mirror is provided by means of LVDT sensors. But this position is referred to an external frame, which is connected to the ground. Any control loop based on this position as reference will reintroduce seismic noise on the pendula chain vanishing all beneficial effects of the seismic attenuation system.

Horizontal accelerometers are used to perform inertial damping in the seismic attenuation system. The mechanics of the device consists of a monolithic folded pendulum (FP) [26] as shown in figure (2.14) but it will be better described in dedicated chapter on this topic. In a FP a proof mass is suspended on one end by a simple pendulum and supported on the other by an inverted pendulum.

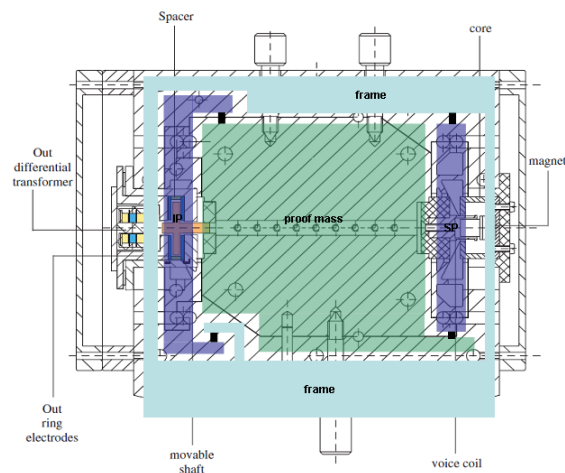


Figure 2.14: Schematic view of the accelerometer. It is composed by an inverted pendulum, a simple pendulum and a proof mass mechanically connected by means of small flexures. On the left side is placed a capacitive sensor and on the right side a voice-coil actuator.

The working principle is the following: the motion of the proof mass is monitored by a capacitive sensor and a feedback force provided by the actuator keeps the mass in the equilibrium position as shown in figure (2.15).

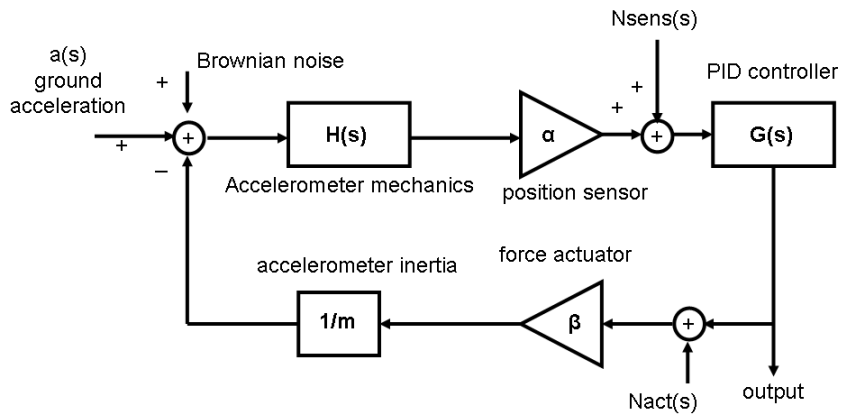


Figure 2.15: Accelerometer principle of working.

The feedback signal is proportional to the acceleration in the frequency range  $0.01 \div 20Hz$ . The FP geometry, combined with the monolithic design, allows the accelerometer to be extremely directional. The vertical-horizontal coupling ranges from  $10^{-6}$  to  $10^{-5}$ .

To make it suitable for ultra-high-vacuum operation and to reduce the probability of failures of the in-vacuum components, the accelerometer is equipped with a high-resolution capacitance sensor fully driven by remote signal conditioning electronics.

# Chapter 3

## Diagonalization procedure

The model design of a MIMO system is often a difficult task. For instance a typical problem is related with a possible disagreement between measured response and the model estimation.

Decoupling multiple input and output channels into several independent single input and output channels can be considered a classical procedure in control system design.

In the following we will consider a procedure to transform a multivariable mechanical system into a set of single input single output system. As we will describe in a while, this method was born in the framework of the control system design in suspended gravitational wave interferometers [10], [11], [12], [13]. But obviously the procedure can be applied on different physical systems.

### 3.1 Introduction

Let suppose our system as linear (because we will take large use of the transfer function concept). This means that when we will apply the numerical procedure to actual physical systems we will restrict our consideration where their dynamical range has a linear behavior only.

If our mechanical system have  $n$  degrees of freedom this means that we need  $n$  sensors at least to detect, for instance, the system position. To act independently on all degrees of freedom direction we need  $n$  actuators at least.

For this reason, let suppose to have a number of sensors and actuators equal to the degrees of freedom number of our physical system.

The input vector  $\mathbf{C} = (C_1, C_2, \dots, C_n)$  is represented by the actuators signal whereas the output vector  $\mathbf{L} = (L_1, L_2, \dots, L_n)$  is the signal provided

by the sensors.

If the  $n$  normal modes of the system are not orthogonal to the sensibility axis of the sensor, each sensor should be sensitive to the projections of all normal modes on its axis. In the same way, each actuator will generate movements that are a mix of system modes.

Here and in the following, the word *diagonalization* means the procedure to obtain a new sensor/actuator space in which each normal mode is independently sensed. In this *virtual* space it will be possible also act on a specific normal mode. From the mathematical point of view, this means to realize a coordinate transformation in which the equation of motion have this kind of expression:

$$\ddot{x}_i + \omega_i^2 x_i = q_i \quad (3.1)$$

where the  $x_i$  (for  $i = 1, 2, \dots, n$ ) is a normal coordinate,  $\omega_i/2\pi$  is the frequency of the  $i$ -th mode and  $q_i$  is the generalized force corresponding to the coordinate  $x_i$  [19]. To diagonalize the system means to find a suitable linear combination of the sensor outputs (*virtual sensors*) each sensitive to a single normal mode. At the same way as *virtual actuators* we intend a linear combination of the actuator signals which is able to excite a single normal mode of the system. Before the diagonalization we can consider our system a MIMO system. The diagonalization procedure allows to consider our system as composed of many SISO systems. The reason to prefer a SISO system is that a single degree of freedom system is much easier to control. In addition controlling each mode by an independent feedback loop can have effects on the stability requirements also. As it will be shown, using this method it is not necessary to find a perfect model to describe the system response. This point makes such a procedure very flexible and suitable to be applied in different physical systems. Especially complex systems in which could be difficult to find a correct model to describe them.

The framework in which the diagonalization idea is born was the control system development in suspended gravitational wave interferometers. In particular this procedure was used on the position control of the *Filter Zero*. Before to use the procedure on a complex system, we tested the method on a simpler system. In the following we will describe the sensors and actuators system on which the procedure has been applied.

## 3.2 The diagonalization method

The diagonalization procedure has been conceived to help the control system design of the the position of the *Filter Zero* described previously.

But this approach can be used on different system. To this purpose we will describe the diagonalization method in a general way. It will be easy to express the terms of the procedure on a different physical system.

Let consider  $n$  generic actuators that are able to excite the system. Their signals are represented by means of the vector  $\mathbf{C} = (C_1, C_2, \dots, C_n)$ . Moreover let consider  $n$  detectors signals  $\mathbf{L} = (L_1, L_2, \dots, L_n)$  that are able to measure the response of the system.

What we want is to make the system *diagonal* i.e. write down the right linear combination of signal sensors to obtain *virtual* disentangled detectors  $(L_1^{virt}, L_2^{virt}, \dots, L_n^{virt})$ . Furthermore, we would like to write down the right linear combination of *real* actuator signals to obtain *virtual* actuators  $(C_1^{virt}, C_2^{virt}, \dots, C_n^{virt})$  capable to act on a single degree of freedom at a time.

In other words the condition we wish to obtain is:

$$\begin{pmatrix} L_1^{virt} \\ L_2^{virt} \\ \vdots \\ L_n^{virt} \end{pmatrix} = \begin{pmatrix} \mathcal{H}_{11}(s) & 0 & \dots & 0 \\ 0 & \mathcal{H}_{22}(s) & \dots & 0 \\ \vdots & \vdots & \ddots & \vdots \\ 0 & 0 & \dots & \mathcal{H}_{nn}(s) \end{pmatrix} \cdot \begin{pmatrix} C_1^{virt} \\ C_2^{virt} \\ \vdots \\ C_n^{virt} \end{pmatrix}$$

As depicted in figure (3.1):

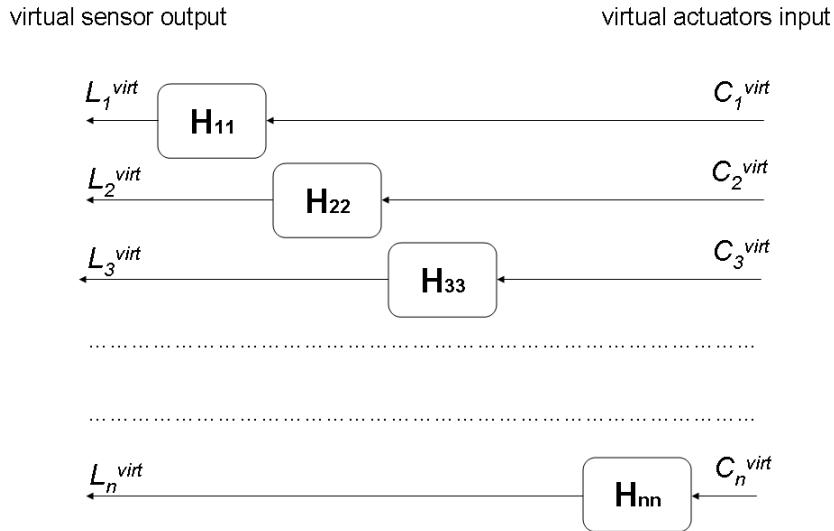


Figure 3.1: Diagonalization goal

But the starting situation is:

$$\begin{pmatrix} L_1 \\ L_2 \\ \vdots \\ L_n \end{pmatrix} = \begin{pmatrix} R_{11}(s) & R_{12}(s) & \dots & R_{1n}(s) \\ R_{21}(s) & R_{22}(s) & \dots & R_{2n}(s) \\ \vdots & \vdots & \ddots & \vdots \\ R_{n1}(s) & R_{n2}(s) & \dots & R_{nn}(s) \end{pmatrix} \cdot \begin{pmatrix} C_1 \\ C_2 \\ \vdots \\ C_n \end{pmatrix}$$

Where the matrix  $R_{ij}(s)$  is composed by the experimental transfer functions obtained exciting the system by means of the  $i - th$  real detector and detecting signals using the  $j - th$  real actuator.

We define the sensing matrix  $\mathcal{S}_{ki}$  as the matrix which describes the coupling of the  $k - th$  virtual detector with the  $i - th$  real detector:

$$\begin{pmatrix} L_1^{virt} \\ L_2^{virt} \\ \vdots \\ L_n^{virt} \end{pmatrix} = \mathcal{S} \cdot \begin{pmatrix} L_1 \\ L_2 \\ \vdots \\ L_n \end{pmatrix}$$

The driving matrix  $\mathcal{D}_{jk}$  describes the coupling of the  $j - th$  real actuator with the  $k - th$  virtual actuator and it is defined as:

$$\begin{pmatrix} C_1 \\ C_2 \\ \vdots \\ C_n \end{pmatrix} = \mathcal{D} \cdot \begin{pmatrix} C_1^{virt} \\ C_2^{virt} \\ \vdots \\ C_n^{virt} \end{pmatrix}$$

So the overall transfer function of virtual detectors over virtual actuators can be written as follow:

$$\begin{pmatrix} L_1^{virt} \\ L_2^{virt} \\ \vdots \\ L_n^{virt} \end{pmatrix} = \mathcal{S} \cdot R_{ij}(s) \cdot \mathcal{D} \cdot \begin{pmatrix} C_1^{virt} \\ C_2^{virt} \\ \vdots \\ C_n^{virt} \end{pmatrix}$$

Or:

$$\begin{pmatrix} L_1^{virt} \\ L_2^{virt} \\ \vdots \\ L_n^{virt} \end{pmatrix} = \mathcal{H} \cdot \begin{pmatrix} C_1^{virt} \\ C_2^{virt} \\ \vdots \\ C_n^{virt} \end{pmatrix}$$

Where we can identify:

$$\mathcal{H} = \mathcal{S} \cdot R(s) \cdot \mathcal{D} \quad (3.2)$$

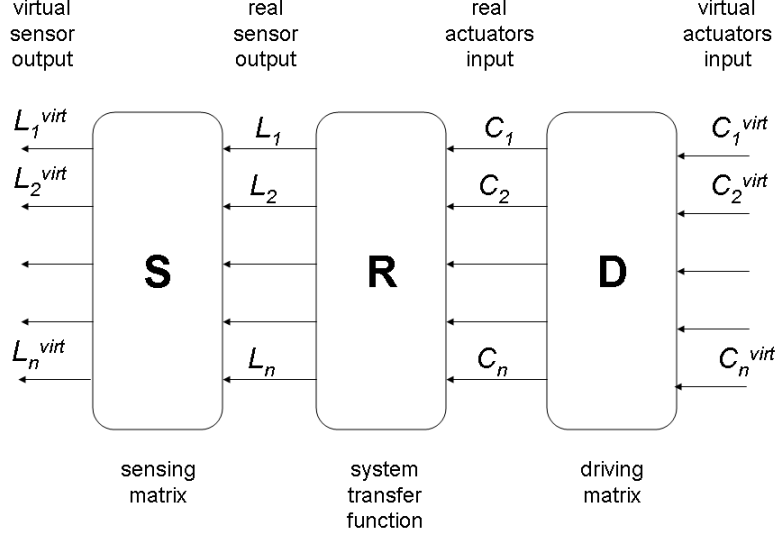


Figure 3.2: Matrix definition:  $\mathcal{S}$  is the sensing matrix,  $R$  is the system transfer function and  $\mathcal{D}$  is the driving matrix

The goal is to estimate the sensing matrix  $\mathcal{S}$  and the driving matrix  $\mathcal{D}$  from experimental data  $R_{ij}(s)$ . The transfer function matrix  $R_{ij}(s)$  is experimentally evaluated exciting with white noise the system by means of the actuator  $C_j$  and detecting the response  $L_i$  of the  $i$ -th sensor ( $i = 1, 2, \dots, n$ ). For each excitation we can detect a row of  $R_{ij}(s)$ . This means that to fully determinate  $R_{ij}(s)$  we need to excite  $n$  times our system building the response matrix row by row.

Several approaches are been used for this purpose [30], [31], [32]. Our method is very simple in principle: we estimate  $\mathcal{S}$  and  $\mathcal{D}$  building the matrix function  $\mathcal{H} = \mathcal{S} \cdot R(s) \cdot \mathcal{D}$  which have to be in a diagonal form.

Using a mathematical algorithm, we look for  $\mathcal{S}$  and  $\mathcal{D}$  which are able to minimize all off diagonal elements.

From the practical point of view, we minimize the sum of the squared off-diagonal elements. Furthermore we request the transformation matrices to have some additional condition to avoid to find trivial solution only.

We request the normalization of each row of  $\mathcal{S}$  (such a condition will preserve also measurement units in the virtual sensors) and the the normal-

ization of each row of the inverse of  $\mathcal{D}$  (which is the matrix we want to preserve measurement units).

In order to implement those requirements we have to minimize the quantity:

$$\sum_{lk} |\mathcal{H}_{lk}|^2 + w[(\mathcal{S} \cdot \mathcal{S}^T - 1)^2 + (\mathcal{D}^{-1} \cdot (\mathcal{D}^{-1})^T - 1)^2]. \quad (3.3)$$

Where  $l \neq k$  and  $w$  is an arbitrary weight chosen to be the number of measured data.

This algorithm has been implemented in a *MATLAB*<sup>®</sup> code using as solver function *lsqnonlin* which is a library function used in nonlinear least-squares (nonlinear data-fitting) problems.

### 3.3 Sensors and actuators on simple pendulum

The preliminary testing bench was a system very similar to the last stage of the pendula chain: a mirror suspended by means of a simple pendulum.

This experimental setup is used to test electrostatic actuation instead of the magnet coil actuation presently used in the VIRGO interferometer. Electrostatic actuators (**EA**) [27] are the most promising devices for mirror control for next generation interferometric gravitational wave detectors.

In the system depicted in figure (3.3) the mirror position is detected using an optical lever: a superluminescent diode beam is sent through a single-mode optical fibre to the mirror. The reflected beam is detected by means of a position sensing photodiode.

In this case we have a two degrees of freedom system: the mass/mirror has a translational mode and a rotational mode (with respect to the vertical). Electrostatic actuators are used to excite the mass. The reflected optical beam is split by means of a beam splitter and a lens is used to perform a preliminary uncoupling of the two degree of freedom as described in [28]. Two position sensing photodiodes receive the optical signals carrying information on tilt and translation of the suspended mass/mirror.

### 3.4 The diagonalization results

The preliminary tests are been performed on the simple pendulum previously described. In this case the signal we send to EA are  $EA_R$  and  $EA_L$  (we use

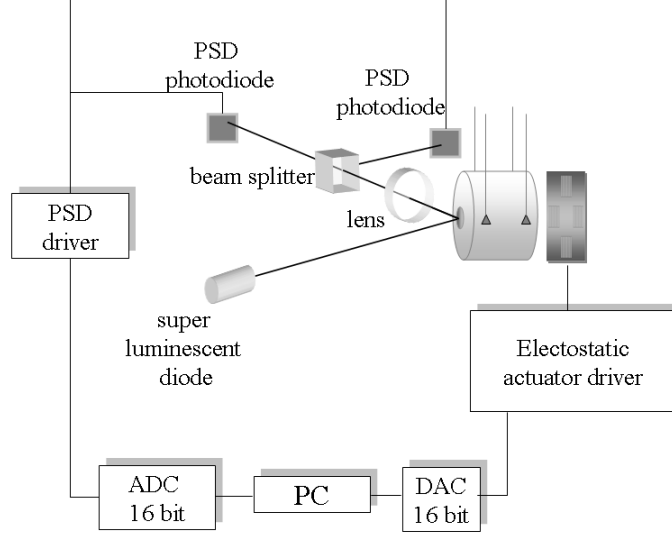


Figure 3.3: System composed by electrostatic actuators and optical lever used to additionally test the diagonalization procedure

only two horizontal electrodes among four available electrodes stripes). Electrostatic actuators are able to excite the suspended mass and two photodiodes ( $Pd_1$  and  $Pd_2$ ) will detect movements of the mirror. Exiting one electrode at time using white noise we are able to measure matrices transfer functions  $R_{ij}(s)$ .

$$\begin{pmatrix} Pd_l \\ Pd_2 \end{pmatrix} = \begin{pmatrix} R_{11}(s) & R_{12}(s) \\ R_{21}(s) & R_{22}(s) \end{pmatrix} \cdot \begin{pmatrix} EA_R \\ EA_L \end{pmatrix}$$

Defining sensing matrix  $\mathcal{S}$  and driving matrix  $\mathcal{D}$  as:

$$\begin{pmatrix} Pd_x \\ Pd_\theta \end{pmatrix} = \mathcal{S} \cdot \begin{pmatrix} Pd_1 \\ Pd_2 \end{pmatrix}$$

where  $Pd_x$  and  $Pd_\theta$  are disentangled *virtual* sensors signals. and

$$\begin{pmatrix} EA_R \\ EA_L \end{pmatrix} = \mathcal{D} \cdot \begin{pmatrix} EA_x \\ EA_\theta \end{pmatrix}$$

where  $EA_x$  and  $EA_\theta$  are disentangled *virtual* actuator signals.

Using sensing matrix  $\mathcal{S}$  and driving matrix  $\mathcal{D}$  previously defined it is easy to find:

$$\begin{pmatrix} Pd_x \\ Pd_\theta \end{pmatrix} = \mathcal{S} \cdot R_{ij}(s) \cdot \mathcal{D} \begin{pmatrix} EA_x \\ EA_\theta \end{pmatrix}$$

And:

$$\mathcal{S} \cdot R(s) \cdot \mathcal{D} = \mathcal{H} \quad (3.4)$$

Where  $\mathcal{H}$  is the matrix transfer function with diagonal form we are looking for.

An example of real transfer function is depicted in figure (3.4):

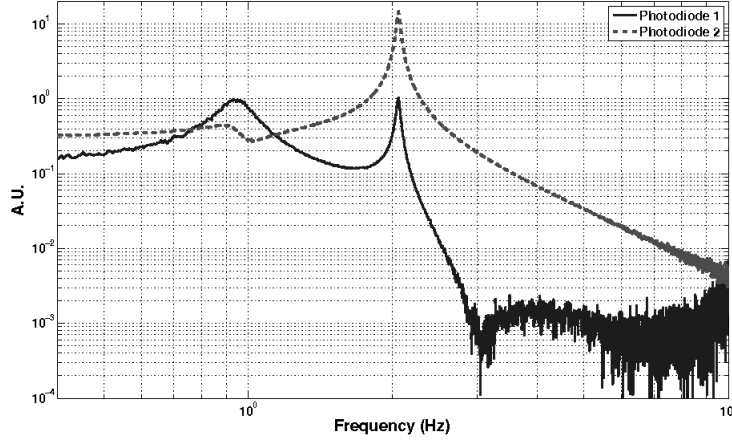


Figure 3.4: Transfer functions obtained exciting the mirror using the right electrodes of the EA [25]

Taking into account this nomenclature, the sensing matrix found is:

$$\mathcal{S} = \begin{pmatrix} 0.998 & 0.0702 \\ -0.186 & 0.983 \end{pmatrix} \quad (3.5)$$

At the same time the procedure found the driving matrix:

$$\mathcal{D} = \begin{pmatrix} 0.621 & 0.64 \\ 0.828 & -0.813 \end{pmatrix} \quad (3.6)$$

Taking into account the previous matrices (3.5) and (3.6) it is possible to build virtual sensor signals and virtual actuator signals. Applying those

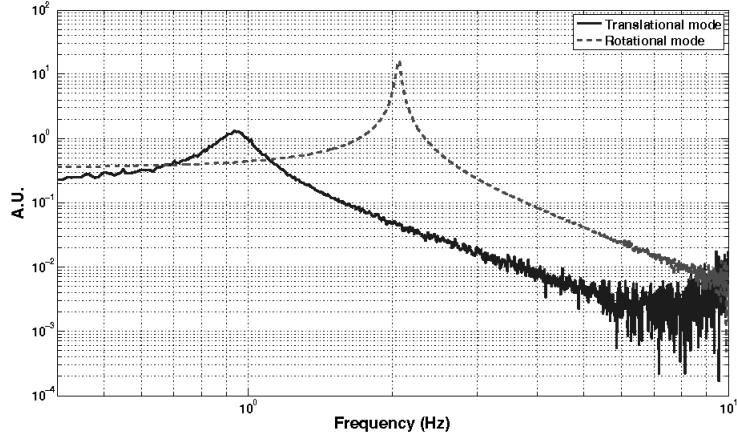


Figure 3.5: Diagonalized transfer function in the optical lever system [25]

results on our system has been possible to disentangle the degrees of freedom as shown in figure (3.5).

After the preliminary tests on a single stage pendulum, the procedure has been applied on a more complex system: the IP previously described.

In this case, LVDT are sensors used to detect the IP motion and magnet-coil systems are actuators. Each sensor should be sensitive to movements in all three IP normal modes. In the same way, each actuator will generate movements of the IP involving a mix of the three modes. In the following we will call the IP normal modes  $x$ ,  $z$  and  $R\theta$  although they do not correspond necessarily to orthogonal translations and a rotation. If the system would have been perfectly symmetrical, we would notice a degeneration in the translational modes. In a real system the two translational modes are almost degenerate.

An example of entangled system is shown in figure (3.6). In the same figure it is possible to notice the almost degeneration in the translational modes.

Using the method described in the previous section, we have found the LVDT sensing matrix  $\mathcal{S}$ :

$$\begin{pmatrix} L_x \\ L_z \\ L_{R\theta} \end{pmatrix} = \begin{pmatrix} -0.556 & -0.045 & 0.83 \\ 0.357 & -0.798 & 0.486 \\ -0.829 & -0.526 & -0.188 \end{pmatrix} \cdot \begin{pmatrix} L_1 \\ L_2 \\ L_3 \end{pmatrix}$$

And the driving matrix  $\mathcal{D}$ :

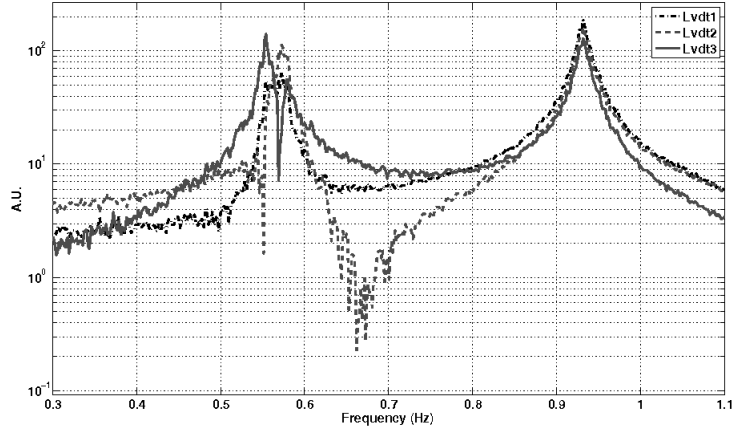


Figure 3.6: Real LVDT transfer function obtained exciting the system by means of real actuator (Coil 3). The translational peaks (0.55 Hz and 0.58 Hz) are almost degenerate [25]

$$\begin{pmatrix} C_1 \\ C_2 \\ C_3 \end{pmatrix} = \begin{pmatrix} 0.0002 & -0.816 & 0.591 \\ 0.528 & 0.4903 & 0.783 \\ -0.868 & 0.306 & 0.265 \end{pmatrix} \cdot \begin{pmatrix} C_x \\ C_z \\ C_{R\theta} \end{pmatrix}$$

The diagonalization results obtained (sensing and driving matrices) can be experimentally evaluated and compared with the diagonalization procedure prediction. Such a prediction is simply obtained combining real actuator and real sensor signals using driving and sensing matrices.

This comparison is shown in the following figure (3.7).

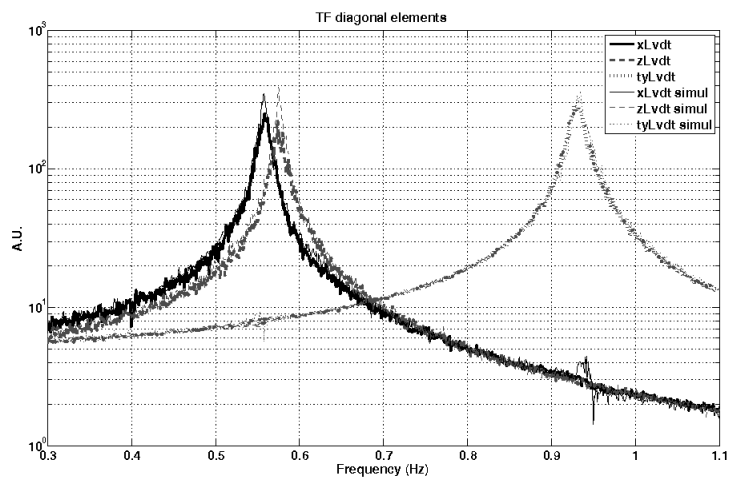


Figure 3.7: Transfer function comparison between measurements results and predicted behavior obtained using diagonalization procedure results (*simul* in the label) [25]

# Chapter 4

## Control design

### 4.1 Transfer function measurements

As usual, the first step in the control design consists in the transfer function measurement of the system we wish to control. Exciting the system with white noise (filtered at 20 Hz) along natural modes of the system ( $x$ ,  $z$ , and  $R\theta$ ) direction we obtain:

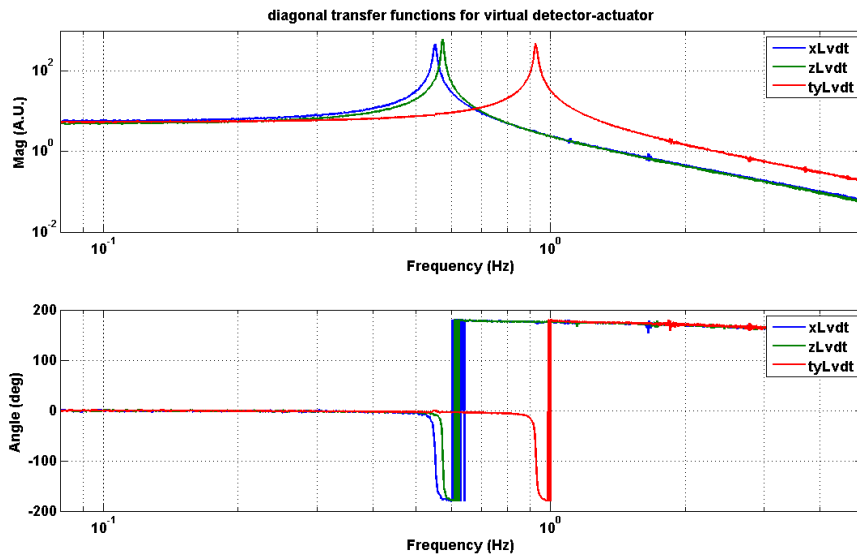


Figure 4.1: Transfer function obtained exciting the system along its eigenmodes.

From the figures it is also possible determining the mode frequencies for each degree of freedom. For this purpose, a MATLAB script has been used

to evaluate the mode frequencies and the respective quality factors. The function used to evaluate such a parameters was *fregs*.

In the following figures some comparison between experimental data and fits are shown for each mode.

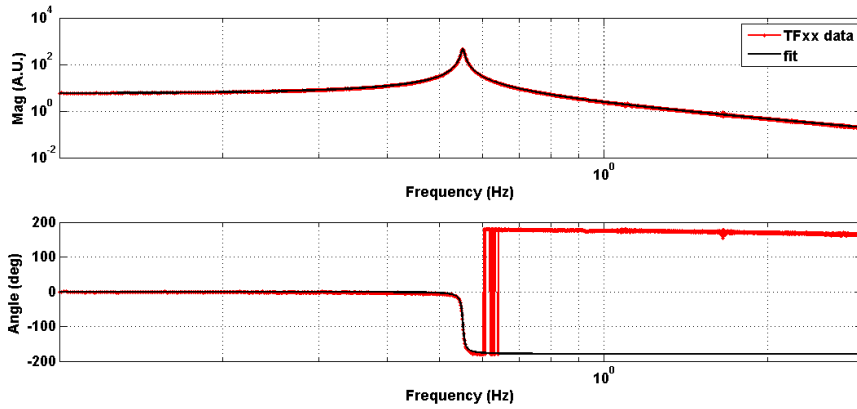


Figure 4.2: Transfer Function obtained exciting the  $x$  mode (measured data and fit).

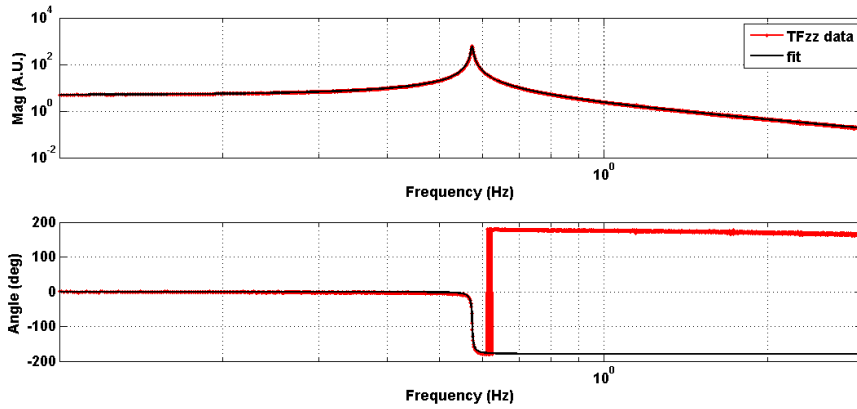


Figure 4.3: Transfer Function obtained exciting the  $z$  mode (measured data and fit).

This resonance frequencies are summarized in the following tabular:

Mode	Frequency (Hz)	Quality factor
$x$	0.551	162
$z$	0.573	254
$R\theta$	0.926	177

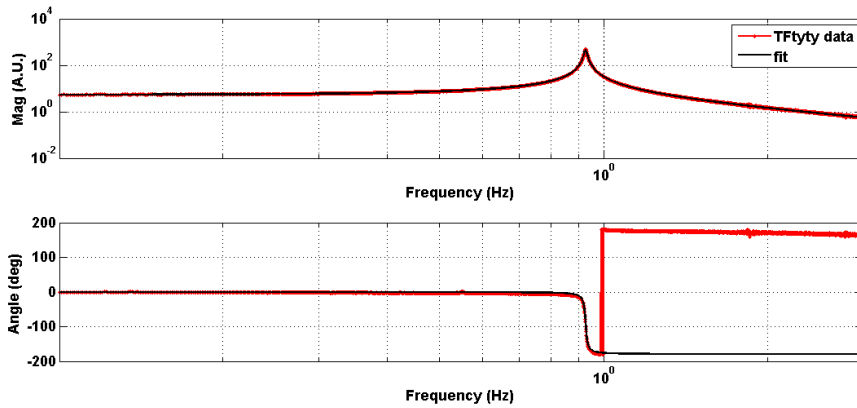


Figure 4.4: Transfer Function obtained exciting the  $R\theta$  mode (measured data and fit).

## 4.2 The control design

When the system can be considered uncoupled into three independent oscillator each provided with its own virtual sensor and actuator, it is possible to define a control strategy for a single degree of freedom system. The logic scheme of the system is described in the figure (4.5) where  $G(s)$  is the transfer function of a single degree of freedom of the IP and  $C(s)$  is the controller transfer function:

Observing the magnitude plot of the system response described in the previous section, we can notice the typical behavior of a second order system for each mode: at low frequencies we have a constant gain, while, for frequencies higher than the resonant frequency, the gain decrease to the increasing of the frequency at the resonant frequency we have a peak in magnitude (as shown in the previous tabular).

A possible way to control such a kind of system could be a zero/pole placement to compensate the presence of the resonance poles. The general scheme adopted (for each mode) has the purpose to obtain a loop gain transfer function  $G(s) \cdot C(s)$ , with high gain in DC, high gain on the resonance and a fair bandwidth.

Summarizing, the scheme is the following:

- A single pole in the origin to have a null position error.
- A double zero before the resonance peak to damp it.
- To preserve the physical reliability of our control system and to mitigate noises in high frequency range, we insert a double pole at a frequency

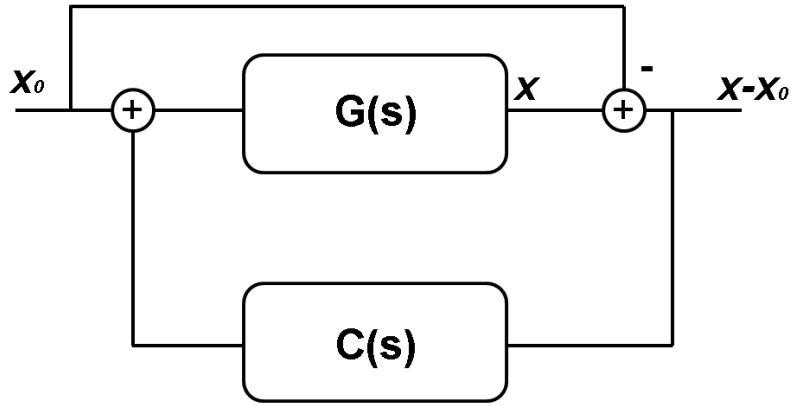


Figure 4.5: Logic scheme of the system.

well above the frequency mode and obviously before the limit of the band of the system.

In particular, the longitudinal digital control system is characterized by a pole at 0 Hz, two zeros at 0.35 Hz with quality factor  $Q = \frac{1}{\sqrt{2}}$  and two poles at 100 Hz with same quality factor  $Q = \frac{1}{\sqrt{2}}$ . The controller devoted to damp rotational is characterized by a pole at 0 Hz, two zeros at 0.8 Hz with quality factor  $Q = \frac{1}{\sqrt{2}}$  and two poles at 100 Hz with quality factor  $Q = \frac{1}{\sqrt{2}}$ . The corresponding the transfer functions are shown in figure (4.6) and (4.7) respectively for longitudinal modes and rotational mode.

The loop gain transfer function  $G(s) \cdot C(s)$  shows that the closed loop system is stable.

To test the control performances, spectral density measurement has been carried out in open and closed loop in all three cases. Results are shown in figures (4.11), (4.12) and (4.13)

### 4.3 Sensor blending

The diagonalization procedure described in *Chapter3* can be used obviously on the accelerometers also. Once diagonalized the accelerometer signals the control strategy follows an additional step: the *sensor blending*.

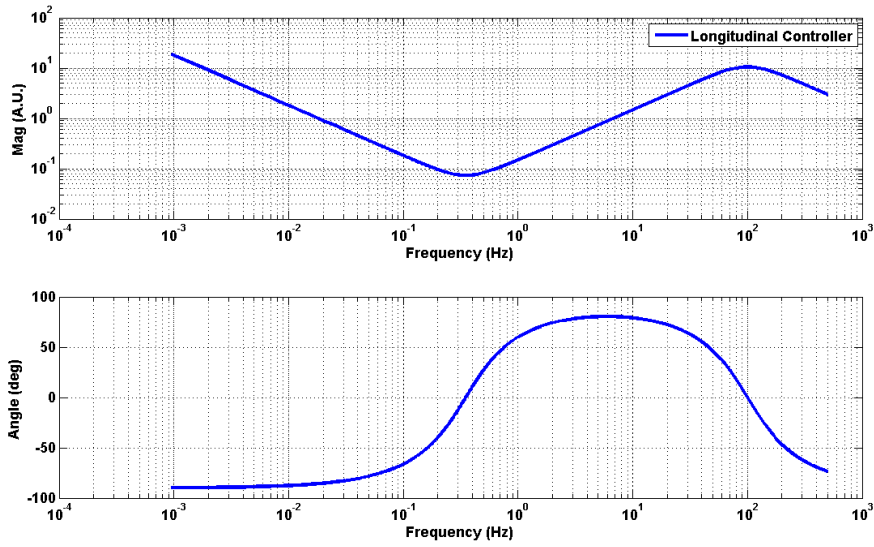


Figure 4.6: Transfer function of the longitudinal mode controller.

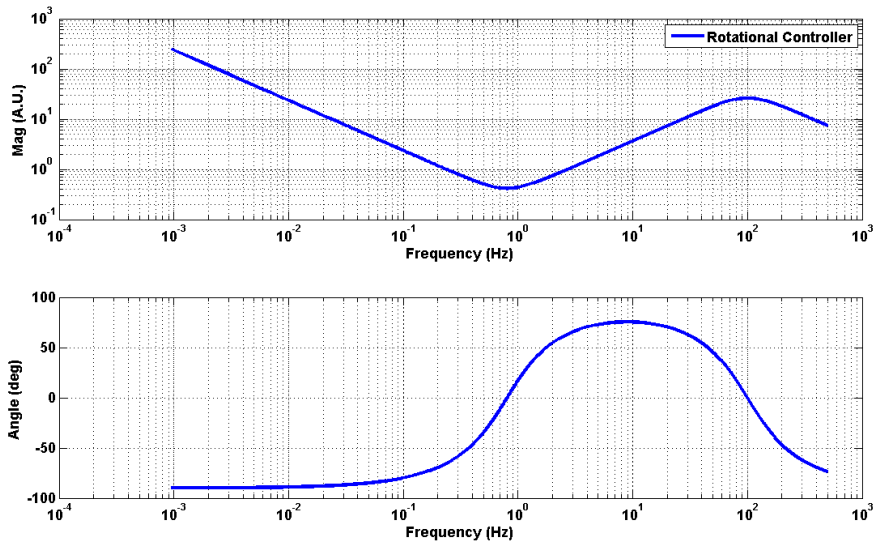


Figure 4.7: Transfer function of the rotational mode controller .

The basic idea of inertial damping is to use the accelerometer signal to build up the feedback force.

By using only the inertial sensor information would null the acceleration of the inverted pendulum but it would do nothing if the pendulum moved at

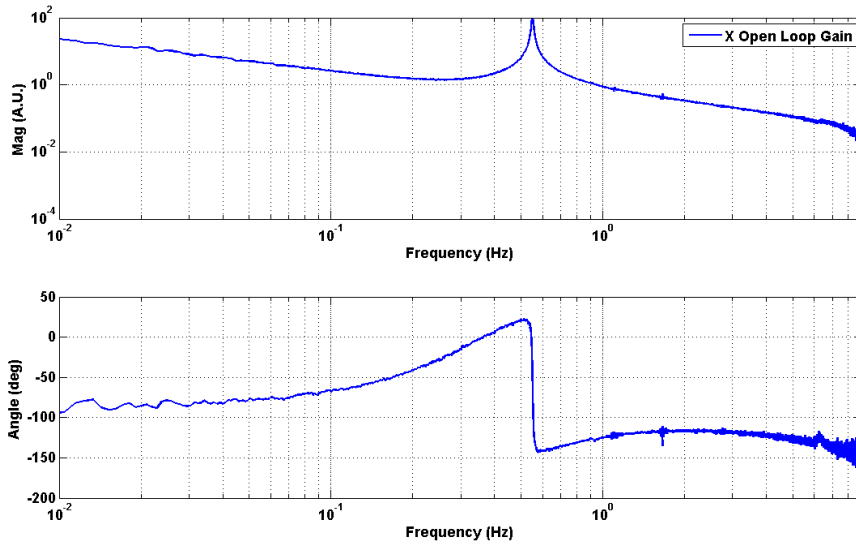


Figure 4.8: Loop gain transfer function  $G(s) \cdot C(s)$  for the  $x$  mode.

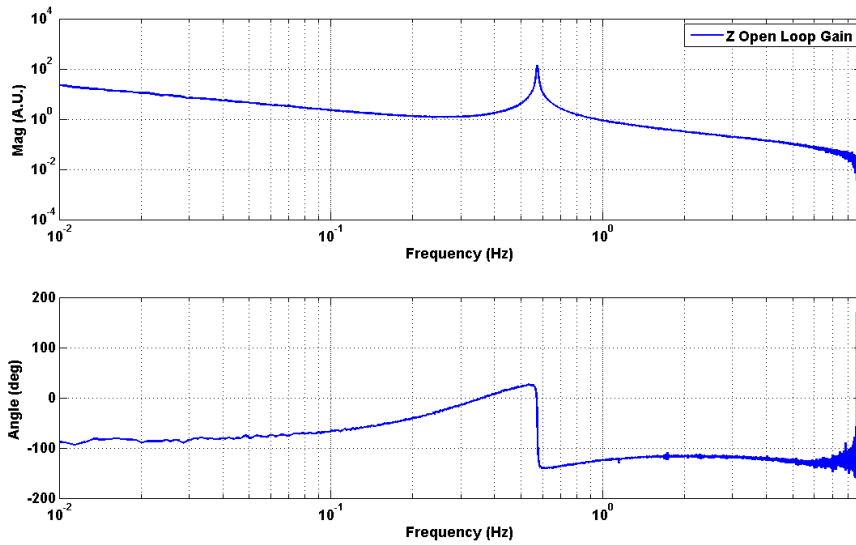


Figure 4.9: Loop gain transfer function  $G(s) \cdot C(s)$  for the  $z$  mode.

constant velocity. In other words, as obvious, the accelerometers are sensitive to acceleration but absolutely blind to IP position drifts. This is the reason why position sensors are also necessary to perform a correct control. To take into account both of the information provided from the two sensor systems

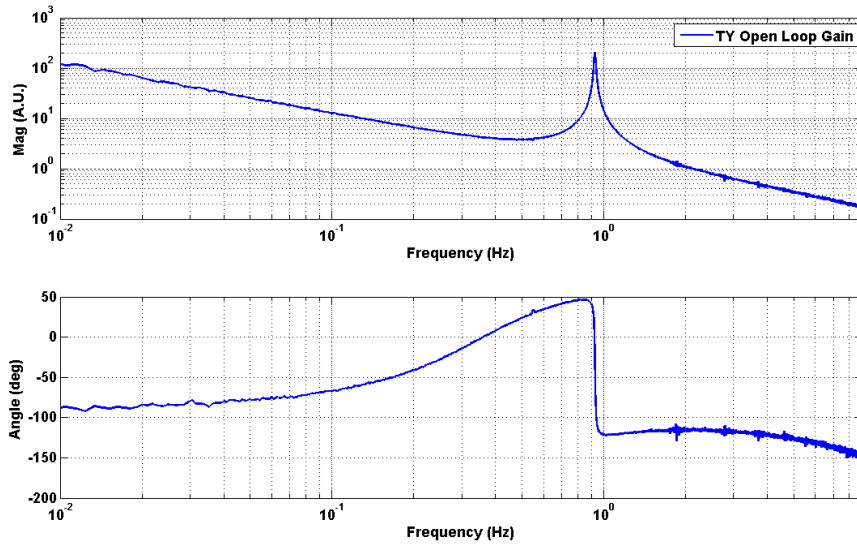


Figure 4.10: Loop gain transfer function  $G(s) \cdot C(s)$  for the  $R\theta$  mode.

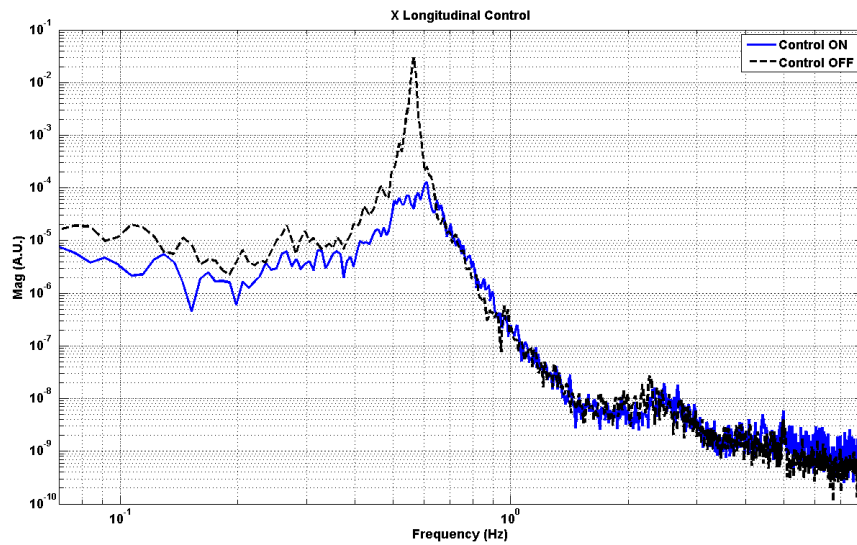


Figure 4.11:  $x$  mode spectral density measurement in open and closed loop.

it is possible to merge the sensor signals.

The virtual LVDT (position) and accelerometer signals are combined in such a way that the LVDT signal  $l(s)$  dominates below a chosen crossover frequency  $f_{merge}$  while the accelerometer signal  $a(s)$  dominates above it.

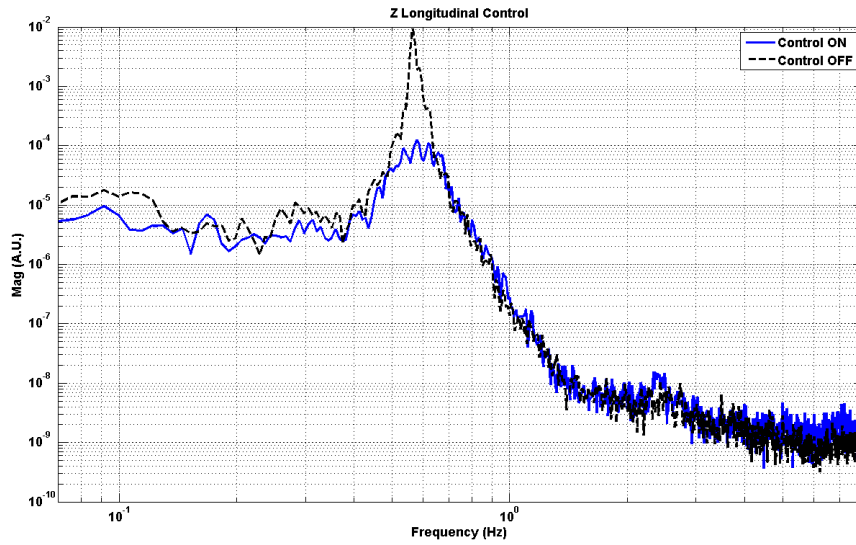


Figure 4.12:  $z$  mode spectral density measurement in open and closed loop.

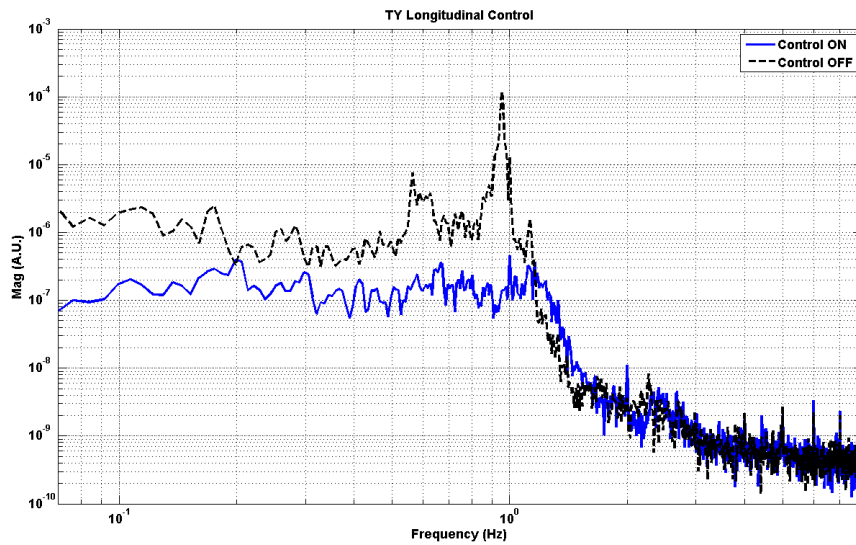


Figure 4.13:  $R\theta$  mode spectral density measurement in open and closed loop.

This task is easily accomplished by using digital filters.

The two kind of signals (position and acceleration) are blended using a low pass filter  $L(s)$  for virtual LVDT signals and an high pass filter  $H(s) = 1 - L(s)$  for virtual accelerometer signals as shown in figure (4.14).

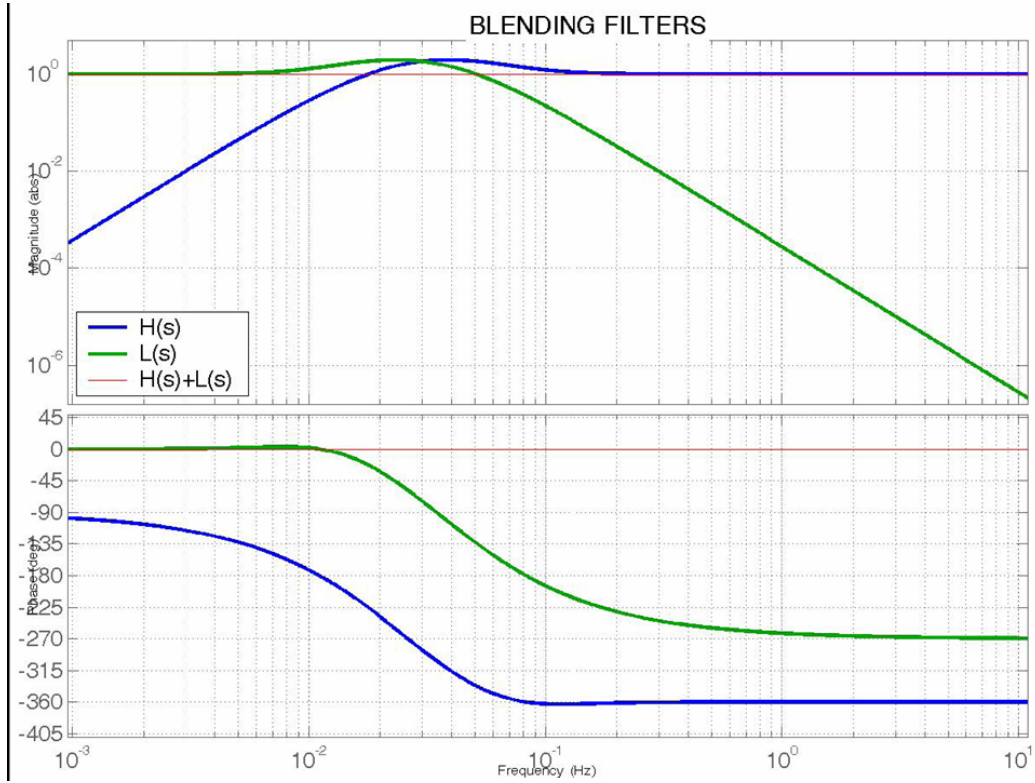


Figure 4.14: The filters used for the sensor blending. The LVDT is filtered through  $L$  ( $L \sim f^{-3}$  above  $30mHz$ ). The accelerometer is filtered through  $\frac{H}{s^2}$ .  $L$  and  $H$  are such that  $L + H = 1$ .

In this way a composite signal (*modal sensor*) can be defined as:

$$sens_{mod}(s) = L(s) \cdot Lvd_{t_{mod}}(s) + \frac{H}{s^2} \cdot Acc_{mod} \quad (4.1)$$

where  $mod = x, z, R\theta$  is the mode label.

The use of virtual modal sensor allowed the results showed in figure (4.15).

Using this new virtual modal sensor it is possible to design a digital control system.

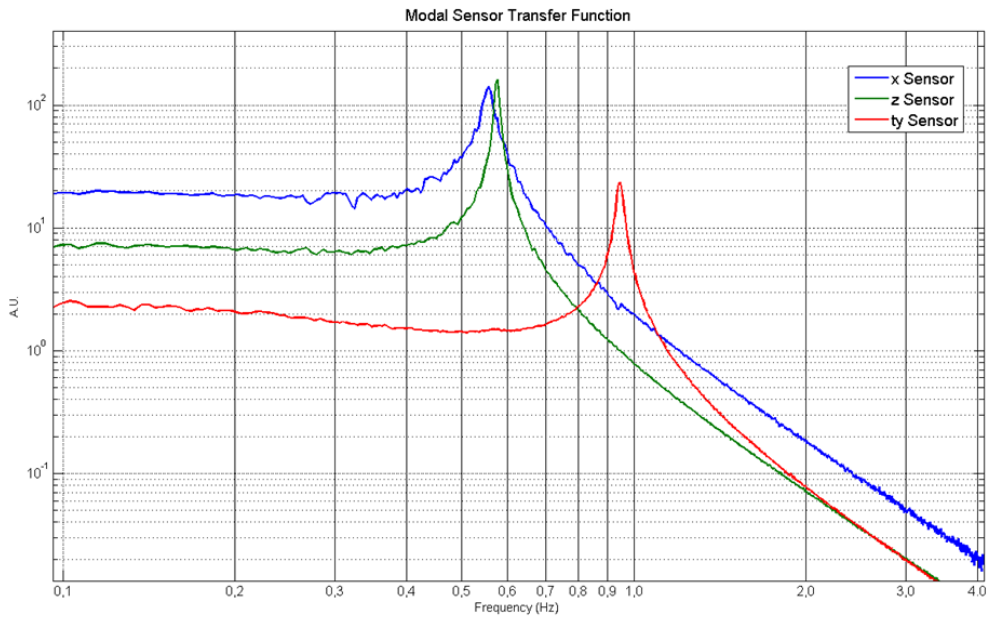


Figure 4.15: Modal sensor transfer functions.

# Chapter 5

## Mechanics of the accelerometer

Accelerometers have a long history as sensors used in gravitational wave detectors. They are special purpose device, expressly designed to instrument the seismic attenuation system but the initial design was inspired by geophysical devices. In fact, their mechanical structure could make use, sometimes, of the so-called *folded pendulum* (FP) which will be described in this chapter. It is remarkable that, nowadays, accelerometers developed for the gravitational wave field could be revealing useful in the geophysics field (as it will be described in a next chapter) that in somehow originated them.

The requirement for our accelerometers (not satisfied from commercial devices) are the following:

- *Strong directionality.* As we have seen before, their main purpose is to perform inertial damping providing signals to be used in the control of the pendula chain. But any MIMO control strategy requires true singleaxis accelerometers. For this reason, a basic constraint in designing the mechanics is to make the instrument as insensitive as possible to all the other five d.o.f. A geometric crosstalk also degrades the resolution of the accelerometer.
- *Very sensitive in the low frequency range.* The performance of an accelerometer is closely related to its resonant frequency; a softer mechanics allows an increase in the low frequency resolution proportionally to  $f_0^2$ . A natural period of a few seconds is needed to achieve subnanometer accuracy around the microseismic peak ( $150mHz$ ), using the best available position sensors.
- *High mechanical quality factor.* Mechanics makes the instruments feedback operation easier, since the ringing rise-time is slower ( $\tau = 2Q/\omega_0$ ); it also prevents hysteresis because a high Q corresponds to low friction

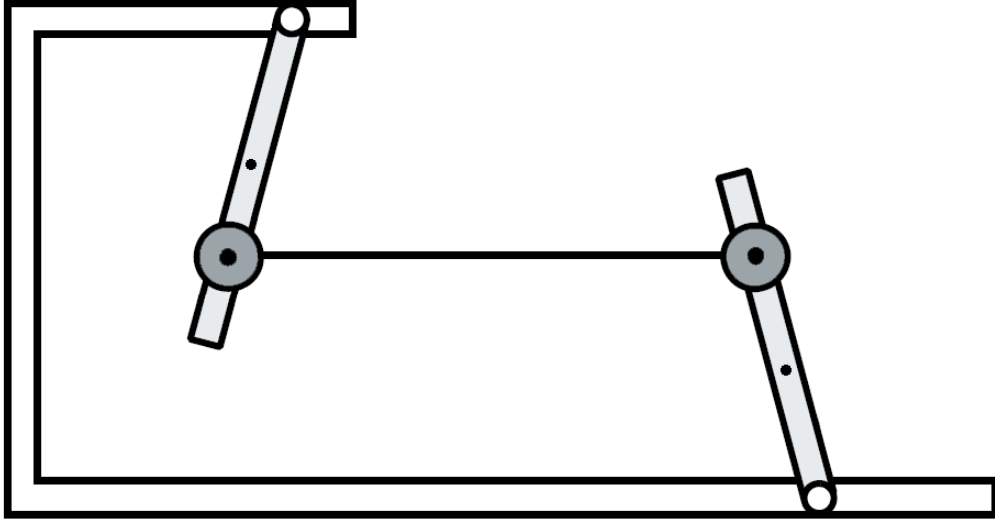


Figure 5.1: Basic scheme of the folded pendulum. Both the arm and the horizontal bar are considered with mass, the points represents the center of mass of the single elements.

between different parts of the instrument and low creep of the elastic elements. As a further benefit nonlinearities in the device output are reduced.

- *High vacuum compatibility.* The whole interferometer works in high vacuum conditions. The reasons are several: to reduce air index refraction fluctuations, air scattering, to isolate mirror from acoustical environment, to reduce thermal noise produced by air dumping.

All those requirements could be satisfied adopting a *folded pendulum* geometry, along with a monolithic design preserving, at the same time, a compact, rugged and allmetal structure.

## 5.1 Folded pendulum

The folded pendulum briefly described in the second chapter deserves some additional detail because of the large use of this particular structure in the design of new acceletometers.

This mechanical structure, also called Watt-linkage, is a system developed in 1962 [33], recently rediscovered for applications who require the study of

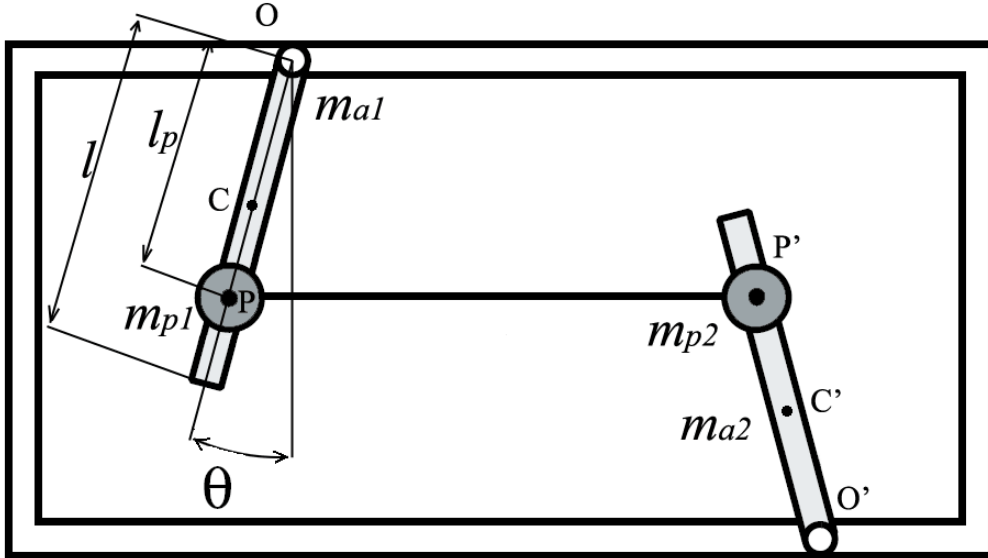


Figure 5.2: Equivalent diagram of the folded pendulum.

ultra-low frequency phenomena [26]. In fact, a monolithic mechanical design has the great advantage of avoiding the shear effects at the contact surface among mechanical parts that can generate hysteresis and dissipation, resulting in a very compact sensor, with characteristics of low thermal dissipation, high Q-factor and very good directionality: coupling factors of less than  $10^{-4}$  among the different degrees of freedom have been obtained in monolithic structures [34]. They and are presently used in our laboratory to perform inertial damping. This broadband singleaxis monolithic folded pendulum shows natural frequencies of  $700mHz$ .

We can schematize the folded pendulum structure as it is shown in figure (5.1). A simple pendulum is connected by means of a rigid massively bar to an inverted pendulum. Theoretically, this configuration allows an equilibrium position without the necessity to introduce elastic restoring force (that means no material stress) and the only restoring force is the gravitational one.

In addition this configuration could produce an arbitrary low resonant frequency, by changing opportunely the mass of the system components.

To better understand the mechanics of the folded pendulum, let consider the figure (5.2).

As already said, it consists of two arms, a simple pendulum of mass  $m_{a1}$

on the left and an inverted pendulum of mass  $m_{a2}$  on the right, connected by means of a rigid bar, whose mass is modelled as shared into two equivalent point masses  $m_{p1}$  and  $m_{p2}$ , respectively placed on the single pendulum and inverted pendulum arms. The two arms have, as pivot point, the points  $O$  and  $O'$ , same length  $l$ , and the two mass  $m_{p1}$  and  $m_{p2}$  are placed at the same distance  $l_p$  from the points  $O$  and  $O'$ ; the points  $C$  and  $C'$  are the center of the the two arms. The bar is hinged to the two arms in the center of the two masses  $m_{p1}$  and  $m_{p2}$ , named  $P$  and  $P'$  respectively. The points  $O$ ,  $O'$ ,  $P$ ,  $P'$ ,  $C$  and  $C'$  have coordinates  $x_O$ ,  $x_{O'}$ ,  $x_P$ ,  $x_{P'}$ ,  $x_C$  and  $x_{C'}$  respectively, and  $\theta$  and  $\theta'$  are the two angle from the vertical positions. In the approximation of small oscillations (little angle of deflections of the vertical arms) we can consider  $\theta \approx \theta'$ ,  $\dot{x}_C \approx \dot{x}_{C'}$  and  $\dot{x}_P \approx \dot{x}_{P'}$ .

To solve the Lagrange equation of the system [26] we can write the kinetic energy  $T$  as:

$$T = \frac{1}{2}(I_1 + I_2)\dot{\theta}^2 + \frac{1}{2}(m_{a1} + m_{a2})\dot{x}_C^2 + (m_{p1} + m_{p2})\dot{x}_P^2 \quad (5.1)$$

and the potential energy  $V$  (which has only gravitational origin) as:

$$V = 2(m_{p1} + m_{a1})lg - \frac{1}{2}(m_{a1} - m_{a2})lg \cos \theta - (m_{p1} - m_{p2})l_p g \cos \theta \quad (5.2)$$

where  $I_1$  and  $I_2$  are the moments of inertia of the two arms around the perpendicular axes through their mass center  $C$  and  $C'$  respectively. Let consider a force  $f$  applied directly on the pendulum platform in the  $x$  direction, and two forces,  $f_{x1}$  and  $f_{x2}$  applied at the ends of the two pendulum arms, in the pivot points  $O$  and  $O'$  (an earthquake, for example).

The corresponding potential of the horizontal forces will be:

$$U = - \int (f_{x1} + f_{x2}) dx_O - \int f dx_P \quad (5.3)$$

In order to write the Lagrangian expression  $L = T - V - U$  as a function of only two variables,  $x_O$  and  $x_P$ , we can introduce the following terms:

$$x_C = x_O - \frac{1}{2}l\theta \quad \theta = \frac{x_O - x_P}{l_p} \quad I_1 = \frac{1}{12}m_{a1}l^2 \quad I_2 = \frac{1}{12}m_{a2}l^2 \quad (5.4)$$

By solving the Lagrange equations

$$\frac{d}{dt} \frac{\partial L}{\partial \dot{x}_O} - \frac{\partial L}{\partial x_O} = 0 \quad \text{and} \quad \frac{d}{dt} \frac{\partial L}{\partial \dot{x}_P} - \frac{\partial L}{\partial x_P} = 0 \quad (5.5)$$

and merging the two equations into one to have  $f_{x1} + f_{x2}$ , by retaining only first order terms, we can express the last as

$$\begin{aligned}
& - \left[ \frac{1}{3}(m_{a1} + m_{a2})\frac{l^2}{l_p} + (m_{p1} + m_{p2})l_p \right] \ddot{x}_P + \\
& + \left[ \frac{1}{3}(m_{a1} + m_{a2})\frac{l^2}{l_p} - \frac{1}{2}(m_{a1} + m_{a2})l \right] \ddot{x}_O = \\
& = - \left[ \frac{1}{2}(m_{a1} - m_{a2})\frac{l}{l_p} + (m_{p1} - m_{p2}) \right] \cdot (x_O - x_P)g - l_P f
\end{aligned} \tag{5.6}$$

Then, let assume that  $f = Fe^{i\omega t}$ ,  $x_O = X_O e^{i\omega t}$ ,  $x_P = X_P e^{i\omega t}$  and set  $x_O = 0$  and  $f = 0$  respectively for force excitation and base excitation.

The force excited and base excited transfer functions of the folded pendulum can be given in forms similar to those of a simple pendulum

$$\frac{X_P}{F} = \frac{1}{M_e \omega_0^2 \left(1 - \frac{\omega^2}{\omega_0^2}\right)} \tag{5.7}$$

$$\frac{X_P}{X_O} = \frac{1 - A_c \frac{\omega^2}{\omega_0^2}}{1 - \frac{\omega^2}{\omega_0^2}} \tag{5.8}$$

where

$$M_e = \frac{1}{3}(m_{a1} + m_{a2})\frac{l^2}{l_p} + (m_{p1} + m_{p2}) \tag{5.9}$$

$$\omega_0^2 = \frac{(m_{a1} - m_{a2})\frac{l}{2l_p} + (m_{p1} - m_{p2})\frac{g}{l_p}}{(m_{a1} + m_{a2})\frac{l^2}{3l_p^2} + (m_{p1} + m_{p2})\frac{l_p}{l}} \tag{5.10}$$

$$A_c = \frac{\left(\frac{l}{3l_p} - \frac{1}{2}\right)(m_{a1} + m_{a2})}{(m_{a1} + m_{a2})\frac{l}{3l_p} + (m_{p1} + m_{p2})\frac{l_p}{l}} \tag{5.11}$$

in which we can see that if  $A_c = 0$  the folded pendulum is equivalent to a simple pendulum with an equivalent mass  $M_e$  and equivalent length:

$$l_e = \frac{(m_{a1} + m_{a2})\frac{l^2}{3l_p^2} + (m_{p1} + m_{p2})}{(m_{a1} - m_{a2})\frac{l}{2l_p^2} + (m_{p1} - m_{p2})} l_p \tag{5.12}$$

By changing opportunely the values of the masses  $m_{a1}$ ,  $m_{a2}$ ,  $m_{p1}$  and  $m_{p2}$  we can, in principle, obtaining any equivalent length, that is the same to say any arbitrarily low resonant frequency.

Now, let consider two extreme cases of the folded pendulum design. In a first case, let suppose the pendulum as dominated by the mass  $m_{p1}$ . This corresponds to consider:

$$m_{p1} \gg m_{a1}, m_{a2}, m_{p2} \quad (5.13)$$

Using the condition (5.13) into the (5.10) we obtain:

$$\omega_0 = \sqrt{\frac{g}{l_p}} \quad (5.14)$$

Thence, the condition (5.13) corresponds to degenerate the folded pendulum into a simple pendulum.

In the second case, let consider the folded pendulum dominated by  $m_{a1}$ . This corresponds to consider:

$$m_{a1} \gg m_{a2}, m_{p1}, m_{p2} \quad (5.15)$$

Using the condition (5.15) into the (5.10) we obtain the frequency of a bar with a fixed extreme

$$\omega_0 = \sqrt{\frac{3g}{2l}} \quad (5.16)$$

By observing the expressions (5.7) and (5.8) it is easy to recognize that the folded pendulum and the simple pendulum have the same form for the force excited transfer function.

In contrast the base excited transfer function shows a different behavior because of the presence of the term  $A_c \omega^2 / \omega_0^2$  in the numerator of the (5.8).

Obviously when  $A_c \rightarrow 0$  the folded pendulum behavior approaches the simple pendulum one.

A simple simulation in figure (5.3) shows the variation of the transfer function for different values of  $A_c$ .

The factor  $A_c$  originates from the fact that the two arms of the folded pendulum are made of rigid bars (they are physical pendula), so that the position of the hinges with respect to the arms center of mass affects the transfer function. Above a critical frequency  $f_c = \frac{\omega_0}{\sqrt{A_c}}$  by shaking the folded pendulum frame, each arm simply rotates around its own center of percussion, while the leg free-end countershakes by an amount that is a function of  $A_c$ . As a result the folded pendulum transfer function flattens above  $\frac{\omega_0}{\sqrt{A_c}}$ . In addition if  $A_c$  is positive, a zero in the transfer function will appear, as shown in figure (5.3).

In order to optimize the mechanical scheme of a folded pendulum let consider the equation (5.12). The condition  $A_c = 0$  could be realized by setting  $m_{a1} + m_{a2} = 0$  or  $l_p = \frac{2}{3}l$ .

For obvious reason it is impossible to reduce to zero the mass of the two arms.

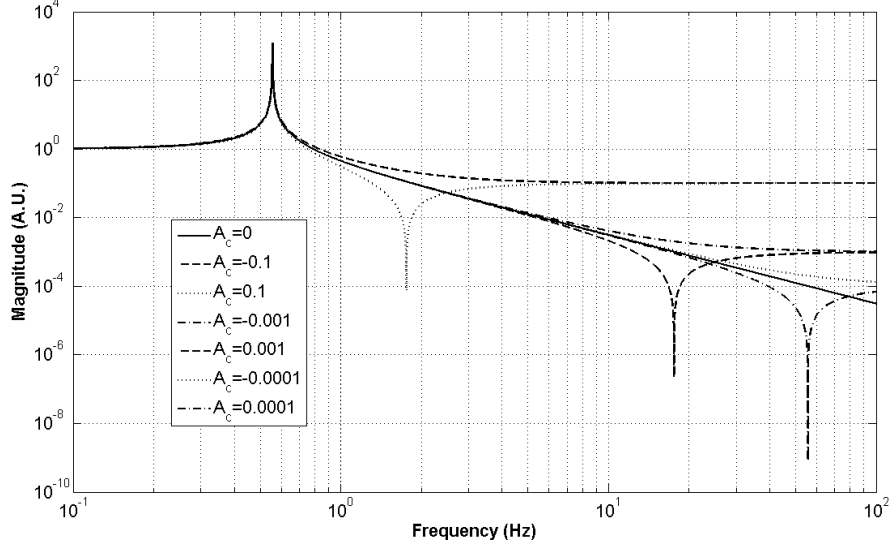


Figure 5.3: Theoretical base excited transfer function of the folded pendulum for different values of  $A_c$ .

Instead, setting  $l_p = \frac{2}{3}l$  means that the points  $P$  and  $P'$  are on the center of percussion of the two arms. This means that we can have the best isolations performance locating the flexure hinge at the center of percussion of the two arm.

### 5.1.1 Potential energy of a folded pendulum

A meaningful characteristic of the folded pendulum is related to its mechanical stability.

To this purpose, let evaluate the potential energy of the folded pendulum using a simple model as it is shown in the figure (5.4), in which we consider all the arm to be massless and we neglect the stiffness of the elastic flexure joint.

The pendulum arms have the same length  $L$  and are separated by a distance  $S$ . A mass  $M$  (the only massive element in this simple model) is placed at distance  $D$  from the simple pendulum. In this model, the resonance frequency became:

$$\omega_r^2 = \frac{g}{l} \left( 1 - 2 \frac{D}{S} \right) \quad (5.17)$$

and the potential energy is a function of the deflection angle  $\theta$  and is:

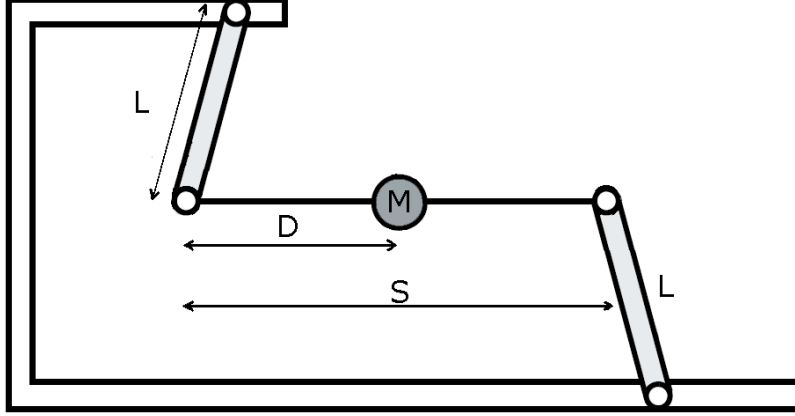


Figure 5.4: Simplified folded pendulum model for the potential energy analysis.

$$U_{pot}(\theta) = MgL(1 - \cos \theta) \left[ 1 - \frac{2}{S} \left( L \sin \theta + \sqrt{D^2 - L^2(1 - \cos \theta)^2} \right) \right] \quad (5.18)$$

As it is shown in the figures (5.5) and (5.6) we see that the folded pendulum exhibits a minimum in  $\theta = 0$  and an increasing when  $\theta > 0$  corresponding to a tilt towards the inverted pendulum arm. The graphs were designed with the length of the arm  $L = 71.5 \text{ mm}$  at a distance  $S = 102 \text{ mm}$ , while the resonant frequency was changed by moving the center of mass position  $D$ . The minimum of the potential energy is in the position  $\theta = 0$ , in this condition the two arm are parallel (corresponding to a vertical position of the arms).

We note that by changing the position of the mass  $M$  (see figure 5.4) towards values of  $\theta$  grater than the ones corresponding to the hill of the potential, the system will be instable.

Experimentally this represents a limit in the possibility to lower arbitrarily the resonance frequency of the system.

Simulations performed for different position of the mass  $M$  (corresponding therefore to different resonance frequency) show that the equilibrium condition (minimum of the potential) is more stable at higher frequencies. The figures (5.5) and (5.6) show the evidence of this behavior.

In literature [35] we can find that the maximal horizontal amplitude of the folded pendulum decrease with respect the resonance frequency as  $\sim f^{1/2}$  and

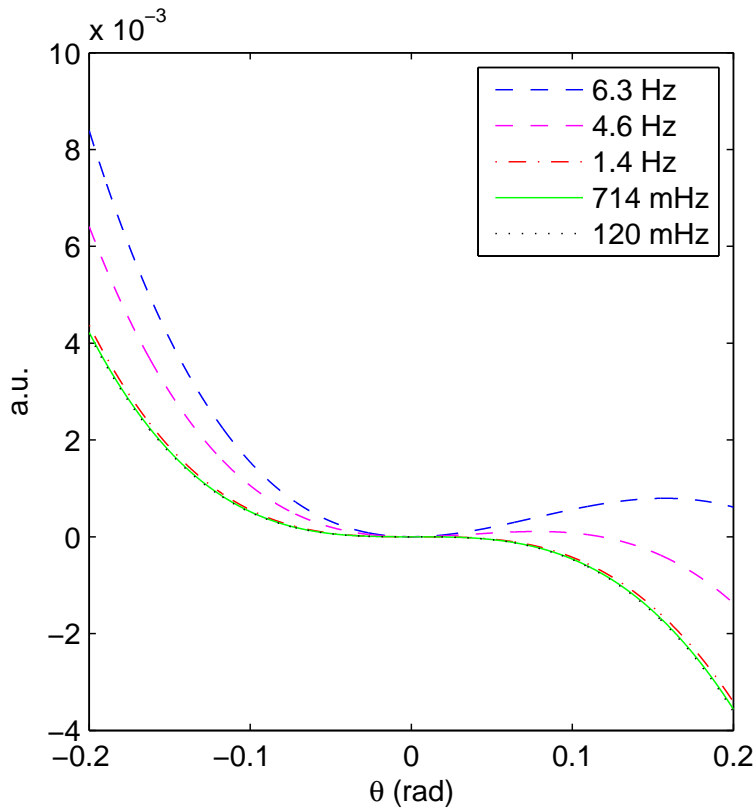


Figure 5.5: Folded Pendulum potential energy versus deflection angle  $\theta$ .

the depth of the potential well decrease as  $\sim f^3$ , so the lower is the resonance frequency the flatter is the bottom of the potential well.

## 5.2 Realistic folded pendulum mechanical model

Up to now, our considerations on the mechanical behavior of the folded pendulum have been based on an oversimplified model. But, in spite of their simplicity these models have been able to reproduce important features of the folded pendulum. Let consider a model taking into account additional parameter we need to face in a more realistic device.

### 5.2.1 Stiffness contribution

Our accelerometers, as already said, are monolithic devices and a more accurate model should take into account the stiffness of the joints connecting

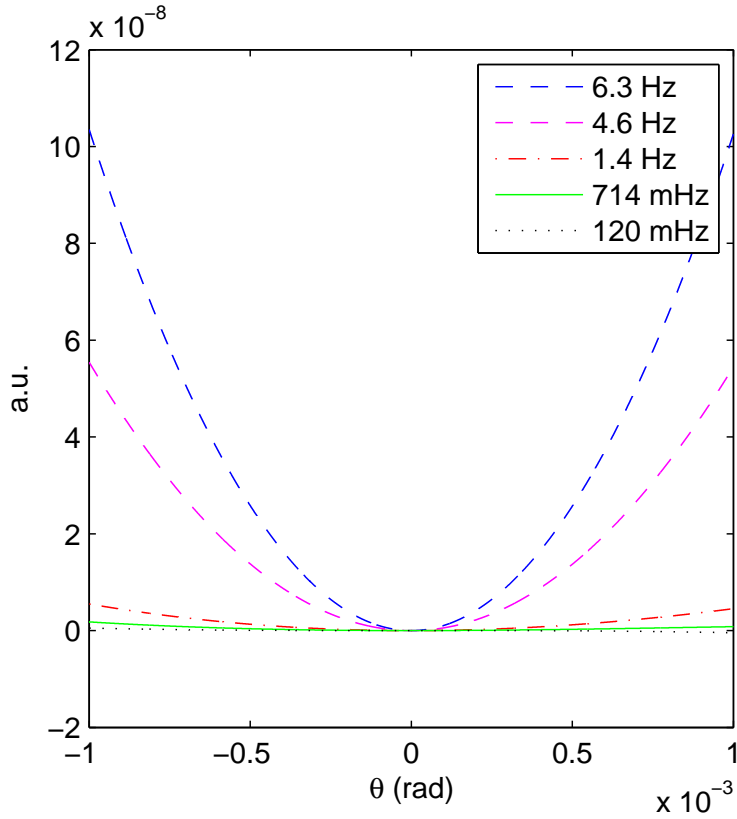


Figure 5.6: Detail, for small angle, of the folded pendulum potential energy versus deflection angle  $\theta$ .

the elements of the folded pendulum.

For this reason the expression of the potential energy (5.2) has to be replaced by the following:

$$U(\theta) = \frac{1}{2} \left( \frac{m_{a1}gl_1}{2} - \frac{m_{a2}gl_2}{2} + m_{p1}gl_{p1} - m_{p2}gl_{p2} + k \right) \theta^2 = \frac{1}{2}k\theta^2 \quad (5.19)$$

where  $\theta$  is the deflection angle and  $k$  is the cumulative stiffness of the joints.

It is possible to proceed in the same way as in section (5.1). Assuming again that the center of mass of the pendula is in  $l_i/2$  and using the approximation of small deflection angles, then the folded pendulum transfer function can be easily obtained by solving the Lagrange Equations. Defining the coordinate of the pendulum frame (fixed to the ground) as  $x_s$  and the coordinate



masses  $m_{p1}$  and  $m_{p2}$  not directly, but in an effective way, by adding a tuning mass,  $M_l$ , at a distance  $D$  from the pendulum suspension point as depicted in figure (5.7). Defining  $S$  as the distance between the folded pendulum hinges points, the values of the masses  $m_{p1}$  and  $m_{p2}$  will change according to the relations

$$m_{p1_{new}} = m_{p1_{old}} + M_l \left(1 - \frac{D}{S}\right) \quad (5.23)$$

$$m_{p2_{new}} = m_{p2_{old}} + M_l \left(\frac{D}{S}\right) \quad (5.24)$$

The new values of the masses  $m_{p1}$  and  $m_{p2}$  will change the value of the natural frequency.

Hence the folded pendulum resonance frequency can be easily modified by changing the value,  $M_l$ , and the position,  $D$ , of a tuning mass.

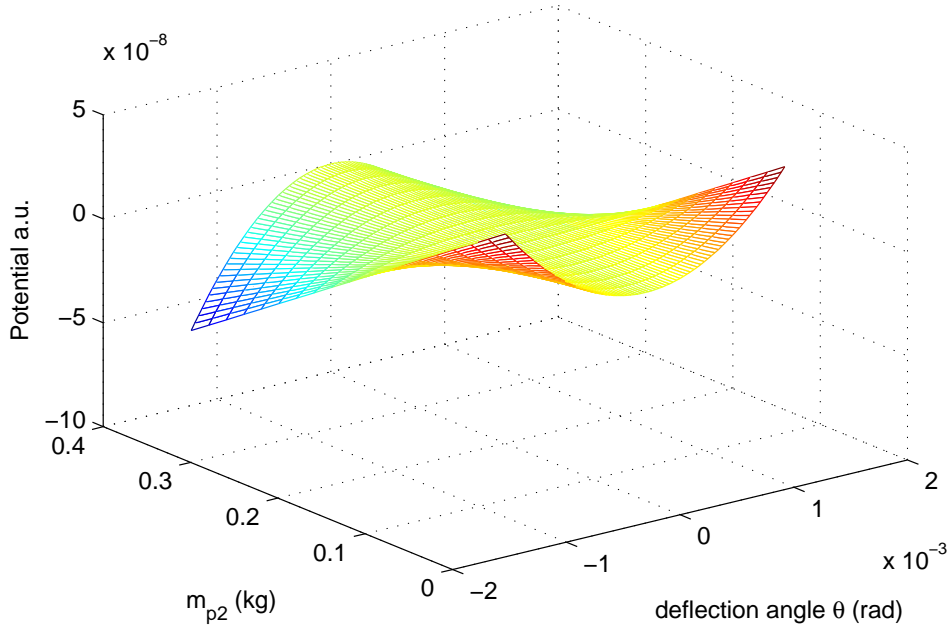


Figure 5.8: Variation of the potential as a function of the mass  $m_{p2}$ . Note the instability over a certain value of  $m_{p2}$ .

Theoretically, the calibration of the resonance frequency can be lowered to an arbitrary value: in fact by analyzing the equation (5.21), it is evident that an opportune choice of the arm mass  $m_{a1}$  and  $m_{a2}$ , and the related suspended mass  $m_{p1}$  and  $m_{p2}$  (for instance  $m_{a1} = m_{a2}$  and  $m_{p1} = m_{p2}$ ) will

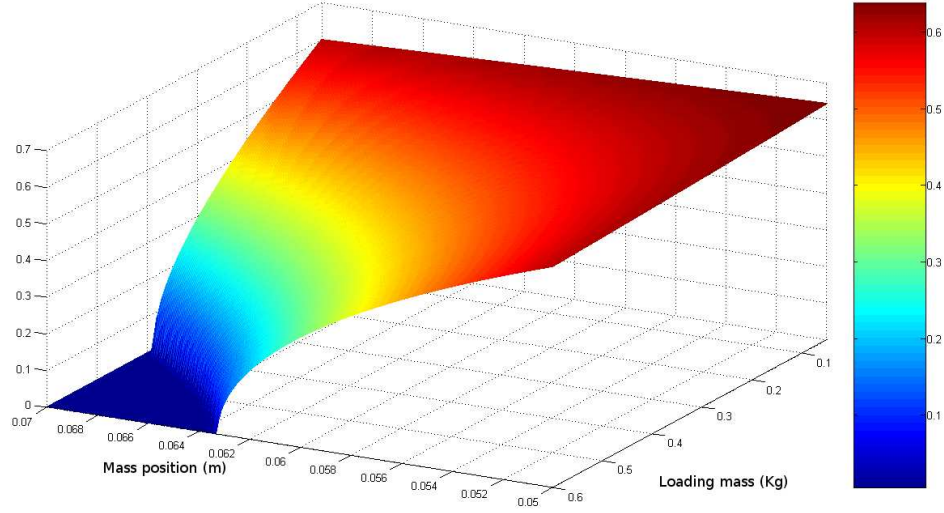


Figure 5.9: Folded pendulum resonant frequency as a function of the value of the loading mass and the position of a tuning mass.

reduce towards zero the natural frequency, having as only limit, the elastic restoring force term  $k$ ; but observing the figure (5.8) we notice a changing of the potential concavity depending on the  $m_{p2}$  values and therefore the system could become unstable (for some  $m_{p2}$  values),

This means that the choice of the tuning mass value should take into account the system mechanical stability. In figure (5.9) the frequency versus the mass position and mass load is analytically evaluated in order to show the instability region.

The mass displacement transfer function with respect to the ground displacement can be obtained by rearranging the equation (5.20) as:

$$\frac{x_p(\omega) - x_s(\omega)}{x_s(\omega)} = \frac{(1 - A_c)\omega^2}{\omega_0^2 - \omega^2} \quad (5.25)$$

This transfer function describes the dynamics of the folded pendulum as seismometer, that is the ground displacement,  $x_s(\omega)$ , as function of the measured mass displacement,  $x_p(\omega) - x_s(\omega)$ . On the other hand, in the implementation of a folded pendulum accelerometer using a force feedback design as described in section (2.7.3), the feedback force generated is proportional to the ground acceleration and, therefore, the current used to drive the actuator coil is proportional to the ground acceleration. Hence, for the folded pendulum in accelerometer configuration, it is necessary to express the mass

displacement,  $x_p(\omega) - x_s(\omega)$  as function of the ground acceleration,  $a_s(\omega)$ , as

$$\frac{x_p(\omega) - x_s(\omega)}{a_s(\omega)} = \frac{(1 - A_c)}{\omega_0^2 - \omega^2} \quad (5.26)$$

A better physical interpretation of the dependence of the folded pendulum resonant frequency from its physical and geometrical parameters, can be obtained if the equation (5.21) is rewritten as:

$$\omega_0^2 = \frac{(m_{a_1} - m_{a_2}) \frac{gl}{2l_p^2} + (m_{p_1} - m_{p_2}) \frac{g}{l_p} + \frac{k}{l_p^2}}{(m_{a_1} + m_{a_2}) \frac{l^2}{3l_p^2} + (m_{p_1} + m_{p_2})} \quad (5.27)$$

Defining the equivalent gravitational constant,  $K_g$ , as

$$K_g = (m_{a_1} - m_{a_2}) \frac{gl}{2l_p^2} + (m_{p_1} - m_{p_2}) \frac{g}{l_p} \quad (5.28)$$

the equivalent elastic constant,  $K_e$ , as

$$K_e = \frac{k}{l_p^2} \quad (5.29)$$

and the equivalent mass,  $M_e$ , as

$$M_e = (m_{a_1} + m_{a_2}) \frac{l^2}{3l_p^2} + (m_{p_1} + m_{p_2}) \quad (5.30)$$

then the FP resonant frequency,  $f_o = \frac{\omega_o}{2\pi}$ , can be rewritten as

$$f_o = \frac{1}{2\pi} \sqrt{\frac{K_g + K_e}{M_e}} \quad (5.31)$$

It is easy to recognize in the equation (5.31) the classic expression of the resonant frequency of a spring-mass oscillator with an equivalent elastic constant  $K = K_g + K_e$ .

The approach up to now followed to describe the folded pendulum dynamics is a classic steady-state approach, in which the dissipation effects have been completely neglected. But actually, the model of a real system has to face the dissipation effects, that are the real limit to the performances of a monolithic folded pendulum. These dissipation effects can be globally introduced already rewriting the equation (5.25) in the Laplace domain as:

$$\frac{x_p(s) - x_s(s)}{a_s(s)} = \frac{(1 - A_c)}{s^2 + \frac{\omega_0}{Q}s + \omega_0^2} \quad (5.32)$$

where  $Q$  is the global quality factor.

## 5.3 Mechanical design

Taking into account the characteristics and the constraints we have seen on the previous sections, a monolithic structure has been chosen in order to reduce dissipative effects produced by the friction among the folded pendulum elements. In fact, the monolithic mechanical design has the great advantage of avoiding the shear effects at the contact surface among mechanical parts that can generate hysteresis and dissipation in a non monolithic structure [26].

A correct choice of the element dimension is also able to produce a low coupling among the various system degrees of freedom, leading to a unidirectional (horizontal) accelerometer.

The monolithic sensors are obtained starting from a  $140 \times 134 \times 40 \text{ mm}$  block of metal (Alloy 7075-T6) shaped with a hybrid technique composed by precision machining and electric discharge machining (EDM).

In this technique, a thin  $250 \mu\text{m}$  wire cut is used to separate the pendulum arm, the inverted pendulum arm and the central mass from the frame. The four torsional flexures, connecting the pendulum arms to the central mass and to the frame, have an elliptical profile (for a specific reason illustrated in the subsection 5.3.3) with thickness and ellipticity (ratio between ellipse axis) depending on the model considered.

### 5.3.1 Gap opening

The tunability of the FP natural frequency represents an undoubted advantage of our sensor. The reason to pursue such a feature is that tuning the FP at its lowest possible natural frequency maximizes the sensor measurement band at low frequencies. But, the lower is the natural resonance frequency, the lower is the restoring force of the pendulum to external perturbations. Furthermore, a lower natural resonant frequency permits to relax the specifications of the control system for force feedback sensor configuration. The drawback of soft restoring forces is that the test mass easily touches the frame, saturating the sensor. Therefore, to improve the performance (with respect to the present sensor used to perform inertial damping) the gaps between the central mass-arms and arms-frame were made of  $2 \text{ mm}$  large. In this way the dynamics of the monolithic FP sensor is quite large, but still far from the elastic limit of the material. These large gaps have another advantage when the FP works in air. In fact, the mechanical quality factor  $Q$  of the instrument in air is strongly influenced by the damping effect of the air present in these gaps, that largely reduces its value.

### 5.3.2 Material choice

The choice of the material, aluminum in the present version of the accelerometers realized, give to the system the *immunity to the magnetic field*, good *thermal conductivity*, with a *low cost material*. This material is also easy to machine.

Other requirements are the *easy construction procedure* (it is relatively simple to machine this material with numerical machining devices) and the little total dimension to assure great *portability* to different work area.

Because of its monolithic nature, the folded pendulum structure is greatly conditioned by the choice of the material used. In fact, the material is important, for the *specific weight* that determine the value of the element masses composing the FP, the elasticity of the material (*Young's module*) that determines the value of the elastic part of the restoring force, the *thermal expansion* connected to the deformation with respect temperature variation and the viscosity from which depends the *loss angle*.

The material under consideration has been the aluminum for its mechanical property, its low cost and its good machining property; also the Cu-Be alloy has been considered for its good mechanical property, especially breaking strength (tensile) that permits to use a little thickness for joint realization, having a lower elastic restoring force. A brief list of the material characteristics are indicate in the follow:

	Al 7075-T6	Cu-Be C17200
Young's Module	72 <i>GPa</i>	131 <i>GPa</i>
Tensile Strength	570 <i>MPa</i>	1205 <i>MPa</i>
Thermal Expansion	23 <i>ppm/C°</i>	17 <i>ppm/C°</i>
Loss Angle	$4 \cdot 10^{-5}$ <i>rad</i>	$4 \cdot 10^{-5}$ <i>rad</i>

Table 5.1: Mechanical characteristics of the best candidates materials for accelerometers.

### 5.3.3 Elliptical hinges

The most critical part of the folded pendulum are the flex joints supporting the test mass and performing the mechanical work of the system. The upgrade, with respect to the model presently used to perform inertial control in our laboratory, consists in a new geometrical design of the hinges: the previous version in fact has a circular form, while the present form is elliptical.

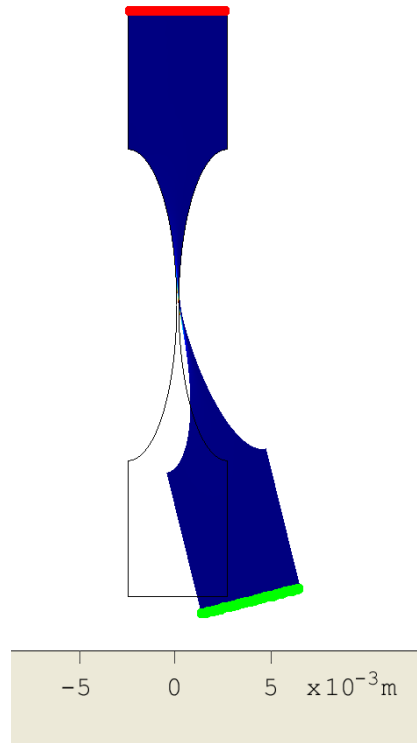


Figure 5.10: Example of the deformation of the hinge with a  $370 \mu\text{m}$  horizontal displacement. The deformation with respect the equilibrium position is enlarged by a factor 10 [38].

As we have seen, the eigenfrequency of the folded pendulum depends both on the gravity and on the elastic restoring force of the hinges. For this reason, to evaluate the frequency response contribution of the hinge ellipticity it is necessary to simulate (numerically) the first eigenfrequency (resonance frequency) of one folded pendulum hinge.

Using a finite elements method (FEM) simulation it has been possible to verify that the higher is the ellipticity the lower is the frequency of the hinge [38].

Those simulations have been performed without evaluate quantitatively the contribution of the elastic force to the global eigenfrequency of the folded pendulum. The evaluation was focused on the single hinge response only, in order to have a qualitative contribution of the ellipticity on the natural frequency. For these reason the absolute value of the frequency is not important for our goal, but it is of interest only the variation of the frequency relatively

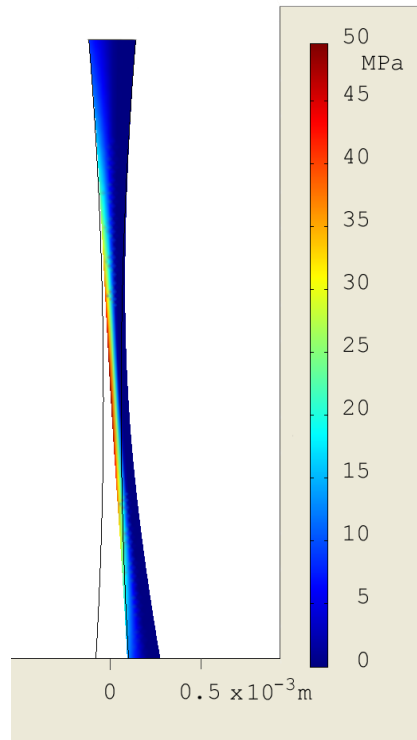


Figure 5.11: Completely elastic deformation, with stress value always below the elastic limit of the material (hinge with ellipticity  $\epsilon = 3.2$ ) [38].

to the variation of the ellipticity.

To this purpose numerical simulation (without considering gravity contribution) has been used [38].

An example of hinge shape is drawn in figure (5.10). In this simulation, as boundary condition, it was chosen the upper face as fixed (horizontal red line in the figure). Observing the figure relative to the deformation stress (5.11), it is possible to see that the material stress (on the right of the hinge, in blue color) is very low, by contrast to the right part of the hinge (red color) that has the maximum of the deformation. However this is only the maximum stress of the external part (only the surface) of the hinge: in fact the central part of the hinge has always a stress whose value is under  $550 \text{ MPa}$ , the limit of the elastic stress, so the hinge is always in the elastic deformation range.

In order to design the shape of the hinge it is of primary importance to analytically study the hinge stress during the accelerometer work, and the angular stiffness contribution.

The behavior of the angular stiffness is described by the Tseytlin formula

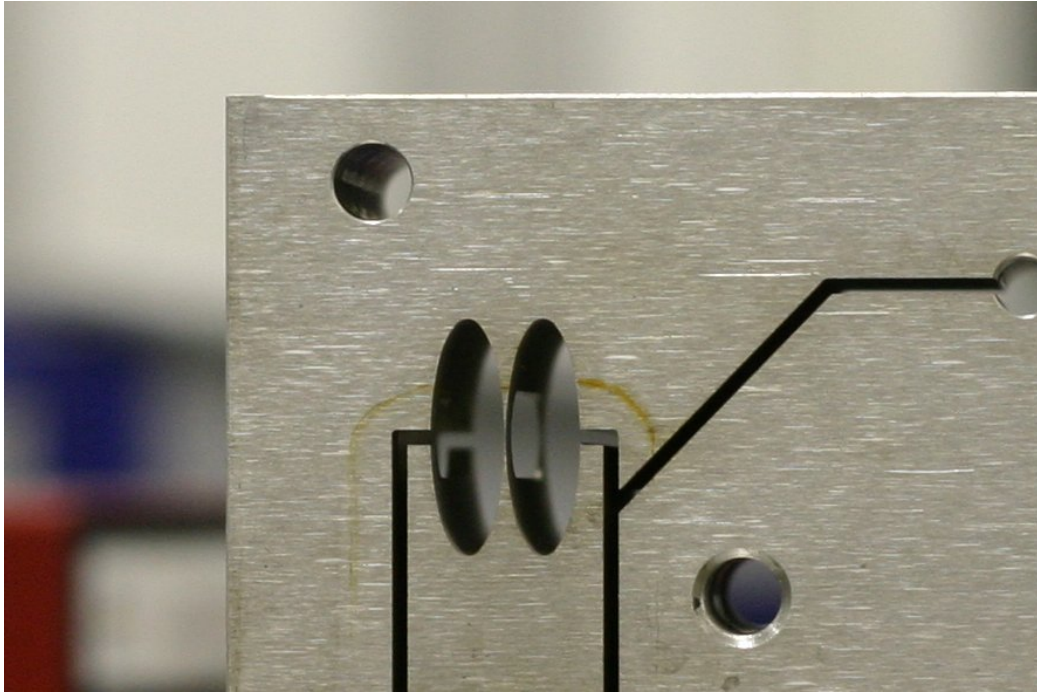


Figure 5.12: Example of elliptical hinge.

[40]:

$$k = \frac{Eat^2}{16[1 + \sqrt{1 + 0.215(2\epsilon R/t)}]} \quad (5.33)$$

where  $a$  is the width of the joint,  $t$  is the thickness at the center,  $R$  is the radius of curvature,  $E$  is the Young's modulus of the material and  $\epsilon$  is the hinge ellipticity.

The accelerometers presently used are characterized by circular notch hinges ( $\epsilon = 1$ ) but an elliptical hinge (with the minor axis equal to the ratio of the circular hinge) can give to the system a lower stiffness. In fact, in this case, the part of the material under stress is larger respect to the circular hinge case. This means that the stress is sharing on a larger surface.

A calculation of the suitable ellipticity values has been performed using simulation program based on the finite element analysis [38]. It has been possible to characterize the stress and to evaluate if the deformation was below the elastic limit of the material.

For instance, taking fixed the minor axis ( $2.5 \text{ mm}$ ) and varying the major axis, in order to have different ellipticity it was possible to simulate the response of each type of hinge. In figure (5.14) it is shown some of the elliptical hinges used; let's note that when the major axis has the value of

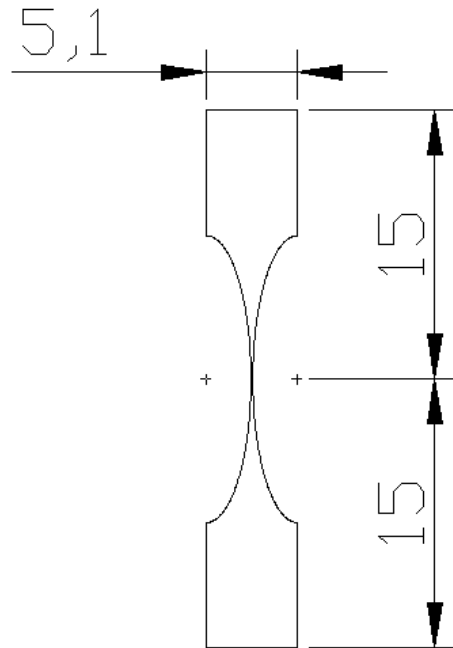


Figure 5.13: Example of simulated hinge with the finite element method; the quote values are in millimeters.

2.5 mm (with  $\epsilon = 1$ ) the hinge is circular, with the dimension of the radius equal to 2.5 mm.

Analyzing with finite elements method the characteristic of elliptical hinge, using the COMSOL<sup>®</sup> [39] simulation application, it was possible to obtain the curves shown in figure (5.15). In this figure we see that the natural frequency of an hinge decrease to the increasing of the hinge ellipticity, as it is also clear from equation (5.33).

In the figure (5.15) it is also shown the material stress. The boundary condition, used to calculate the stress, consists into fixing the upper face of the structure (red line in the upper part of figure (5.10) and moving to a predefined distance the lower face green line in the lower part of figure (5.10)). In this way it is possible to measure the stress of the material in stress condition and load similar to those existing in a real accelerometer hinge. The stress taken into consideration was the bending stress, due to the deformation of the hinge when the suspended mass moves from an equilibrium position to an extreme position. The load has been chosen by dividing the total suspended mass by eight (there are 8 flex joint constituting the accelerometer) and as value for the load a force of 1 N was chosen (the weight of the oscillating

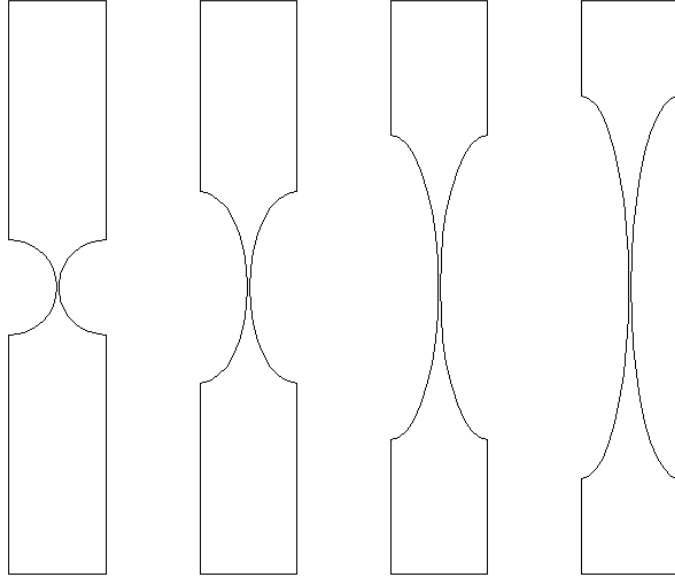


Figure 5.14: Examples of joint shapes with ellipticity  $\epsilon = 1$  ,  $\epsilon = 2$  ,  $\epsilon = 3.2$  and  $\epsilon = 4$ , from left to right.

parts is about  $800\text{ g}$ ).

In the figure (5.15) we can see that the first principal stress of the hinge, with ellipticity varying in the interval  $\epsilon \in [1, 4]$ , is always below the limit of the elastic limit of  $550\text{ MPa}$  of the material when the hinge has the maximum deformation (corresponding to an extreme position of the test mass), that is a guarantee of robustness and long-term durability of the mechanics. The figure (5.11) shows the distribution of the first principal stress for the hinge corresponding to  $\epsilon = 3.2$  demonstrating that the stress quenches with the ellipticity.

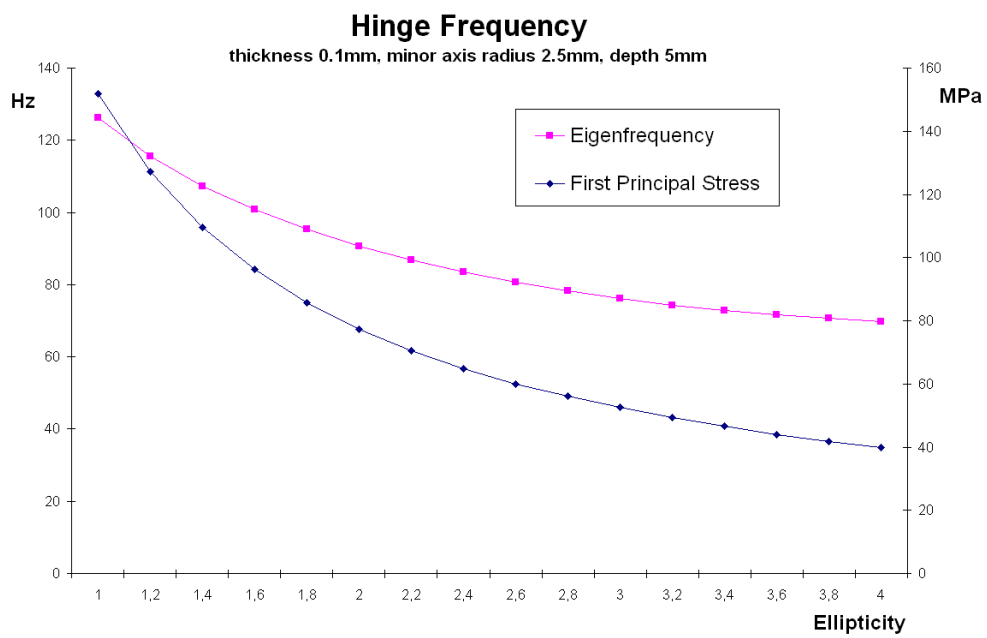


Figure 5.15: Eigenfrequencies and the first principal stress of the hinge versus hinge ellipticity  $\epsilon$ .

# Chapter 6

## Accelerometer performances

In the previous chapter we have seen the characteristics offered by the folded pendulum structure and the possible improvements with respect the accelerometer model presently used to perform inertial damping in our laboratory. Taking into account those characteristics several prototypes of such accelerometers have been realized. In particular, in this chapter it will be shown the characteristics and the test measurements of the most performing model among the implemented prototypes.

This model has been fabricated in the INFN *Officina Meccanica* of Napoli. Our sensor was obtained starting from a  $140 \times 134 \times 40 \text{ mm}$  block of metal (Alloy 7075-T6) shaped with precision machining and electric discharge machining. The four torsional flexures, connecting the pendulum arms to the central mass and to the frame, have an elliptical profile with  $100 \mu\text{m}$  minimum thickness with ellipticity ratio of  $\epsilon = 16/5$ . The pendula arms ( $71.5 \text{ mm}$  length and spaced by  $102 \text{ mm}$ ) are designed to minimize the mass and the moment of inertia without reducing rigidity and symmetry.

With respect to the model developed in the previous chapter, the value of the simple pendulum mass is  $m_{a_1} \approx 40 \text{ g}$ , the inverted pendulum has mass  $m_{a_2} \approx 50 \text{ g}$  and the central mass has mass  $(m_{p_1} + m_{p_2}) \approx 600 \text{ g}$ .

### 6.1 Optical readout

One of the main requirement in the readout system is that it has to be a non-contacting system. For this purpose, in our system, the choice has been an optical readout. As it will be shown, this solution guarantees a very high sensitivity and very low coupling effects with environmental noises. The optical scheme is shown in figure (6.1).

From this figure it is easy to see that the optical readout system is basi-

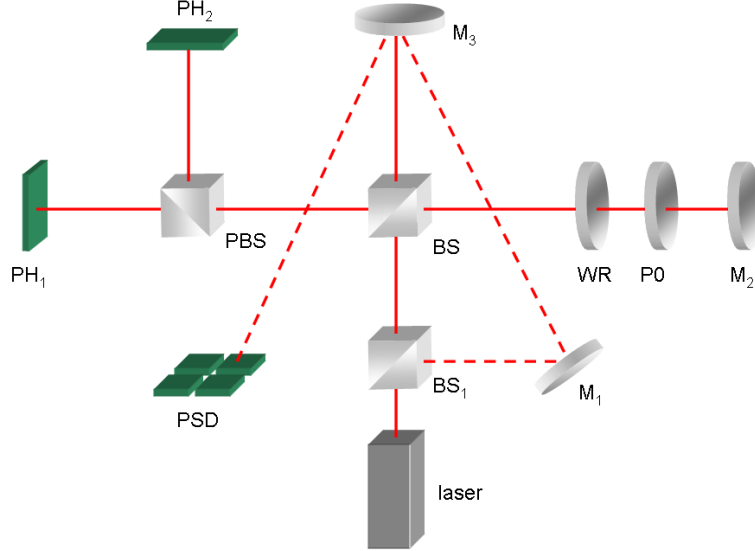


Figure 6.1: Optical scheme of the implemented readout system.

cally a combination of an optical lever and a classic Michelson interferometer.

The optical readout works in a very simple way. A stabilized laser beam ( $\lambda = 632.8nm$ ,  $P = 3mW$ ) is divided into two beams by means of the beam splitter  $BS_1$ . A first beam (dotted line in figure 6.1), reflected by the mirror  $M_1$  is used for the implementation of an optical lever. The beam is reflected by the mirror  $M_3$  which is mechanically connected to the test mass. Then the mass position is detected by means of a PSD photodiode (Hamamatsu S2044). The signals, coming from the PSD, are combined and amplified using an ad hoc developed electronic board. Therefore, the optical lever provides a signal, that after some elaboration, is proportional to the relative motion of the test mass with respect to the sensor frame.

A second beam (continuous line in figure 6.1) is used for the implementation of a polarimetric homodyne Michelson interferometer [41]. This system consists in a beam splitter  $BS$ , a  $\lambda/4$  retarder ( $WR$ ), a polarizing plate  $P0$ , a reference mirror  $M_2$  and again mirror  $M_3$  connected to the mass. The interference beam is split using a polarized beam splitter ( $PBS$ ). Then the polarized beam is detected by the photodiodes  $PH_1$  and  $PH_2$  always differing each other of  $1/4$  of a fringe (or  $\pi/2$ ). Therefore, the mirror displacement is reconstructed with a quadrature correction algorithm and a phase-unwrapping technique [42].

Of course, when the sensor is used in feedback force configuration, an

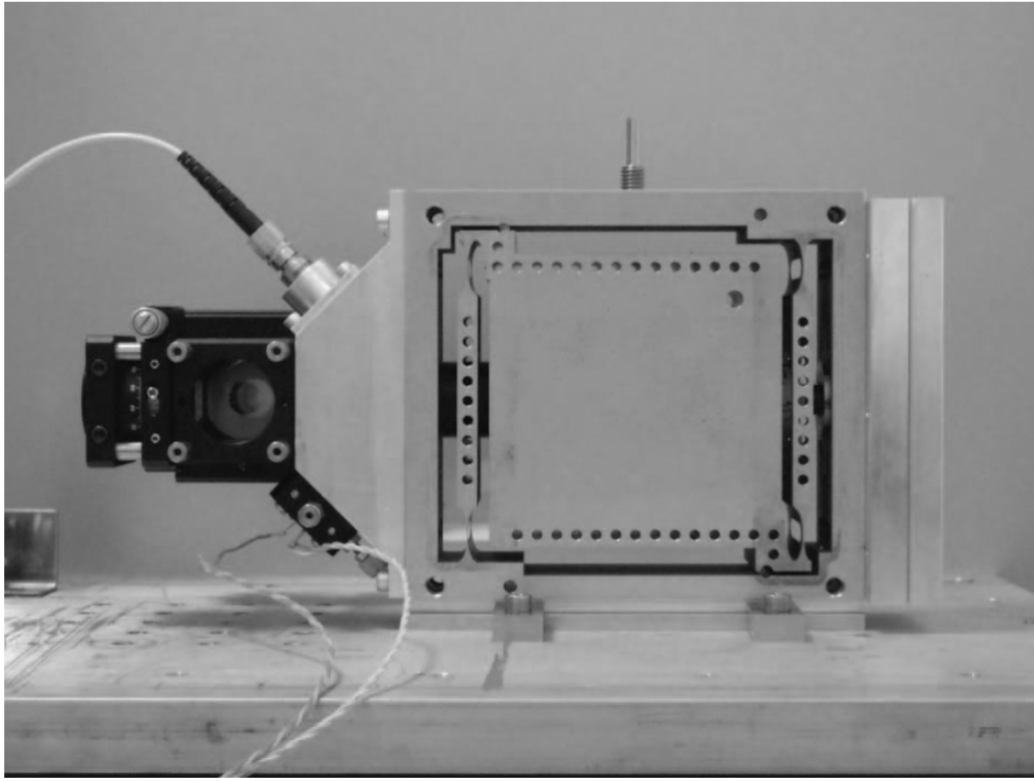


Figure 6.2: Horizontal monolithic folded pendulum sensor. On the sensor left side there is the inverted pendulum and the mirror, connected to the moving central mass, and the optical read-out. On the sensor right side there is the simple pendulum and the coil-magnet actuator for the implementation of the FP control when the sensor is used as an accelerometer. The calibration masses can be placed on the central mass.

actuator it is necessary. In our case the actuation is provided by means of a magnet-coil actuator mounted on the simple pendulum side which appears on the right in figure (6.2).

Instead, the optical readout system has been implemented in a very compact way and it is placed on the inverted pendulum side appears on the left in figure (6.2).

## 6.2 Preliminary measurements

Preliminary tests have been performed on the monolithic FP mechanics, in order to demonstrate both the reliability of the theoretical model and the effectiveness of the monolithic FP natural frequency reduction with a suitable

tuning procedure.

The reliability of the theoretical model was proved by comparing the experimental monolithic FP transfer function to the theoretical one, described by the equation (5.32). For this task the central mass,  $m_p$ , was excited with white noise (input signal) through the coil-magnet actuator (see Figure 6.2) while the output signal, that quantifies the central mass motion, was detected by means of the optical lever readout. An example of results of this first tests is shown in figure (6.3), where both the theoretical model and the experimental points are reported. In this example (as in the other measurement not showed for practical reason) it is evident a very good agreement between model and data. The analysis of these example of data shows a natural resonance frequency of the monolithic FP  $f_0 = 720 \pm 5 \text{ mHz}$  with a  $Q \approx 140$  in air. It is important to notice that the quality factor  $Q$  has a remarkable low value with respect the results obtained with no voice-coil actuator, due to the presence of the wire from the voice-coil to the frame that degrade the performance of the system.

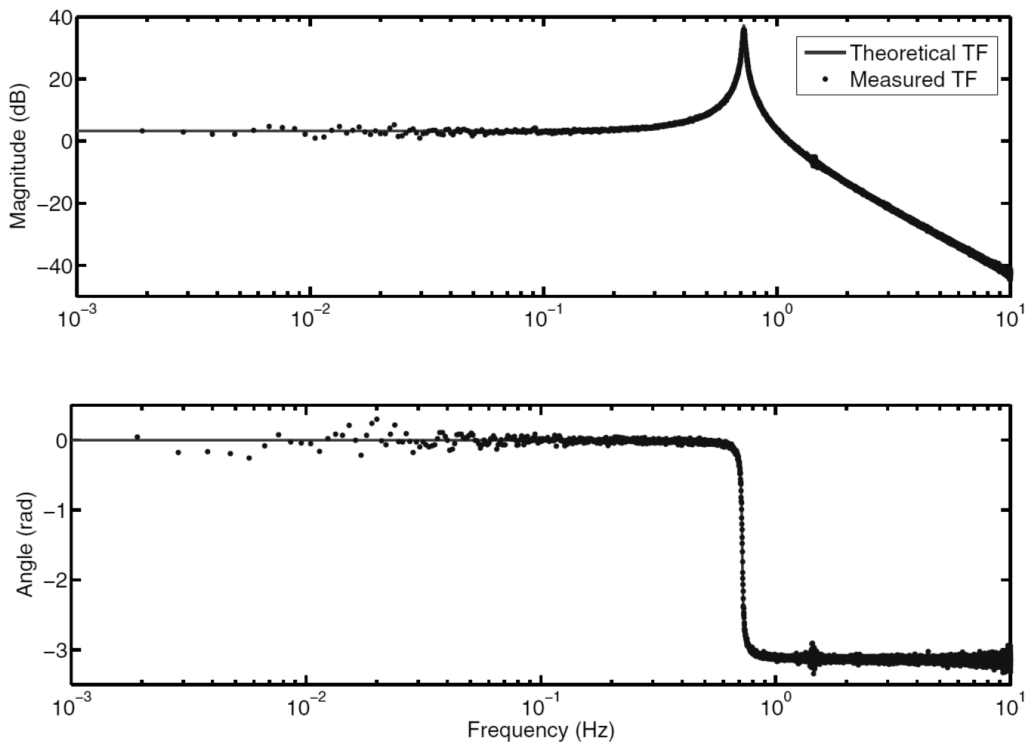


Figure 6.3: Theoretical and experimental transfer function of the horizontal monolithic FP.

To test the tuning procedure, we used tuning masses of different weights, in order to implement a rough or fine calibration. Those tuning masses are positioned in the opening of the test mass. The tuning masses were moved in small steps, of less than  $1\text{ mm}$ .

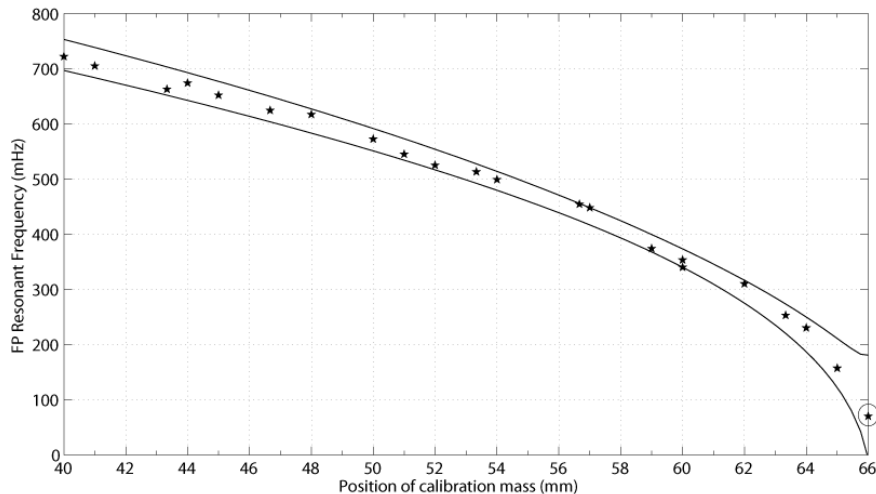


Figure 6.4: Measured resonance frequencies of the horizontal monolithic folded pendulum sensor. The best measured frequency,  $f_r = 70\text{ mHz}$ , is circled.

Different sets of measurement have been performed. In figure (6.4) an example of measured frequency versus the tuning mass position is shown. The data were fitted using the equation (5.27). The figure (6.4) shows very good agreement between the experimental data and the  $3\sigma$  error bars of the theoretical model (area between the continuous lines).

The lowest natural frequency measured is about  $70\text{ mHz}$  with a  $Q < 10$ , which is a very good result for a monolithic FP sensor of these size. It is worth to notice that the position of the calibration mass has been fixed with an accuracy of about  $\pm 1\text{ mm}$ .

As said before, tuning the folded pendulum at its lowest possible natural frequency maximizes the sensor measurement band at low frequencies, but at the same time it reduces the restoring force of the pendulum to external perturbations, so that the test mass easily touches the frame, saturating the sensor.

This could be a problem because of the short dynamical range provided for the FP especially in seismometer configuration. But we have seen that this problem can be partially solved enlarging the gaps among the central

mass-arms and arms-frame. In any case, it would be not a problem for the FP in accelerometer configuration, being the central mass kept in its rest position by means of a force feed-back control. The real drawback of the FP structure is related to the fact the its quality factor  $Q$  decreases together with its natural frequency. This means a performance degradation of the monolithic FP sensor at low frequency. An investigation of the mechanical quality factor dependence by environmental parameters (in particular, the air pressure) will be described in a next specific section.

## 6.3 Sensitivity curve

There are several noise sources affecting the sensitivity of the FP sensor: thermal noise, readout noise and electronic noise. The internal thermal noise is dependent on the material and on the mechanical design, while the readout noise and electronic noise are instead related to the external devices used to acquire the output signal.

In the following we will describe each noise source and its contribution on the total sensitivity curve.

### 6.3.1 Thermal noise

In order to calculate the internal thermal noise of FP it is possible to make use of the *Fluctuation Dissipation Theorem* [3] according to which, if we consider a system under a random force  $F_{th}$  with a white spectral density, the system transfer function  $H(\omega)$  is strictly connected with the power spectrum:

$$x_{therm}^2(\omega) = \frac{4K_B T}{\omega} \Im[H(\omega)] \quad (6.1)$$

where  $K_B$  is the Boltzmann constant,  $T$  is the absolute temperature. In the model described in section (5.2) we have considered our folded pendulum as a spring-mass oscillator with an equivalent elastic constant  $K = K_g + K_e$  and equivalent mass  $M_e$  described by the equation (5.30).

Assuming that the energy dissipation of the folded pendulum is localized in the flex-joint and that the origin of the loss is intrinsically related to the material, it is possible to introduce an imaginary part (the *loss angle*  $\phi$ ) of the elastic constant  $K_e$  [43] obtaining a new constant  $K'$ .

$$K' = K_g + K_e(1 + i\phi) = K + K_e i\phi = K\left(1 + i\phi \frac{K_e}{K}\right) = K(1 + i\phi_{eff}) \quad (6.2)$$

In this way it is possible to define an equivalent loss angle  $\phi_{eff}$  of the effective spring constant as:

$$\phi_{eff} = \phi \frac{K_e}{K} \quad (6.3)$$

In order to calculate the thermal noise contribution, if the FP dynamics shows small hysteresis, it is possible to use the fluctuation dissipation theorem (which is true only for linear system). The detailed procedure is described in Appendix A.

The internal thermal noise of a folded pendulum is described by:

$$x_{int}^2(\omega) = \frac{4K_B T \phi_{eff}(\omega) \omega_0^2}{\omega M_e^2 [(\omega_0^2 - \omega^2)^2 + \omega_0^4 \phi_{eff}^4(\omega)]} \quad \left[ \frac{m^2}{Hz} \right] \quad (6.4)$$

Because of the air presence it is necessary to take into account an additional thermal noise contribution. The damping (air friction) will produce a viscous term described by:

$$x_{visc}^2(\omega) = \frac{4K_B T \beta}{M_e^2 (\omega_0^2 - \omega^2)^2 + \omega^2 \beta^2} \quad \left[ \frac{m^2}{Hz} \right] \quad (6.5)$$

where  $\beta$  take into account the medium viscosity.

### 6.3.2 Optical noise

This noise is related to the radiation pressure of the laser source and to the shot noise of the photodiodes.

#### Radiation pressure

The radiation pressure can be described by:

$$x_{rad}(f) = \sqrt{\frac{h P_0}{8\pi^3 c \lambda M_e f^2}} \quad (6.6)$$

where  $h$  is the Planck constant,  $P_0$  is the power of the laser source,  $c$  is the velocity of light,  $\lambda$  is the laser wavelength). Because of the low power of the laser sources ( $P_0 < 10 \text{ mW}$ ) the radiation pressure contribution is negligible in our case.

About the optical readout noise it is necessary to distinguish between the PSD photodiodes (used for optical lever) contribution and the shot noise of the photodiodes used in the Michelson interferometer readout.

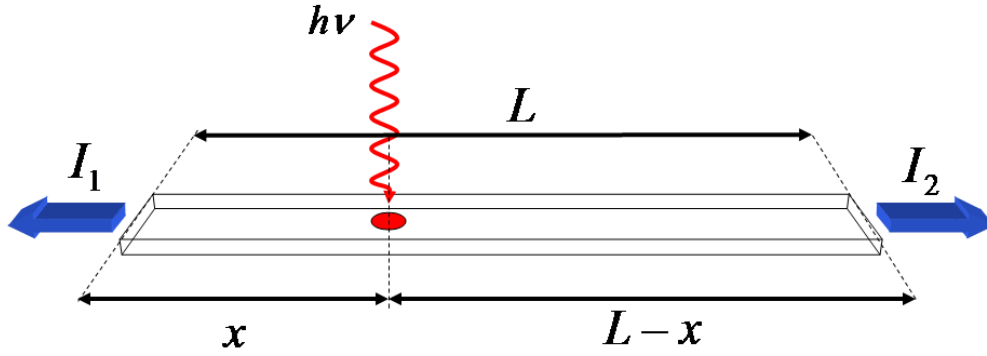


Figure 6.5: Schematic of position sensing device: the circle represent the area of the laser beam at a  $x$  distance from one end.

### Position sensing devices

Let consider the figure (6.5) in which it is shown the schematic of a PSD of length  $L$  on which there is a circular laser beam spot at distance  $x$  from one extreme.

The response of the PSD is given by

$$x = K \frac{I_1 - I_2}{I_1 + I_2}$$

where  $I_1$  and  $I_2$  are the current generated at the two end of resistive substratum of the sensor:

$$I_1 = \frac{e\eta P_0}{h\nu} \frac{x}{L}$$

and

$$I_2 = \frac{e\eta P_0}{h\nu} \frac{L - x}{L}$$

where  $\eta$  is the quantum efficiency  $h$  is the Planck constant and  $P_0$  and  $\nu$  are the laser source power and its emitting frequency respectively.

When the optical beam is smaller than the width of the PDS, the current delivery is:

$$I(x) = \frac{e\eta P_0}{h\nu} \frac{L - 2x}{L} \quad (6.7)$$

The slope of the signal, that has a linear trend along the beam displacement, is:

$$\frac{dI(x)}{dx} = \frac{2}{L} \frac{e\eta P_0}{h\nu}$$

so the minimum detectable displacement will be:

$$\Delta x_{Pmin} = \sqrt{\frac{2h\nu}{\eta P_0}} \frac{L}{2} \quad (6.8)$$

Then expressing the (6.8) in terms of wavelength  $\lambda$  (using  $\lambda\nu = c$ ) we can conclude that the minimum detectable displacement due to the PSD shot noise is

$$x_{sh}(\lambda) = \frac{L}{2} \sqrt{\frac{2hc}{\eta\lambda P_0}} \left[ \frac{m}{\sqrt{Hz}} \right] \quad (6.9)$$

### Interferometric readout

The shot noise for an usual photodiode, employed in the case of interferometric readout, is

$$x_{sh}(f) = \sqrt{\frac{hc}{8\pi^2 P_0 \eta \lambda}} \left[ \frac{m}{\sqrt{Hz}} \right] \quad (6.10)$$

### 6.3.3 Electronic noise

The Voltage-Current amplifiers used have been designed to minimize the electronic noise. The principal noise sources we have considered are the Johnson noise of the resistors, the shot noise and the  $1/f$  noise. Concerning the analog-to-digital converter (ADC) noise, it was used a real 18 bit ADC with a sampling frequency  $F_s = 1 \text{ kHz}$  and range of  $\pm 10 \text{ V}$ . We modeled the ADC noise as a white noise with equivalent displacement spectral density

$$x_{ADC}(f) = \mathcal{C} \frac{20}{2^{18} \sqrt{F_s}} \left[ \frac{m}{\sqrt{Hz}} \right] \quad (6.11)$$

where  $\mathcal{C}$  is a calibration constant related to the conversion voltage to displacement.

## 6.4 Measurements at atmospheric pressure

There are two possible configurations for the monolithic FP sensor, as seismometer or accelerometer. In both of the cases the mechanics and the optical readout are the same. For both of the configurations the tests were made with the same Real Time Control and Data Acquisition System (DAQ). It is composed by a cluster of two PCs: the first one is a desktop PC used as real time machine, running Labview<sup>©</sup> with Real Time Module operation system, and equipped with a 18 bits DAQ board by National Instrument<sup>©</sup>, model PXI-6289; the second one is an Host PC, running Windows 7<sup>©</sup> operating system and LabView 8.6 as real time software development platform. The sampling frequency was set to 2kHz. All the tests were made in air without thermal stabilization. The effects of thermal air stabilization have an important role, but, at this stage of development are less relevant.

### 6.4.1 Monolithic FP sensor as *seismometer*

The configuration of the monolithic FP as seismometer is straightforward. In fact, as shown before, the readout output signal ( $x_p(\omega) - x_s(\omega)$ ) is acquired, calibrated and then processed according to the equation (5.25). According to the readout configuration of the monolithic FP seismometer we measured the three sensitivity curves corresponding to optical levers and interferometer readouts. In figure (6.6) a central mass displacement as recorded by interferometric readout is shown.

We remind here that all the tests were performed in air and with no thermal stabilization. In figure (6.7) the best theoretical and experimental sensitivities curves at ( $T = 300 K$ ) and ( $f_0 = 70 mHz$ ) are shown.

To compare the sensitivity of the FP seismometer with other geophysical instruments, we reported in figure (6.7) also the sensitivity of the STS-2 by Streckeisen, that represents the state-of-art of the low frequency seismic sensors [44]. This Figure shows that the monolithic FP sensor has already a sensitivity comparable or better (with interferometric readout) than the STS-2 in the band  $10^{-3} \div 10 Hz$ . We reported also the Peterson New Low Noise Model (NLNM) [46], that is the Minimum Earth Noise. From a collection of seismic data from 75 sites located around the world, Peterson found that there is a minimum level of earth noise; noise levels below this are never or extremely rarely observed.

As a comparison in figure (6.8) it is shown the displacement noise of the model presently used in our laboratory [45].

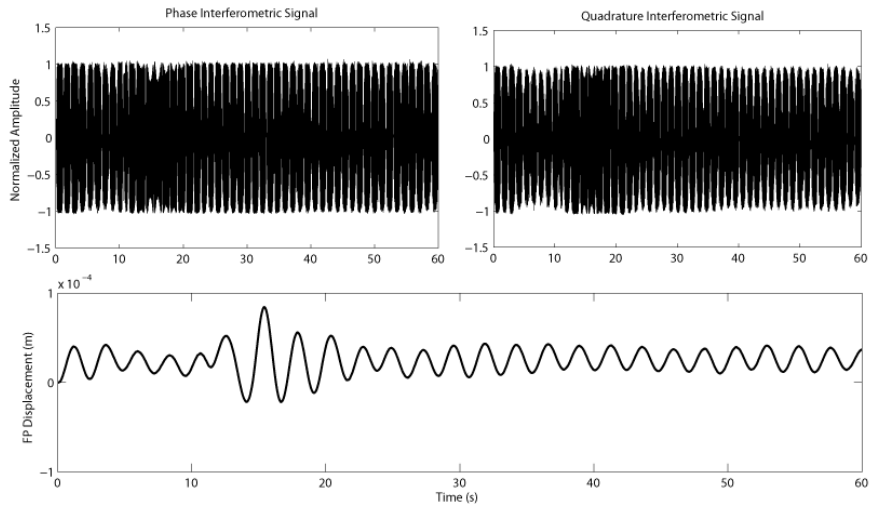


Figure 6.6: On the top an example of interferometric readout output is shown, while, on the bottom, the reconstruction of central mass displacement of several fringes is shown [47].

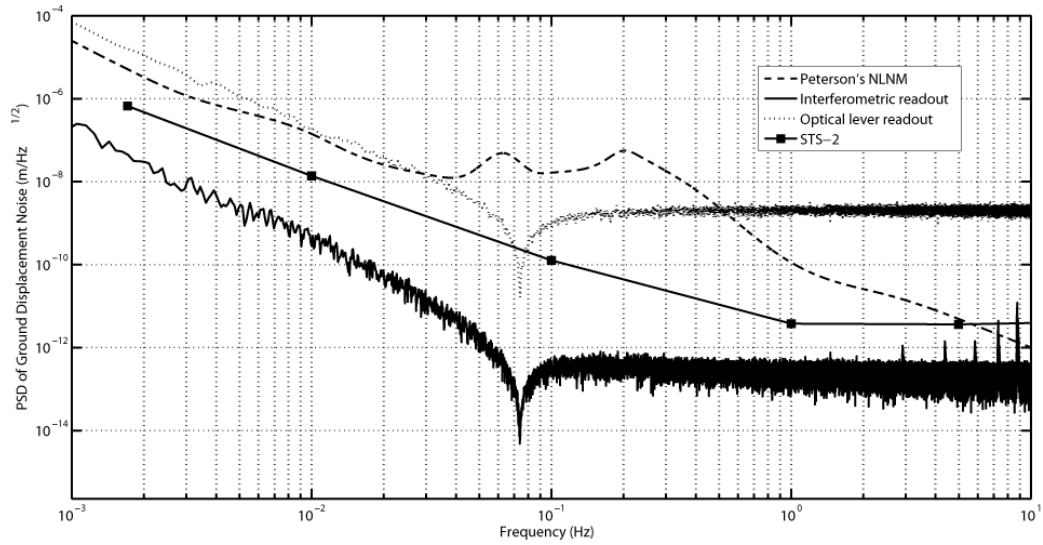


Figure 6.7: Theoretical and experimental sensitivity curves of the monolithic FP seismometer with optical lever and laser interferometric readouts. Note that the theoretical curves were evaluated at  $T = 300\text{ K}$ , while the best experimental sensitivities were evaluated for a seismometer with the best obtained natural frequency ( $f_0 = 70\text{ mHz}$ ) [47].

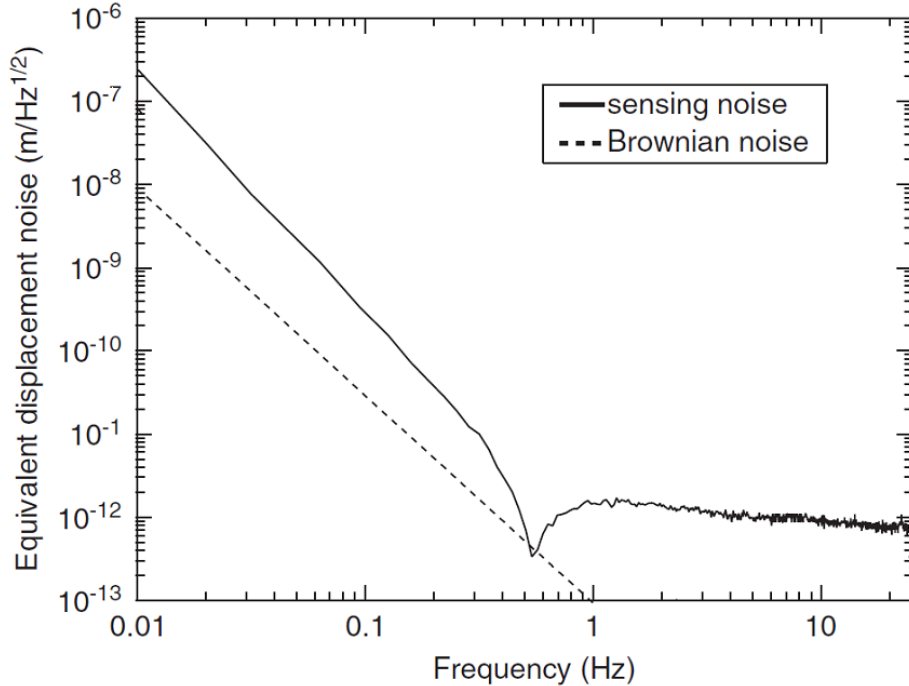


Figure 6.8: Equivalent inertial displacement noise of the aluminum FP accelerometers presently used in our laboratory. The readout noise is compared with the thermal (Brownian) noise level for a mechanical quality factor of 3000 [45].

#### 6.4.2 Monolithic FP sensor as *accelerometer*

The use of the monolithic FP sensor as accelerometer is less direct. In fact the system must be provided with a suitable feed-back system. The output signal of the optical readout, this time properly digitally filtered according to the rules of the control theory, drives the coaxial linear voice-coil actuator located opposite the optical readout (as shown in Figure 6.2). The force actuator keeps dynamically the proof mass at the equilibrium position, corresponding to the zero point of the PSD or to the dark fringe of the Michelson interferometer. As already mentioned in this configuration the correction signal driving the voice-coil actuator is proportional (through a calibration factor) to the ground acceleration. This configuration is known as force feed-back configuration.

The control scheme implemented is shown in figure (6.9) where  $a(s)$  is the reference signal (ground acceleration),  $FP(s)$  is the folded pendulum transfer

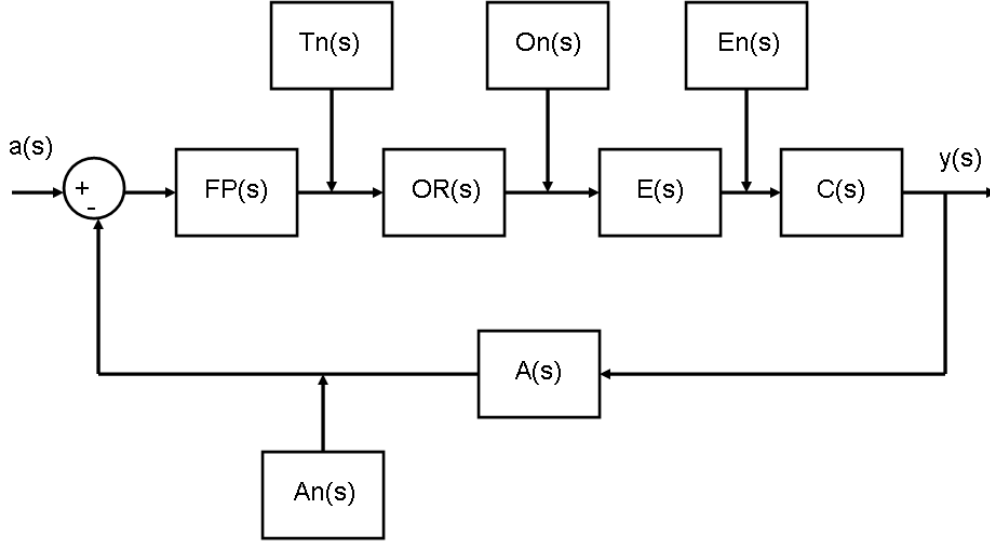


Figure 6.9: Control scheme of the accelerometer

function  $(x_p - x_g)/a_g$ ,  $OR(s)$  is the optical readout transfer function,  $E(s)$  is the conditional electronic transfer function,  $C(s)$  is the controller,  $A(s)$  is the actuator transfer function,  $Tn(s)$  is the thermal noise of the folded pendulum,  $On(s)$  is the shot noise of optical readout,  $En(s)$  is the electronic noise,  $An(s)$  is the actuator noise,  $y(s)$  is the output of control system. The transfer function is:

$$\frac{y(s)}{a(s)} = \frac{FP(s)OR(s)E(s)C(s)}{1 + FP(s)OR(s)E(s)C(s)A(s)} \quad (6.12)$$

in the hypothesis that  $A(s) = 1$  and  $FP(s) OR(s) E(s) C(s) \gg 1$  (closed loop transfer function  $> 10 dB$ ) then  $y(s) \approx a(s)$  and the control signal is proportional to the ground acceleration. To realize the closed loop configuration we used a control filter based on PID controller with a double pole low pass filter to reduce the high frequency noise. In figure (6.10) the open loop and the closed loop bode diagram are shown. As it can be seen the control bandwidth is about  $70 Hz$  and the ripple in pass bandwidth is less than  $3 dB$ .

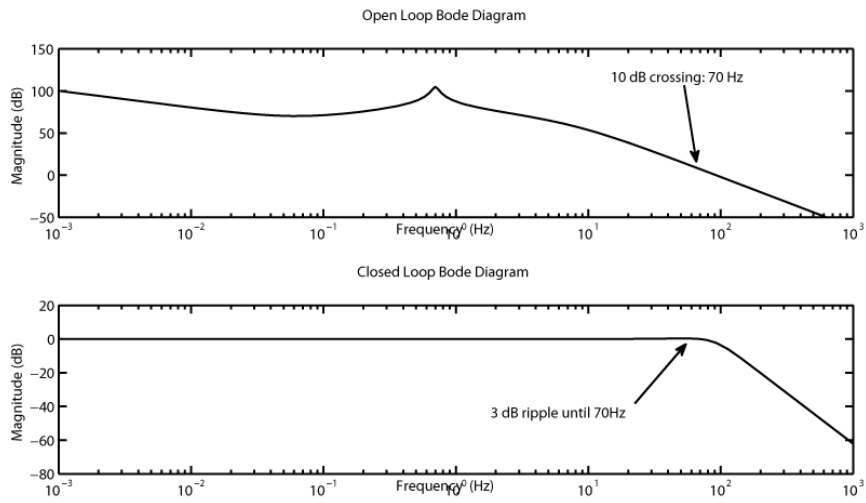


Figure 6.10: The open loop (top) and the closed loop (bottom) Bode diagram of the FP sensor used as an accelerometer.

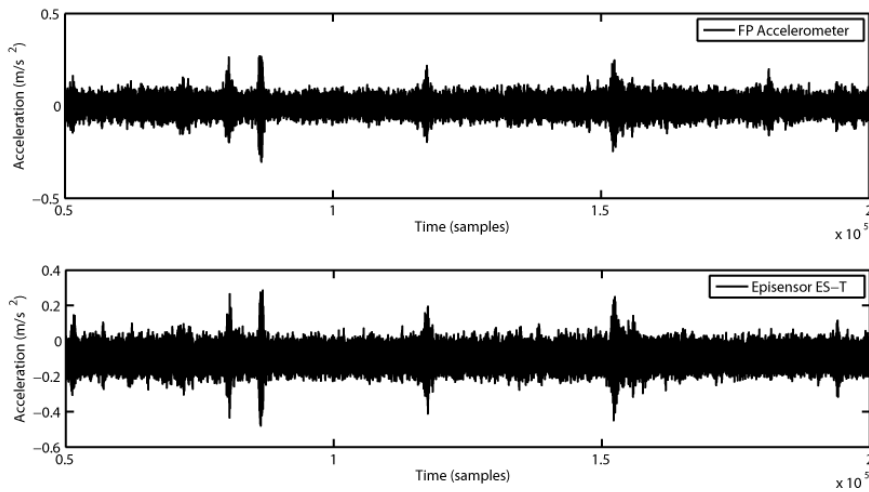


Figure 6.11: An example of signals as recorded by a commercial accelerometer (up) compared to FP accelerometer (down) [47].

To test the response of FP accelerometer with respect to the ground vibration, a seismic station was installed in our laboratory. An example of signals as recorded by FP accelerometer respect to a commercial accelerom-

eter (Episensor model ES-T by Kinematics<sup>©</sup>) is shown in figure (6.11).

## 6.5 Measurements in vacuum

Measurements performed at atmospheric pressure are not able to show intrinsic mechanical properties of the joints. In order to investigate the mechanical behavior of our folded pendulum detectors, a vacuum chamber able to host two FP seismometers, including the optical read-out system, has been prepared and equipped.

### 6.5.1 Internal quality factor in a folded pendulum

In section (5.2) a folded pendulum has been described as an oscillator with natural pulsation:

$$\omega_0 = \sqrt{\frac{K}{M_e}} \quad (6.13)$$

where the equivalent elastic constant  $K = K_g + K_e$  take into account a *gravitational* and an *elastic* contribution.

As previously done, let consider the equivalent constant  $K'$  described by the equation (6.2) and the equivalent loss angle of the effective spring constant  $\phi_{eff} = \phi \frac{K_e}{K}$ . We can express explicitly the dependence of  $\phi_{eff}$  from the resonant frequency using the expression of  $K$  from the equation (6.13):

$$\phi_{eff} = \phi \frac{K_e}{M_e \omega_0^2} \quad (6.14)$$

Then, we can write that the internal  $Q_{int}$  factor has the expression:

$$Q_{int} = \frac{1}{\phi} \frac{M_e}{K_e} \omega_0^2 \quad (6.15)$$

### 6.5.2 Folded pendulum and internal and external damping in coexistence

At this point, we have to consider a more realistic case of a folded pendulum in which we take into account the presence of the air also. A viscous medium affects the FP performances by degrading the quality factor.

The simultaneous presence of the both damping sources (internal and viscous) can be described using the quality factor expression for internal and

viscous damping (a more exhaustive derivation of this terms can be found in Appendix A):

$$Q_{int} = \frac{1}{\phi} \frac{M_e}{K_e} \omega_0^2 \quad (6.16)$$

and

$$Q_{visc} = \frac{M_e \omega_0}{\beta} \quad (6.17)$$

Then, the total quality factor  $Q_{tot}$  will be:

$$Q_{tot} = \frac{Q_{int} Q_{visc}}{Q_{int} + Q_{visc}} = \frac{M_e \omega_0^2}{\phi K_e + \beta \omega_0} \quad (6.18)$$

Or equivalently, in terms of resonance frequency  $f_0 = \frac{\omega_0}{2\pi}$ :

$$Q_{tot} = \frac{4\pi^2 M_e f_0^2}{\phi K_e + 2\pi\beta f_0} \quad (6.19)$$

Summarizing, this means that, the quality factor  $Q_{visc}$  for viscous damping depends linearly on resonant pulsation, instead, the dependence of the quality factor  $Q_{int}$  for internal damping is quadratic. In the global case we have to take into account both of them and the total contribution is described by means of the (6.18) or (6.19).

### 6.5.3 Quality factor measurements

Characterization in vacuum conditions has been performed in order to consider structural dissipative effects only. Experimental results are shown in figure (6.12) where two regimes are evident. In the high pressure range, the medium viscosity is the dominant phenomenon and the mechanical quality factor is strongly affected by the presence of the air.

Considering low pressure values, the internal dissipation can carry out its role not any more masked by the medium viscosity. In this pressure range, differences among different natural frequencies of the FP are more evident leading to very high Q values.

Despite a folded pendulum with high quality factor is synonymous of high performing mechanical system, the figure (6.12) shows that such a characteristics can be obtained paying a cost. In fact, higher quality factors are obtained for higher resonance frequencies of the folded pendulum. This behavior qualitatively showed in figure (6.12) is quantitatively well described by our model in the equation (6.19). In fact, the same measurements are in

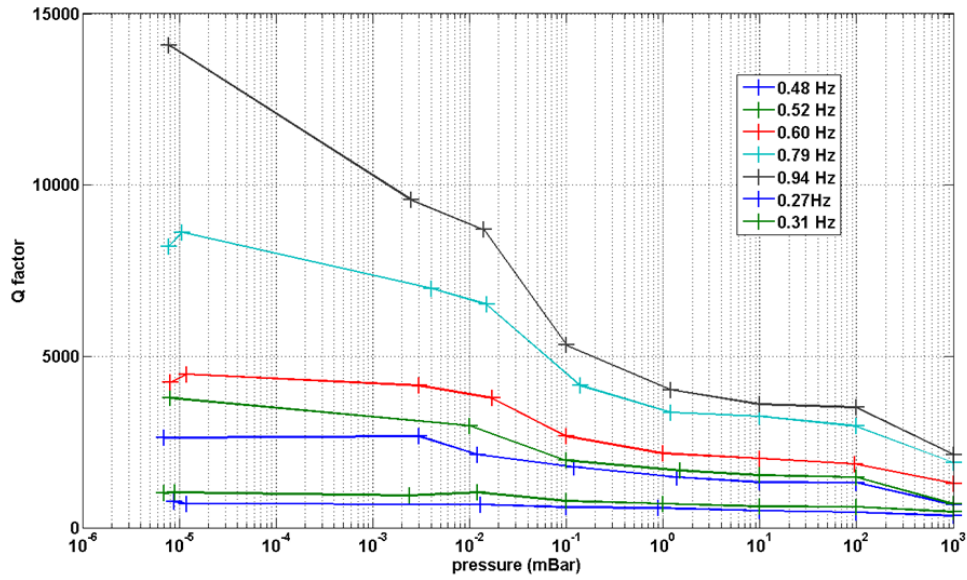


Figure 6.12: Mechanical quality factor versus pressure for different values of the natural frequency (obtained by changing the tuning mass position).

agreement with this model and the fits performed using the expression (6.19) are showed in figure (6.13).

In particular the viscosity coefficient  $\beta$  estimation is compatible with literature values whereas our estimation for the loss-angle is  $\phi = 6.35 \cdot 10^{-5} \pm 0.36 \cdot 10^{-5}$ .

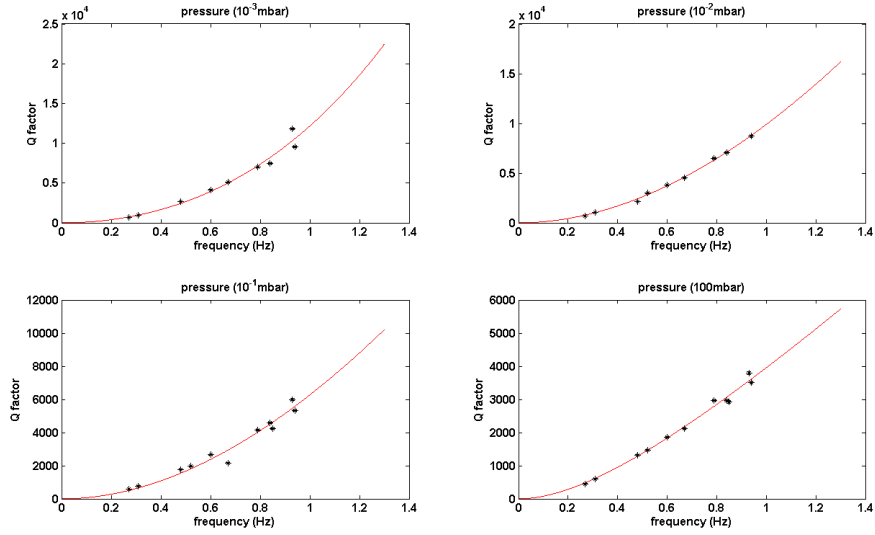


Figure 6.13: Examples of quality factor versus pressure measurements. The fits are performed using as fitting function  $Q_{tot} = \frac{4\pi^2 M_e f_0^2}{\phi K_e + 2\pi\beta f_0}$  where  $\phi$  is the aluminium loss angle and  $\beta$  the air viscosity.

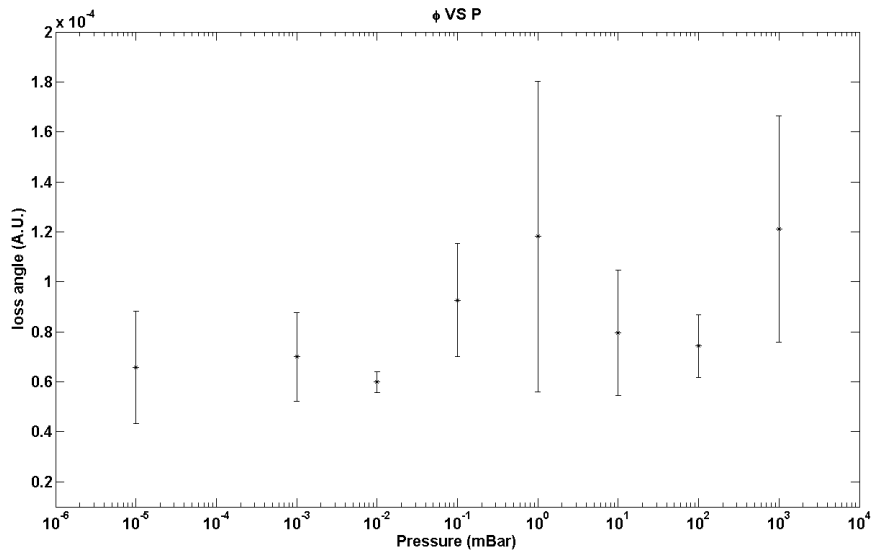


Figure 6.14: Aluminium alloy 7075 loss-angle  $\phi$  versus pressure measurements.

# Chapter 7

## Electrostatic actuators

The actuation system currently used in the VIRGO detector is composed by coil-magnet actuators. The same devices are used to control the inverted pendulum of our interferometer as described in subsection (2.7.2). In this chapter it will be shown the advantage of using an alternative system actuation with respect to coil-magnet system presently used. As it will be shown, their employment will be limited to the control of the interferometer last suspended stage because of the typical force order of magnitude they are able to apply on the test masses. The reason to develop an alternative actuation system is due to some disadvantages of using magnet-coil system actuation.

### 7.1 Magnet-coil actuation drawbacks

Magnet-coil actuators are presently used in VIRGO not only to control the seismic attenuation system elements (as described in chapter 2 for our interferometer) but also in the last stage to the final mirror control.

To this purpose, four permanent magnets are attached to the rear part of the mirror, at the same way, four coils are placed in the recoil masses in correspondence of the magnets. Through the application of the magnetic field created by the coils it is possible to control the mirror position on the various degrees of freedom. In particular, to lock the interferometer in the dark fringe in the VIRGO case, the order of magnitude of the force necessary is about  $10^{-3}N$ . As we will see, the actuation system we wish to propose is able to produce forces of this magnitude.

Despite the present employment, the magnet-coil actuation presents some negative aspects.

In particular, because of the peculiar way in which magnets are connected to the mass, there is an unavoidable mirror quality factor degradation. Also

when silicate bonding technique are used [48], an increasing of the mirror thermal noise is observed.

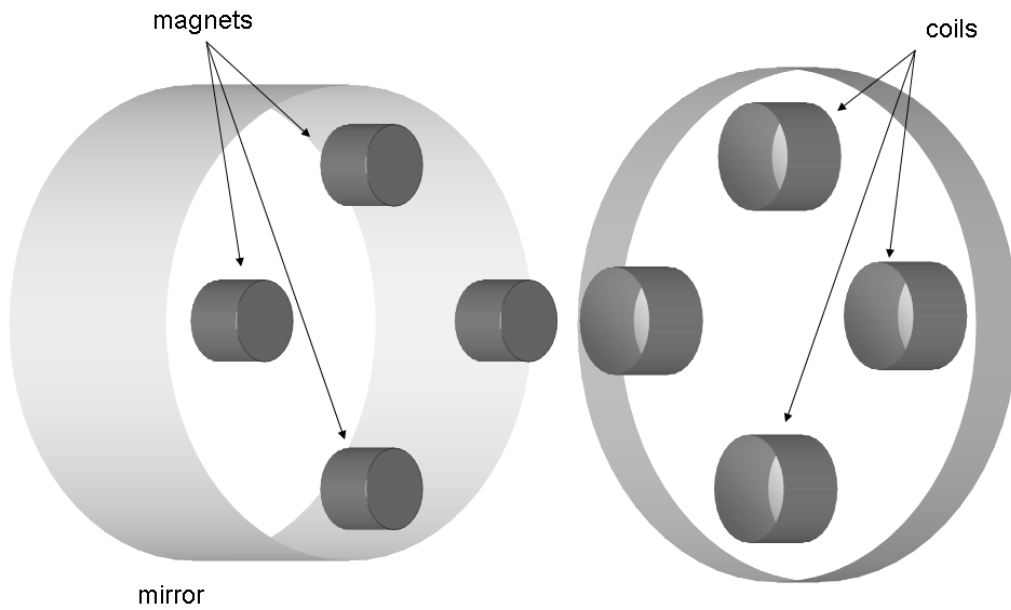


Figure 7.1: Magnets and coils on the rear side of the end mirror.

An additional problem is related to possible coupling with external magnetic field present in proximity of the test masses. The test masses are not magnetically screened as discussed in [49] and such a coupling could produce additional forces that could result in additional noise.

Another drawback related to the magnet-coil actuation is the difficulty in the fine control of the mirror position. This disadvantage is related to the Barkhausen effect [50].

It consists of a series of sudden changes in the size and orientation of ferromagnetic domains that occurs during the process of magnetization or demagnetization. This effect shows the direct evidence that the magnetization of a ferromagnetic substance by an increasing magnetic field takes place in discontinuous steps, rather than continuously.

The figure (7.2) shows a typical magnetization curve with  $B$ , the flux density, appearing to be a continuous function of the magnetic field  $H$ . Ex-

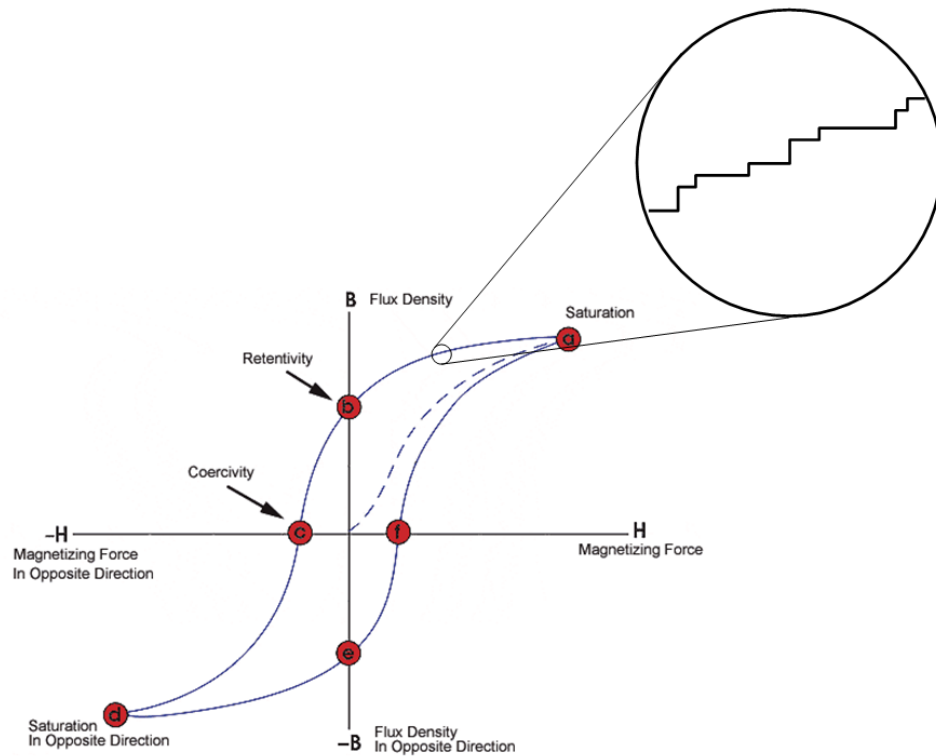


Figure 7.2: Barkhausen effect.

Examining the figure more closely, we find that the  $B - H$  curve consists of small, discontinuous changes of  $B$  as  $H$  varies.

These changes are the results of the Barkhausen effect, which has been studied in detail for various materials [51], and may cause a sort of noise in the force applied to the magnets limiting the precision in the fine control of the mirrors [52] [50].

## 7.2 Electrostatic actuation

In order to avoid the magnet-coil actuator disadvantages described in the previous chapter, an alternative actuation system could be employed.

Electrostatic actuators could be a valuable choice in order to substitute the present test mass actuation system.

EA are quite common as commercial devices especially in MEMS (Micro-Electro-Mechanical Systems) technology. As the commercial devices, our actuators are based on the electrostatic force generated by couples of electri-

cally charged electrodes.

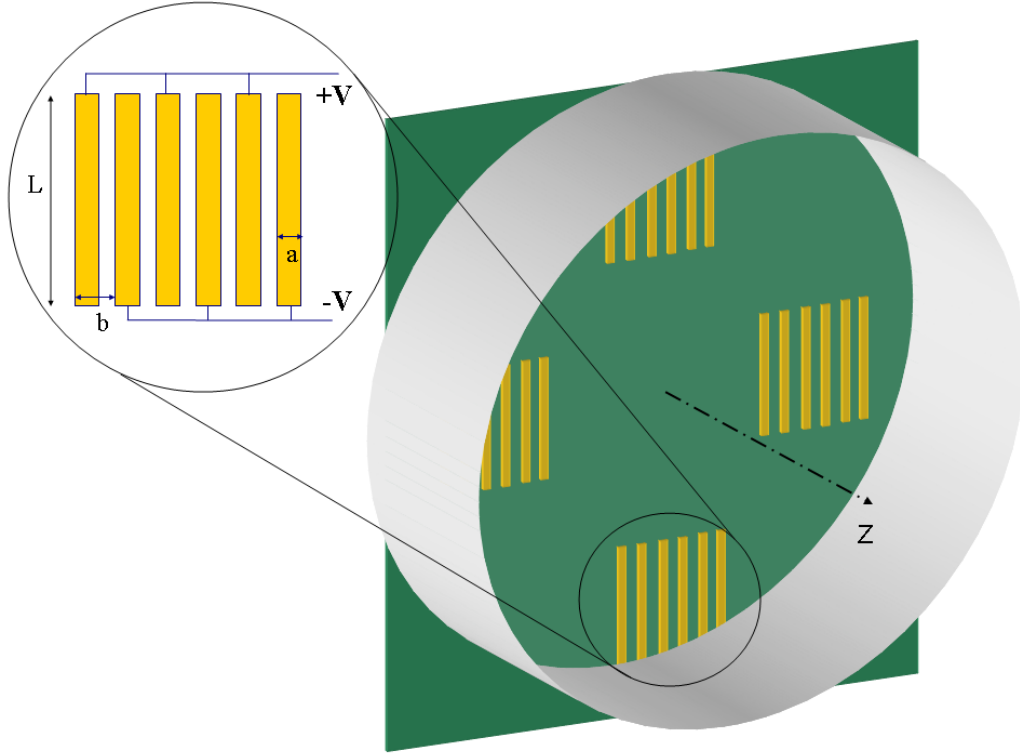


Figure 7.3: Electrostatic actuator and test mass. EA is composed by four strips elements. Each element (in the inset) is composed by electrodes of size  $a$  and length  $L$  and period  $b$  alternately polarized at two different voltages  $\pm V$ .

The working principle of an EA can be described by using the standard electrostatic. For a device as the one depicted in figure (7.3) characterized by a total capacity  $C$  (which depend on the geometric parameter of actuator-mass system) and polarized at a given voltage  $V$ , the resulting force on a dielectric mass is obtained by calculating the gradient of the stored energy in the system. The corresponding force along the  $z$  axis will be:

$$F_z = -\frac{1}{2} \left| \frac{dC}{dz} \right| V^2 \quad (7.1)$$

As the minus sign shows, the force described by the (7.1) is always attractive. This is not a real problem, the trick is the usual one employed each time we are dealing with an unidirectional actuation system. In fact, it is

possible to use an offset voltage that shifts the mass in some position and than applying the desired voltage (negative also this time) to *push* or *pull* the mirror with respect to the position corresponding to the offset value.

### 7.2.1 Electrostatic actuator model

Because of the not obvious geometrical contribution, the main element to model has been the total capacity  $C$  corresponding to each strips element showed in the inset of figure (7.3).

An analytical model has been developed by S. Grasso et al. [53] which make use of the method of the image charges in order to take into account the presence of the dielectric substrate and of the dielectric mirror. A finite element model has been then developed, mainly by I. Ricciardi, and written in *Matlab*<sup>®</sup> code [54].

In the following we recall the most important characteristics of this model.

Let consider the electrodes array showed in the inset of figure (7.3). This array is composed by an even number  $N$  of parallel conductive strips with period  $b$  and rectangular shape of length  $L$  and width  $a$ , laying on a substrate with relative dielectric constant equal to  $\epsilon_s$ , placed at distance  $x$  from the test mass having a relative dielectric constant equal to  $\epsilon_m$ , the capacity can be written as:

$$C(x) = C_\infty \alpha_m(\tilde{\alpha}, \tilde{x}, \epsilon_m) \quad (7.2)$$

where it has been defined the normalized strip width  $\tilde{\alpha} = \frac{a}{b}$ , the normalized distance  $\tilde{x} = \frac{x}{b}$  whereas  $\alpha_m$  is a function of the previously defined geometrical parameter which describes the effect of the mirror placed at distance  $x$  and  $C_\infty$  is the capacity of the isolated actuator defined as:

$$C_\infty = N\pi^2 L \frac{\epsilon_s + 1}{4} \epsilon_0 \alpha_s(\tilde{\alpha}) \quad (7.3)$$

where  $\alpha_s$  is a function of the normalized strip width that is proportional to the capacity linear density of the electrodes in free space, while the first term, depending on  $\epsilon_s$ , takes into account the effect of the actuator substrate.

In the model described in [53] and the subsequently translation in *Matlab*<sup>®</sup> code [54] a not negligible approximation is done. The actuator total capacity  $C$  is calculated in the approximation of infinite strips and taking into account only the contribution of the first image charges, both for the substrate and for the mirror. This means that experimentally measured capacities can have different values with respect to the theoretical prediction. This is particularly true for small values of  $x$  with respect to  $b$  because of the increasing weight of border effects and image charges as the distance decreases.

Taking into account the capacity expression (7.2) and assuming that the displacement of the test mass is small respect to the static distance  $d$  of the actuator, the corresponding force expressed by the (7.1) becomes:

$$F_z = -N\pi^2 L \frac{\epsilon_s + 1}{8} \epsilon_0 \alpha_s \left. \frac{d\alpha_m}{dz} \right|_{x=d} V^2 = -\alpha V^2 \quad (7.4)$$

in which  $\alpha$  is a global coupling constant of the electrostatic actuator expressed in  $\left[\frac{N}{V^2}\right]$  where all the characteristics, but the polarization voltage, are included.

## 7.2.2 Stray charge contribution

The model described until now does not take into account an additional contribution which, unlikely, is present.

Electrical charges due to several potential reason, could be present on the mirror surfaces. In fact a charging effect can occur during the pumping process necessary to put the interferometer in high vacuum. In this case the effect is due to friction when dust or other particles removed by the pumping process scrape across the interested surface [55].

Another potential source is cosmic rays, a calculation by Braginsky and others [56] suggests that a cascade of energy from a cosmic ray striking a dense material could deposit excess electrons. Mitrofanov et al. [57] have observed jumps in the charge on an optic element in vacuum of up to  $10^8 e^-/cm^2$ , which may be attributable to cosmic rays.

For this reason the previous expression (7.4) has to be modified to consider also the presence of a stray electric charge  $q$  on the dielectric mass. In this case, by making the simple approximation that this unwanted electric field is proportional to the polarization voltage applied to the actuator, it is possible to write:

$$F_z = -\alpha V^2 + \beta V \quad (7.5)$$

where the factor  $\beta$  is, in general, a function of the charge  $q$  (which is unlikely time dependent), of the distance  $x$  and of the actuator geometry. The effects of this term have been observed in different experiment [51] [58], and some techniques for its mitigation were already developed [59]. In the next section it will be showed our proposal as mitigation technique.

## 7.2.3 Bias modulation technique

The expression (7.5) show clearly two different problem for our purpose:

1. Non linearity because of the first term  $-\alpha V^2$
2. Stray charge effect (which is time dependent also)

The first problem is related to the fact that we wish to use the linear control theory when we drive the mirror in order to keep the interferometer locked on the right working point.

This constraint is not strictly necessary but, since it is more effective, in the framework of standard control systems, to work with linear actuation systems, a simple trick can be used.

Applying the square root of the driving signal we should use  $\sqrt{A} = V$ , we can consider our system as *linear* with respect this new variable  $A$  and this make possible to work with linear actuation systems again.

The second issue, related to the stray charge effect is, instead, a real problem. As example of stray charge effect on the position mass is shown the black curve in figure (7.4) where is evident a position drift. More spectacular effects arise, working near atmospheric pressure, when the mass is closer to the actuator and discharge or glare can be present.

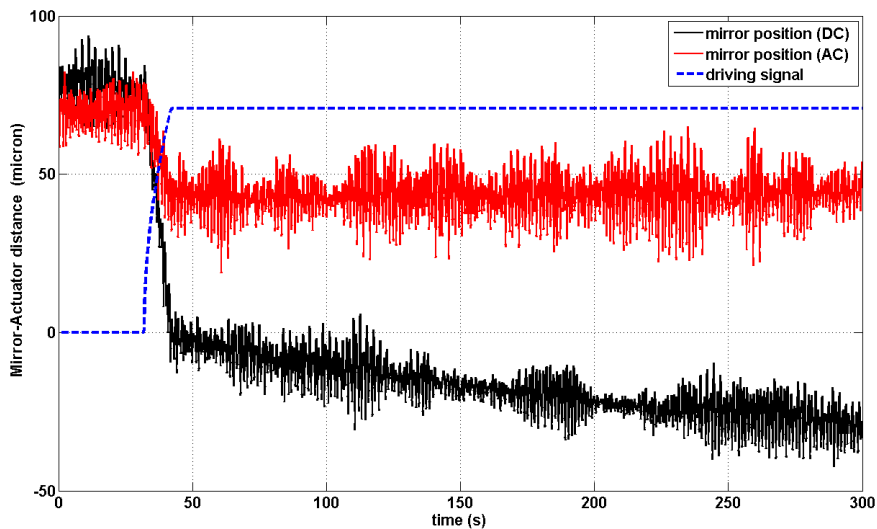


Figure 7.4: Drift position when different modulation signal are used. Black curve signal with no modulation, the position drift is evident; No drift is observed when a modulated signal is used (red curve); Dotted line shows when the polarization signal is applied on the actuator.

In order to reduce the effect of the stray charges, it is possible to modulate the driving signal, resulting in a zero averaged contribution of the linear term of the actuation force even in presence of charges on the test masses.

Summarizing, to take into account both of the problem let consider  $A(t)$  the driving signal we want to apply on the test mass,  $A_{DC}$  the voltage bias and  $2\pi\omega_M$  the modulation frequency of the full driving signal.

The square root of the two signal component  $A(t)$  and  $A_{DC}$  is computed and sent, with the modulation, to the actuator driver. In this way the voltage applied to the actuator is:

$$V = G\sqrt{A_{DC} + A(t)} \cos \omega_M t \quad (7.6)$$

where  $G$  is the gain of the EA driver. Using this voltage, the force exerted on the test mass expressed by the (7.5) becomes:

$$F_z = -\frac{1}{2}\alpha G^2 (A_{DC} + A(t)) (1 + 2 \cos \omega_M t) + \beta G \sqrt{A_{DC} + A(t)} \cos \omega_M t \quad (7.7)$$

By choosing the modulation frequency at enough high value in order to have negligible effects on the test mass motion and if the frequency content of the driving signal is much smaller with respect to  $\omega_M$ , the force expressed by the (7.7) only consists of a *DC* bias term and of a term proportional to the original driving signal  $A(t)$ .

### 7.3 Characterization of electrostatic actuators in air

Several models with different stripe number  $N$  and different parameters  $a$ ,  $b$  and  $L$  has been tested. Preliminary extensive capacity measurements have been performed in order to test and validate the model available for different parameters values.

In order to measure the actuator force exerted on a suspended dielectric mass with a mirror connected to one side, two different experimental set-up based on optical lever readout have been realized in order to perform measurements in air and in high vacuum environment.

In both of the cases, the actuator was mounted on a translation stage in order to easily change its distance from the suspended mass.

Optical lever system have been realized using a SLED (Superluminescent Light Emitting Diode) as light source. In particular the model used was a Qphotonics *QSDM - 830 - 2* emitting at  $\lambda = 830nm$ .

The choice of SLED as light source was mainly related to the low noise introduced in the position signal.

For this purpose, it has been measured the displacement noise introduced by different light source as He-Ne laser and laser diodes, detecting their output using a PSD photodiode, and analyzing the spectrum of the output signal. Some experimental result is shown in figure (7.5).

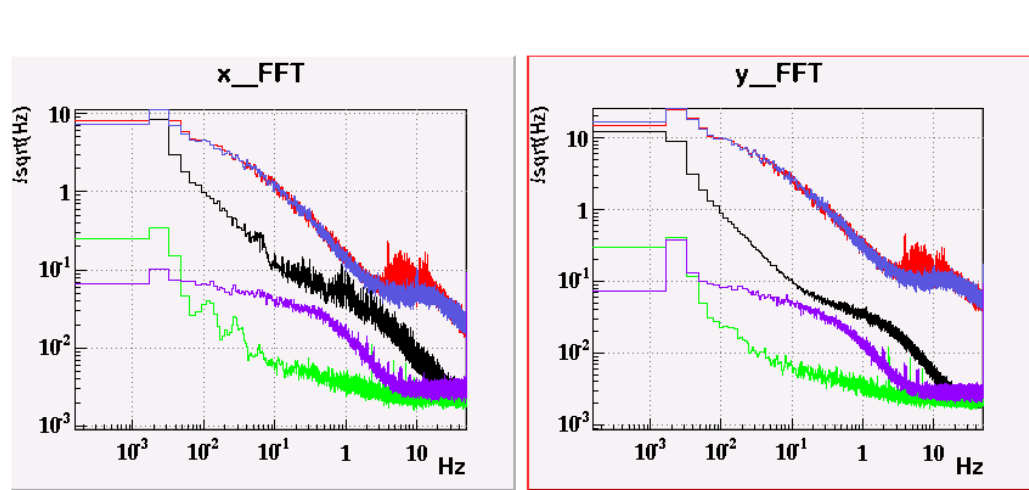


Figure 7.5: Output signal spectrum of different light source. The lowest (green) is referred to the SLED output.

The measurements have shown that the SLED presents a level noise about two order magnitude smaller respect to laser sources (laser diode and He-Ne laser).

Qphotonics *QSDM* – 830 – 2 provides an almost monochromatic beam characterized by an output power  $P_0 = 1mW$  and bandwidth  $\sim 20nm$ , but with a relatively short coherence length (well below  $1mm$ ).

In this optoelectronic devices there is no lasing action and this means that they are mode hopping free. The very short coherence length make the SLEDs unsuited to cases in which coherent light is needed, as in interferometric optical readouts. But for an optical lever there is no need of coherent light. On the contrary the use of incoherent light can be an advantage: the short coherence length avoids the effect of ghost fringes, due to multiple reflections within optical components or windows, which can, in some cases, spoil the sensitivity of the optical lever.

Using SLED as light source, an optical lever was realized in order to measure the force provided by different electrostatic actuators on suspended dielectric masses. The typical setup is shown in figure (7.6).

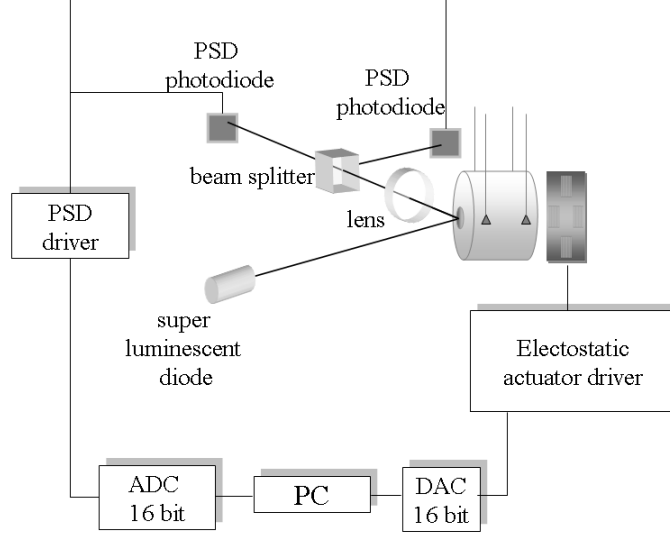


Figure 7.6: Optical lever setup used to measure mass displacement induced by an electrostatic actuator.

The measurements were performed by applying, by means of a high voltage amplifier (with amplification factor 200), a voltage (provided by a 16 bit DAC) of the form expressed by the equation (7.6), with a simple line at frequency  $f = 2\pi\omega \ll 2\pi\omega_M$  as driving signal:

$$V = G\sqrt{A_{DC} + A_{AC}\cos\omega t} \cos\omega_M t \quad (7.8)$$

In this way the component at angular frequency  $\omega$  of the force applied on the suspended mass was:

$$F_\omega = \frac{1}{2}\alpha G^2 A_{AC} = \frac{1}{2}\alpha V_{AC} \quad (7.9)$$

where

$$V_{AC} = G\sqrt{A_{AC}} \quad (7.10)$$

The effect of this force was measured by calculating the displacement spectrum of the mass, using the data coming from the PSD. Finally the displacement was converted in force by taking into account the theoretical transfer function of the suspended mass.

The actuation force was evaluated by sending different amplitude driving signals, at different distances between the actuator and the suspended mass.

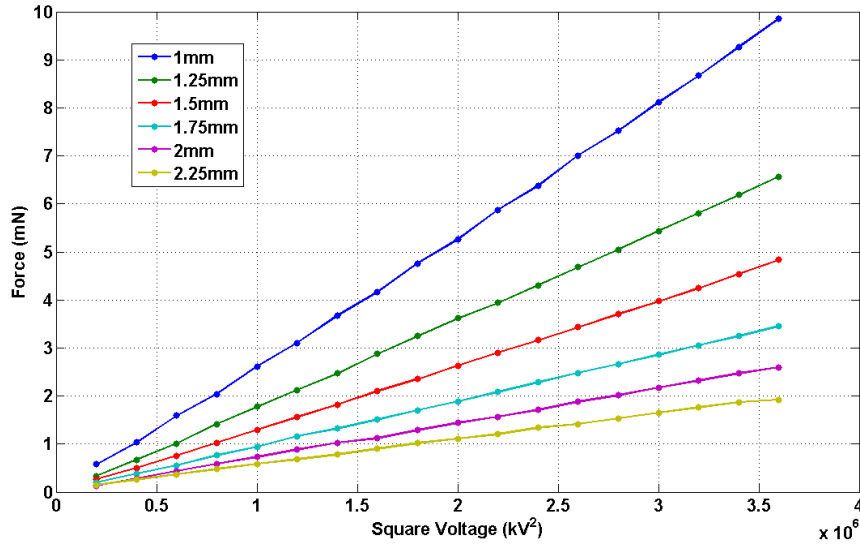


Figure 7.7: Examples of electrostatic actuator force VS square of voltage in order to show the linearity. The measurements have been performed for different distance actuator-mirror. The lines are eye-guide and not fit.

An example of measurements performed by means of optical levers is showed in figure (7.7).

An excellent linearity behavior was always found in all the distance range examined. In those distance range, force the order of magnitude was in the  $mN$  range (depending on the actuator model considered) and than suitable for the proposed application.

The same measurements showed in figure (7.7) as example, are plotted as a function of the actuator-mass distance in figure (7.8).

## 7.4 Characterization of electrostatic actuators in high vacuum

At atmospheric pressure, the increasing stray charges make impossible to send a driving signal without a modulation (DC bias condition), because the additional force, due to the spurious charge, bring an evident drift of the mass as shown in figure (7.4). Furthermore, medium vacuum condition also is not optimal, because for high voltage signal we produce unwanted glow discharges.

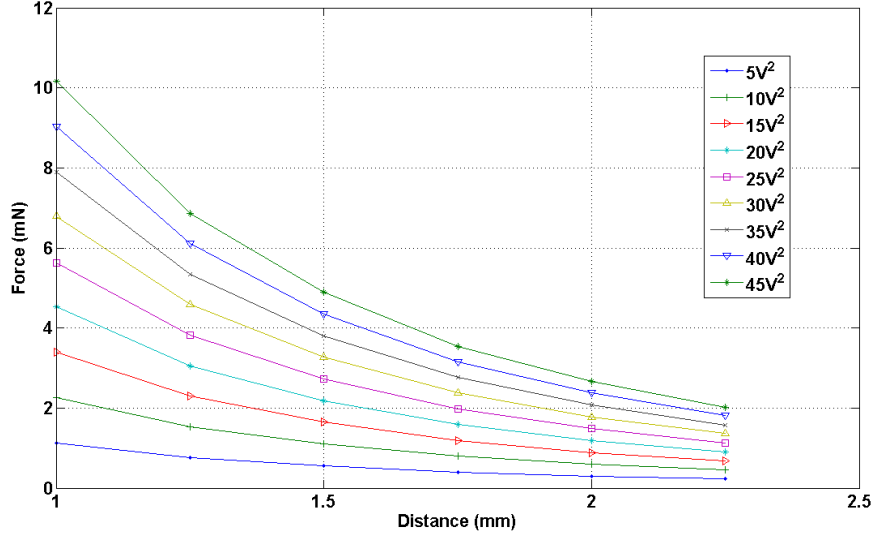


Figure 7.8: Force measurements as function of the distance. The measurements have been performed for different applied voltage.

The experimental set-up used to characterize the actuator consists of a suspended dielectric mass with a mirror placed on a side, whereas the readout system, was based on an optical lever. All the optical components, including the PSD and the actuator were placed in a vacuum chamber as depicted in figure (7.9). The probe beam of the optical lever was sent in the chamber by using a single mode optical fiber and guided to the mirror connected to the test mass by means of a suitable collimator.

The mass of the suspended element was  $m = 1.312Kg$ , while the length of the suspension wires was  $l = 0.18m$ .

As example of electrostatic actuator characterized, we can consider a model composed by  $N = 20$  strips, with length  $L = 8cm$ , width  $a = 3.2mm$ , and period  $b = 4mm$ . The relative dielectric constant of the EA substrate was  $\epsilon_s = 4.47$ , while the one of the dielectric mass  $\epsilon_m = 3.7$ .

The characterization of the actuator was performed in a way similar to the one used at atmospheric pressure: a simple line at frequency  $f = 2\pi\omega$  as driving signal of the form  $V = G\sqrt{A_{DC} + A_{AC}\cos\omega t}\cos\omega_M t$  at which correspond a force whit component  $F_\omega = \frac{1}{2}\alpha V_{AC}$  as described in the section (7.3).

Typical experimental results are shown in figure (7.10) and (7.11). The measurements in figure (7.10) are referred to a fixed distance between the

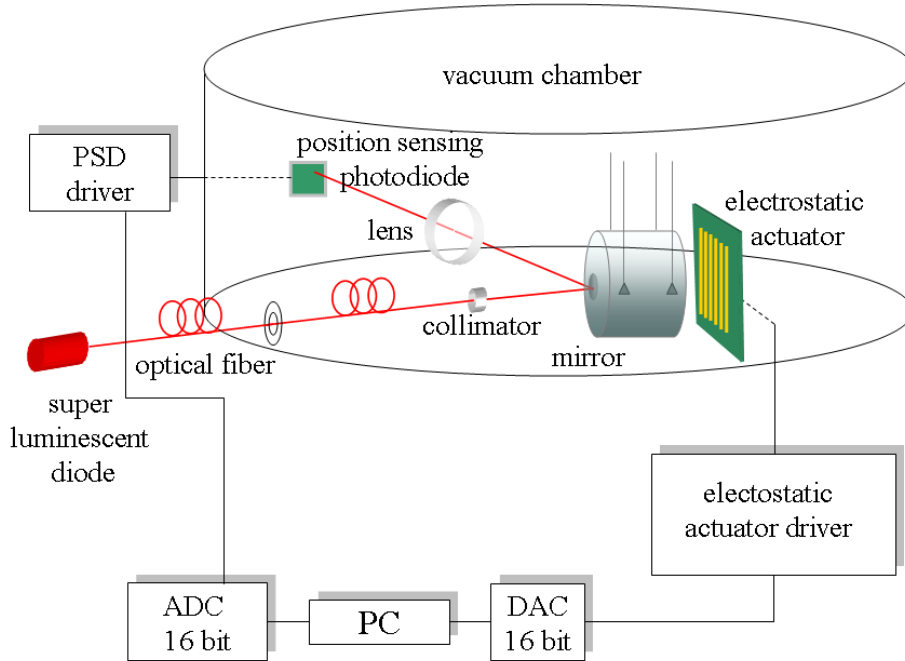


Figure 7.9: Experimental setup used to characterize electrostatic actuators in high vacuum condition.

actuator and the test mass equal to  $d = 3.5mm$ , using a fixed bias  $A_{DC} = 50V^2$ , that corresponds to a force equal to the half of the maximum force for the given output range of the HV amplifier.

Exciting the system by using excitation frequency as  $0.1Hz$  and  $20Hz$  (figure 7.12 and 7.11 respectively) we can neglect the transfer function details around the suspended mass resonance because both of them are far enough from the pendulum natural frequency  $f_0$ .

For each frequency a set of excitation amplitudes  $A_{AC}$ , in the range  $5 \div 45V^2$  were used.

All the measurements were repeated in *DC* bias ( $f_M = 0$ ) and alternate bias ( $f_M = 100Hz$ ) conditions.

In the measurements performed at  $f = 0.1Hz$  the filled dots represent the force measured in *AC* bias, both with positive or negative gain  $G$ , while the open circles are the force measured in *DC* bias with different  $G$  sign.

A deviation from the foreseen behavior are clearly visible for all the points

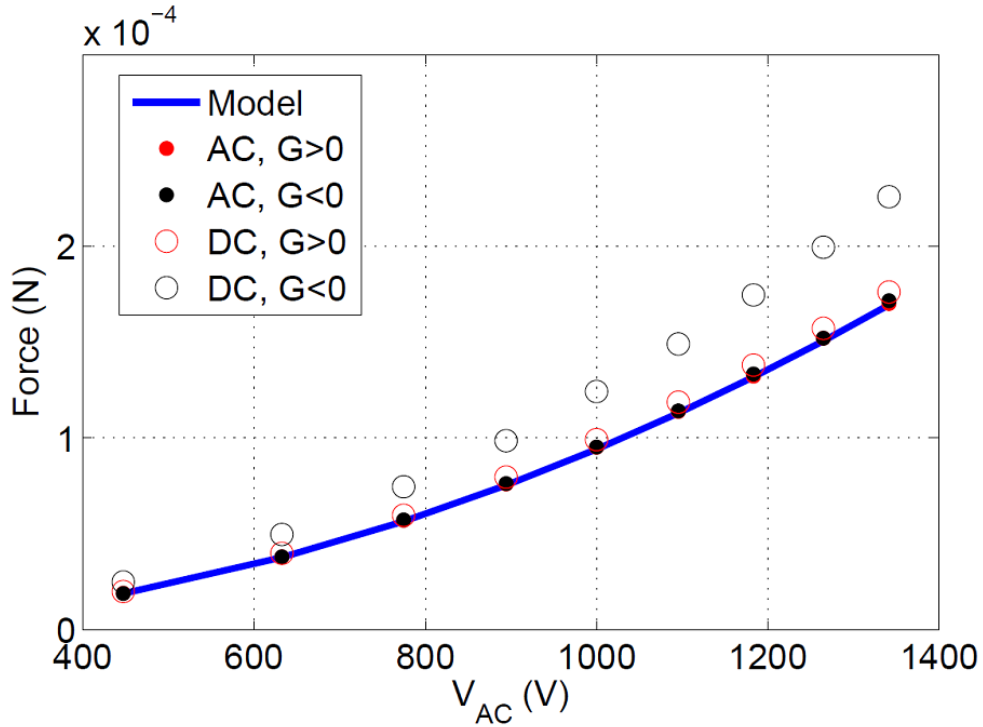


Figure 7.10: Force measurements in vacuum in different bias condition: modulated *AC* bias and in *DC* bias (both of them with positive and negative gain  $G$ ). A comparison with model prediction is also showed. Excitation frequency  $f = 0.1Hz$ . Distance actuator-mass  $z = 2.5mm$ .

in *DC* bias, in particular in the case of negative  $G$ . This lack of agreement between the model and the measurements is related to the presence of spurious charges on the dielectric suspended mass as it will be showed in the section (7.5).

The measurements performed in *AC* bias show the same behavior as the experimental data are almost overlapped. This is an additional confirm of the effectiveness of the alternate bias driving technique: it is insensitive to any static stray charge present on the test mass.

It should be said that, in order to compare the two different bias condition (*AC* and *DC*), the measurements in *AC* bias, were multiplied by a factor 2 in order to take into account the presence of the modulation at  $\omega_M$  that introduce a factor  $\frac{1}{2}$  in the force expression (see equation 7.9). All the measurements were performed in the same run, without opening the vacuum

chamber to not intentionally change the charge distribution on the test mass.

Similar result were obtained also for the  $f = 20Hz$  excitation as it is shown in figure (7.11).

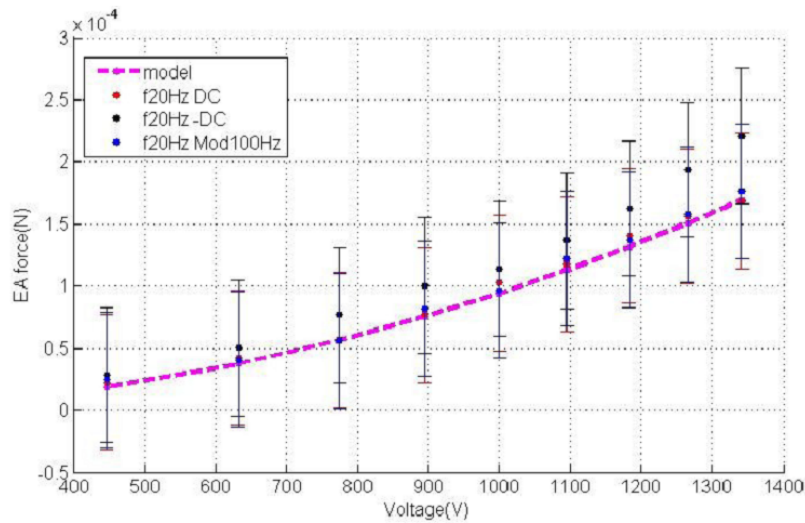


Figure 7.11: Measurements of the EA force for different driving amplitudes with and without modulation. The comparison with a numerical model is also reported. Excitation frequency  $f = 20Hz$ . Distance actuator-mass  $z = 2.5mm$ .

In the case showed in figure (7.11) the measurements were affected by a larger error, caused by the suspension filter. The corresponding displacement is not very large with respect to the noise floor and the final error on the force estimation is of the order of 20% making very difficult to decide if the points follow the model or not.

Performing additional measurements and plotting them on the same graph as figure (7.12) shows we can conclude that measurements made in *DC* bias given different results also in the same measuring conditions.

Such a disagreement can be explained as the stray charge present on the mass continuously changes with time. Instead the measurement in *AC*

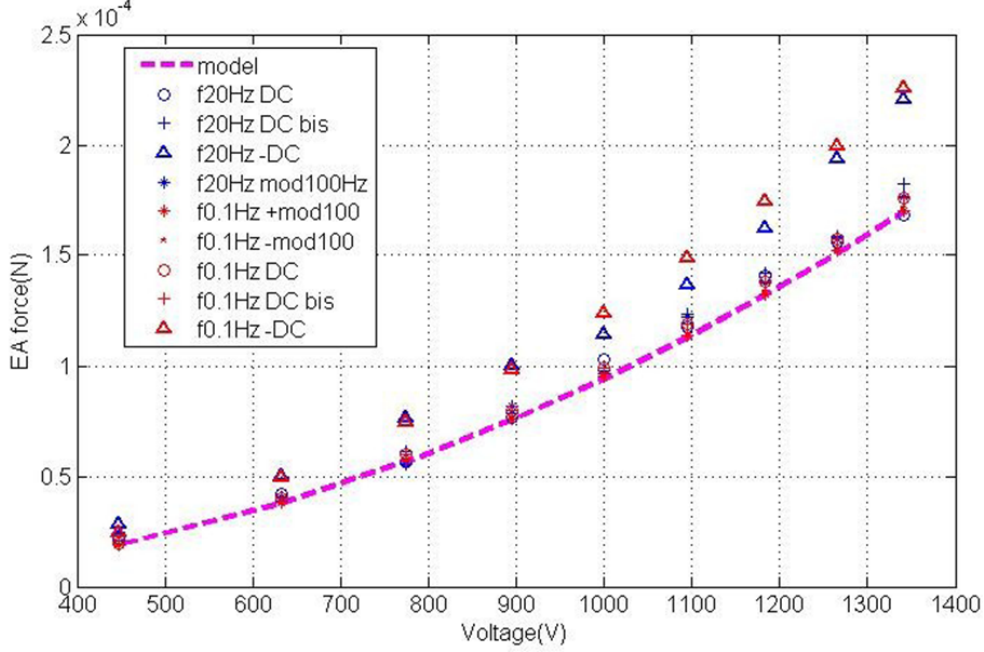


Figure 7.12: Measurements of the EA force for different driving amplitudes with and without modulation. The comparison with a numerical model is also reported. Excitation frequency  $f = 20Hz$  and  $f = 0.1Hz$ .

modulated bias are totally free by this problem.

## 7.5 Spurious charge detection technique

The modulation technique used to drive electrostatic actuator offers an additional advantage: allowing the spurious charge detection.

In fact comparison of the displacement spectrum obtained using a not modulated driving with the one obtained using a modulated driving will show us the presence of multiple frequency that are not present in the modulated case. Those peaks are related to the presence of spurious charge.

Let consider to apply a single frequency signal to our electrostatic actuator with the following form:

$$V = \sqrt{A_{DC} + A_{AC} \cos \omega t} \quad (7.11)$$

without the usual modulation term  $\cos \omega_M t$  that appears in the (7.8).

The application of the equation (7.5) on order to calculate the corresponding force provided by the actuator, will lead to:

$$F = -\alpha V^2 + \beta V = -\alpha(A_{DC} + A_{AC} \cos \omega t) + \beta \sqrt{A_{DC} + A_{AC} \cos \omega t} \quad (7.12)$$

where the first term, apart from the DC bias, consists of a signal at well determined frequency  $2\pi\omega$ , while the second term deserves some additional comment. In fact, it is possible to write:

$$\sqrt{A_{DC} + A_{AC} \cos \omega t} = \gamma \sqrt{1 + a \cos \omega t} \quad (7.13)$$

where  $a = \frac{A_{AC}}{A_{DC}}$  and  $\gamma = \sqrt{A_{DC}}$ . In addition it is possible to demonstrate [60] that:

$$\gamma \sqrt{1 + a \cos \omega t} = \gamma \left( c_0 + 2 \sum_{n=1}^{+\infty} c_n \cos n\omega t \right) \quad (7.14)$$

where the generic Fourier coefficient is:

$$c_n = -\frac{\Gamma(n - \frac{1}{2})}{2\sqrt{\pi}\Gamma(n + 1)} \left(-\frac{a}{2}\right)^n {}_2F_1\left(\frac{n}{2} - \frac{1}{4}, \frac{n}{2} + \frac{1}{4}, n + 1, a^2\right) \quad (7.15)$$

where  $\Gamma$  is the gamma function and  ${}_2F_1$  is the Gauss Hypergeometric function. Since for real cases  $a < 1$ , this relation foresees decreasing contribution for all the harmonics of the injected signal.

In fact, those lines are clearly visible in the spectrum at least until  $n = 3$  as it is shown in figure (7.13). Equation (7.14) also foresees a contribution on the fundamental frequency, that corresponds to the disagreement between the DC and AC measurements previously reported.

Thanks to this behavior, the chosen form of the driving, allows to easily detect the presence of charges on the test mass, simply by looking for the harmonics of the injected line.

In figure (7.14) the measured displacements ratio between the 2<sup>nd</sup> and 1<sup>st</sup> harmonics (upper graph) and the 3<sup>rd</sup> and 1<sup>st</sup> harmonics (lower graph) are reported as a function of the voltage  $V_{AC}$ . The measurements were done both for positive and negative  $G$ . The comparison with the model, based on the expression (7.15) is also given:  $R_i = c_i/c_1$ . The large error do not allow to state any definite conclusion, but the measurements largely follow the model.

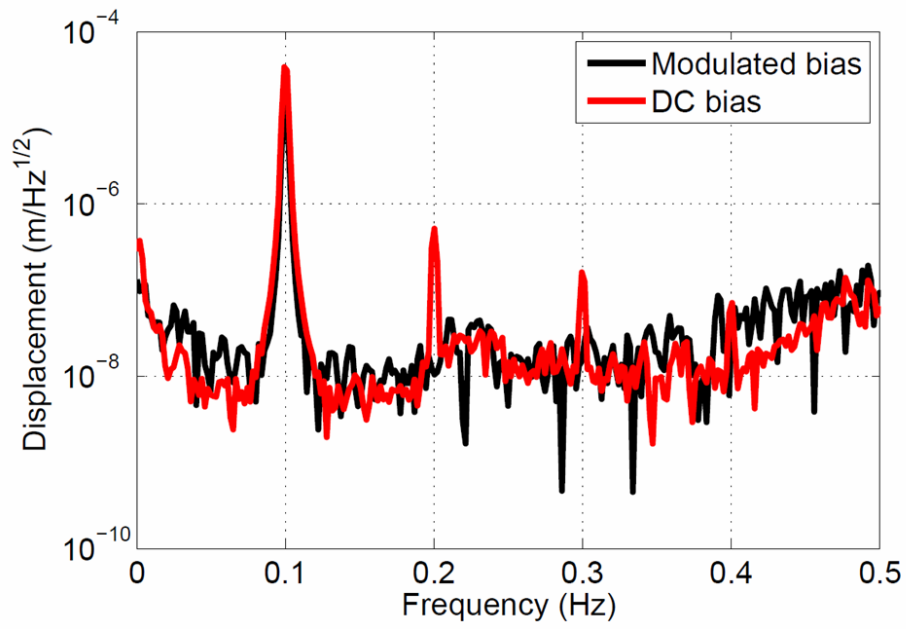


Figure 7.13: Spectra of the test mass displacement with the same actuation force, at  $f = 0.1\text{Hz}$  in two different bias conditions.

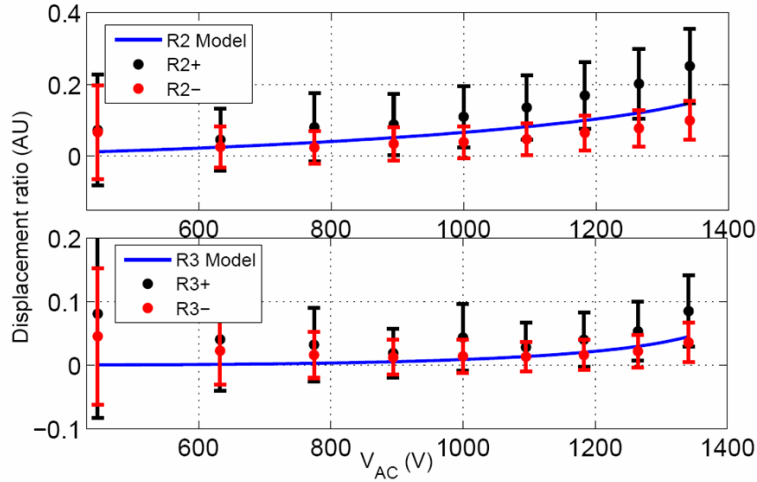


Figure 7.14: Ratios of the displacement harmonics compared with the model. Upper plot: ratio between the  $2^{nd}$  and  $1^{st}$  harmonics; lower plot:  $3^{rd}$  and  $1^{st}$  harmonics.

Then we can conclude that the modulation driving technique is not only useful and effective in order to drive electrostatic actuators avoiding the spurious charge effect but this technique also allows to easily detect the presence of external charges on the test mass giving a quantitative information on the charging level.

## 7.6 EA application on suspended Michelson interferometer control

Our main interest in electrostatic actuation comes to the mirror driving in order to lock interferometer on the right working point.

For this reason is fundamental to verify the possibility to use an electrostatic actuator for this purpose.

EA was used to lock a two stage suspended Michelson interferometer shown in figure (7.15). The position of the upper stage was controlled using coils-magnet actuators and optical levers for the position monitoring.

The bottom stage was different for each of the two suspension.

A first suspension was essentially a small bench used to hold the beam

splitter and one of the arms of the interferometer, that was folded to fit the available space.

The second suspension was a single dielectric cylindrical mass with a small mirror in the front, that constituted the end mirror of the second arm of the interferometer.

An electrostatic actuator was used to control the end mirror longitudinal motion.

All the system was placed in air and both the laser and the output photodiode were fixed on the optical bench. As source a frequency stabilized,  $1.5mW$ , HeNe laser was used, while for the optical lever very simple laser diodes, emitting  $3mW$  at  $680nm$  were employed.

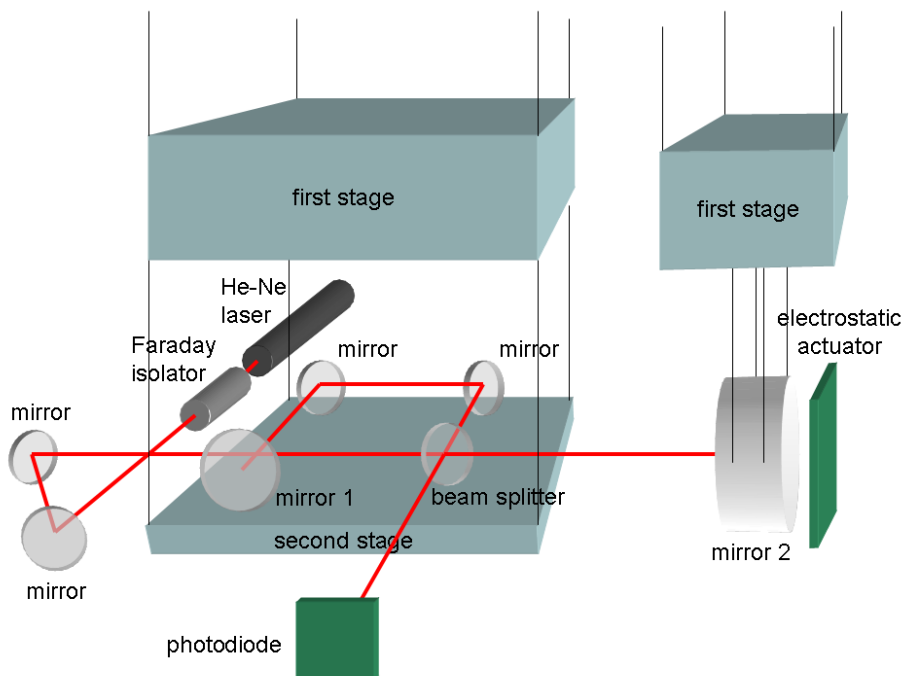


Figure 7.15: Double stage suspended Michelson interferometer.

The electrostatic actuator was constituted of a set of 4 patterns of electrostatic actuator very similar to the one schematically depicted in figure (7.3). The 4 elements geometry allowed to move the mirror along the optical axis as well as to rotate it around the two other axis. Each pattern consisted of 8 electrodes,  $4mm$  large and  $4cm$  long. The distance between the electrodes was  $1mm$ , that is the same value of the distance between the actuator and the suspended mass.

The interferometer control was divided in two parts. The first step was

to damp and position the suspended elements acting on the upper stage by using magnet-coils actuators. The control was realized by using a VME based digital control system. Once the damping was performed, the interferometer was manually aligned by acting on the reference values of the control loops, in order to maximize the contrast. Then, the second step was the interferometer lock by means of electrostatic actuators. The results are shown in figure (7.16).

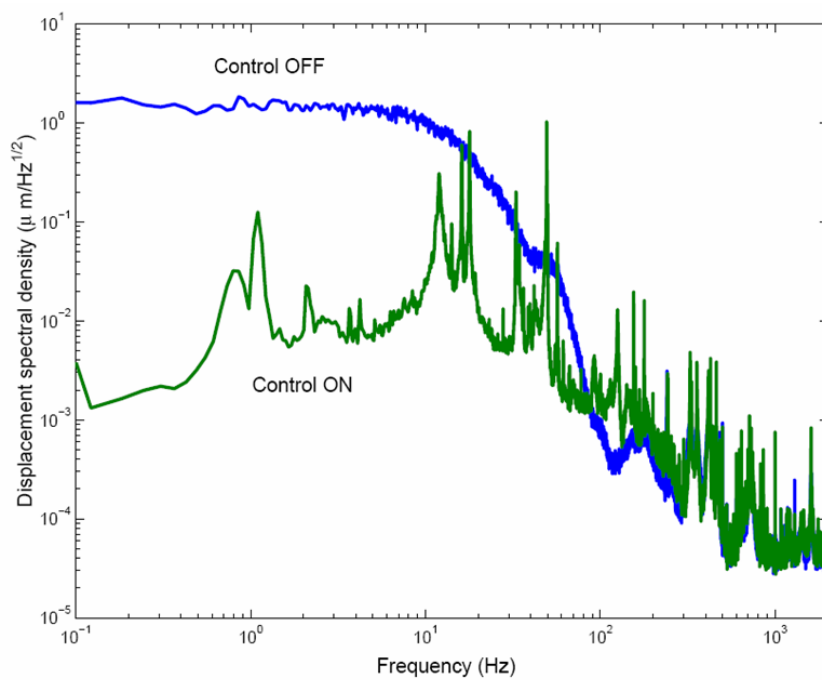


Figure 7.16: Displacement spectral density of the residual relative motion between the interferometer arms.

# Conclusions

This research activity was carried on in the framework of the INFN VIRGO experiment.

In the Naples VIRGO laboratory a prototype version of this interferometric detector is building. Thanks to this prototype interferometer it will be possible to develop and test new sensors as monolithic accelerometers, new actuation systems to employ in the mirror control (electrostatic actuators) and designing new control system for the interferometer.

All of this aspects are been topics of this thesis work.

Seismic noise limits Earth based gravitational wave interferometric detectors at low frequencies. The detection threshold can be lowered down to a few Hz using a seismic attenuation system based on Inverted Pendulum which sustains interferometer optical components by means of a pendula chain. The IP, acting as a mechanical low pass filter, is able to filter out seismic noise and at the same time it provides a quasi-inertial stage where the suspension point of the pendula chain lies. The IP is a three degrees of freedom system, it has two translational and one rotational modes. Therefore, to fully determinate its position, three independent sensors have been mounted at the periphery of the IP top table. For the same reason, three independent actuators have been used to move the Inverted Pendulum. The geometrical position of the sensors was different from actuator positions, in addition, both of them were not connected to the normal modes of the IP. Each sensor was sensitive in all the three IP normal modes and each actuator will generate movements which are a mix of the three modes.

To take advantage of controlling a SISO system instead of a MIMO system, a diagonalization of the actuation and detection system was needed. An original and model independent experimental procedure for determining the system dynamic, giving an effective diagonalization has been developed and tested.

Preliminary tests, performed on a simpler system have been successful. The same procedure has been extensively used on a more complex mechanical system. The method developed and described in this thesis offers the

undoubted advantage to be *model independent*. As a consequence of this peculiarity, it can be easily adopted in complex system which presents some difficulties into determining a perfect model to describe the system response (obviously if degrees of freedom are not intrinsically entangled).

This point makes such a method very flexible and suitable to be applied in different physical systems. Especially systems in which could be difficult to find a correct model to describe them.

But this is not the only advantage showed by this method:

- it does not require two distinct steps to obtain sensing and driving matrices (as usually done in VIRGO, TAMA, etc.).
- It works even with degenerate systems.
- It does not require the experimentalist to provide for frequency ranges and geometric positions of the actuators and sensors system.

Besides activity on the IP control, the PhD activity has been related to the development and test innovative sensors and actuators which equipped the seismic attenuation system. All the sensors and actuators are special purpose devices and no commercial device is available with same features.

To improve feedback control system performance and more generally the whole interferometric gravitational waves detector, new monolithic accelerometers has been developed.

This device is basically a monolithic tunable folded pendulum, shaped with precision machining and electric-discharge-machining, that can be used both as seismometer and, in a force-feedback configuration, as accelerometer. It is a very compact instrument, very sensitive in the low-frequency seismic noise band, with a very good immunity to environmental noises.

One of the most important parameter to determine the performance of this sensor is the mechanical quality factor. To this purpose, a vacuum chamber has been set up and mechanical quality factor measurements has been performed on different accelerometers model. In particular, one of the model tested had shown exceptional quality factor. Another parameter which determines the overall performance is the frequency resonance. The accelerometers are expressly designed to change this frequency because of the presence of a tuning mass. The measurements have shown very low frequency resonance values.

This characteristic make this sensor interesting as showing features that overcome commercial devices.

Another interesting characteristic of this sensor is the integrated laser optical readout consisting of an optical lever and an interferometer. The

theoretical sensitivity curves was in a very good agreement with the measurements. A direct comparison of its performances with a commercial device (the STS-2) shows that better performances have been reached with the interferometric readout ( $\approx 10^{-12} m/\sqrt{Hz}$  in the band  $10^{-1} \div 10 Hz$ ) as seismometer. Experimental results as accelerometer (force feed-back configuration) have been also presented and discussed.

Additional research activity was related to the design and characterization of an alternate biased electrostatic actuator to be employed for the control of the last suspended stage interferometer mirror. Electrostatic actuators are the most promising devices for mirror control for next generation of interferometric gravitational wave detectors.

An accurate characterization of such actuators has been performed by varying the mirror-actuator distance and the bias amplitude.

Those tests was obtained in different environmental condition and for different actuator models.

The experimental results were compared to the prediction of a numerical model taking into account the actuator geometry and the working conditions.

An original driving technique for electrostatic actuators, making use of alternate bias to minimize the effect of stray charges present on the dielectric test mass, was developed and characterized. The experimental results confirmed the effectiveness of this technique compared with the standard DC bias. Devices driven in this way showed a very good agreement with the theoretical model of electrostatic actuation. Moreover this technique also allows to easily detect the presence of spurious electric charges on the test mass and gives quantitative indications on the level of charging.

Additionally, electrostatic actuators was used to lock a double stage suspended Michelson interferometer showing their purpose feasibility.

# Appendix A

## Viscous and internal damping

We are interested to find the expression of the mechanical quality factor  $Q$  and the thermal noise in mechanical oscillating system

In order to determine the contribution of the thermal noise it is possible to make use of the *Fluctuation-Dissipation Theorem* [3] according to which, if we consider a system under a random force  $F_{th}$  with a white spectral density, the system transfer function  $H(\omega)$  is strictly connected with the power spectrum:

$$x_{therm}^2(\omega) = \frac{4K_B T}{\omega} \Im[H(\omega)] \quad (\text{A.1})$$

where  $K_B$  is the Boltzmann constant,  $T$  is the absolute temperature. Different definitions of quality factor  $Q$  are possible. For instance, the  $Q$  factor is  $2\pi$  times the ratio of the stored energy over the energy dissipated per oscillation cycle, or equivalently the ratio of the stored energy to the energy dissipated per radian of the oscillation.

$$Q = 2\pi \frac{\text{stored energy}}{\text{dissipated energy per cycle}} \quad (\text{A.2})$$

Taking into account this definition, if the degradation of the quality factor is due to different contributions (to simplify we consider two contributions only):

$$Q = 2\pi \frac{E_{stored}}{E_1^{diss} + E_2^{diss}} \quad (\text{A.3})$$

where  $E_{stored}$  is the system stored energy and  $E_i^{diss}$  are the dissipated energy per cycle  $i^{th}$  contribution.

$$\frac{1}{Q} = \frac{1}{2\pi} \left( \frac{E_1^{diss}}{E_{stored}} + \frac{E_2^{diss}}{E_{stored}} \right) = \frac{1}{Q_1} + \frac{1}{Q_2} \quad (\text{A.4})$$

In other words, different contributions on the total quality factor value have to be added in parallel.

In the following we will make large use of a different and more *operative* definition in terms of resonance bandwidth. We will consider the Q factor as the ratio of the resonance frequency over the full width at half-maximum (FWHM) bandwidth of the resonance.

$$Q = \frac{\omega_0}{\Delta\omega} \quad (\text{A.5})$$

where  $\omega_0$  is the resonant frequency and  $\Delta\omega$  is the width of the range of frequencies for which the energy is at least half its peak value.

## A.1 Viscous damping

Let consider a classical mass-spring system with mass  $m$  immersed in a thermal bath (then subject to a random force  $F_{th}$  of thermal origin).

Its equation of motion is the well known Langevin equation:

$$m\ddot{x} + \beta\dot{x} + kx = F_{th} \quad (\text{A.6})$$

where  $\beta$  is related to the medium viscosity and  $k$  is the spring elasticity.

This equation is easily solved in the frequency domain, by the usual replacement  $x(t) \rightarrow x(\omega)e^{i\omega t}$  leading to:

$$-\omega^2 mx(\omega) + i\omega\beta x(\omega) + kx(\omega) = F_{th}(\omega) \quad (\text{A.7})$$

The system transfer function will be:

$$H(\omega) = \frac{1}{m((\omega_0^2 - \omega^2) + i\omega\frac{\beta}{m})} \quad (\text{A.8})$$

where  $\omega_0^2 = \frac{k}{m}$  is the square of the resonance frequency.

The application of the fluctuation-dissipation theorem will give as:

$$x_{visc}^2(\omega) = \frac{4K_B T\beta}{m^2(\omega_0^2 - \omega^2)^2 + \omega^2\beta^2} \quad (\text{A.9})$$

The maximum value for  $x_{therm}^2(\omega)$  is:

$$(x_{visc}^2)_{max} = \frac{4K_B T\beta}{\omega^2\beta^2} \quad (\text{A.10})$$

The  $\omega$  values that render the power spectrum the half of the maximum value solve the equation:

$$(\omega_0 - \omega)^2 = \frac{\beta^2}{4m^2} \quad (\text{A.11})$$

whose solutions are:

$$\omega_1 = \omega_0 + \frac{\beta}{4m} \quad (\text{A.12})$$

and

$$\omega_2 = \omega_0 - \frac{\beta}{4m} \quad (\text{A.13})$$

then:

$$Q_{visc} = \frac{\omega_0}{\Delta\omega} = \frac{\omega_0}{\omega_1 - \omega_2} = \frac{\omega_0 m}{\beta} \quad (\text{A.14})$$

## A.2 Internal damping

Internal damping in materials has been found to obey an extension of Hookes law, which can be approximated by:

$$F = -k(1 + i\phi(\omega))x \quad (\text{A.15})$$

A fraction  $2\pi\phi$  of the energy stored in the oscillatory motion is being dissipated during each cycle. Lets consider in our hypothetical mechanical system the only presence of internal damping. By substituting a general spring imaginary constant in the equation motion in the absence of external damping, we will have:

$$m\ddot{x} + k(1 + i\phi(\omega))x = F_{th} \quad (\text{A.16})$$

that in the frequency domain becomes:

$$-\omega^2 mx(\omega) + k(1 + i\phi(\omega))x(\omega) = F_{th}(\omega) \quad (\text{A.17})$$

Then, the system transfer function will be:

$$H(\omega) = \frac{1}{m(\omega_0^2 - \omega^2) + i\omega_0^2 m\phi(\omega)} \quad (\text{A.18})$$

The application of the fluctuation-dissipation theorem will give as:

$$x_{int}^2(\omega) = \frac{4K_B T \phi(\omega) \omega_0^2}{\omega m^2 ((\omega_0^2 - \omega^2)^2 + (\omega_0^2 \phi(\omega))^2)} \quad (\text{A.19})$$

The maximum value is:

$$(x_{int}^2)_{max} = \frac{4K_B T}{m\omega_0^3 \phi^2(\omega_0)} \quad (\text{A.20})$$

The pulsation values that render the power spectrum the half of the maximum value solve the equation:

$$(\omega_0 - \omega)^2 = \frac{\omega_0^2 \phi(\omega)^2}{4} \quad (\text{A.21})$$

whose solutions are:

$$\omega_1 = \omega_0 + \frac{\omega_0 \phi(\omega)}{m} \quad (\text{A.22})$$

and

$$\omega_2 = \omega_0 - \frac{\omega_0 \phi(\omega)}{m} \quad (\text{A.23})$$

then:

$$Q_{int} = \frac{\omega_0}{\Delta\omega} = \frac{\omega_0}{\omega_1 - \omega_2} = \frac{\omega_0}{\omega_0 \phi(\omega_0)} = \frac{1}{\phi(\omega_0)} \quad (\text{A.24})$$

### A.3 Internal and external damping

Lets now consider the case of the simultaneous presence of internal and external damping on our system. The equation of motion can be written as:

$$m\ddot{x} + \beta\dot{x} + k(1 + i\phi(\omega))x = F_{th} \quad (\text{A.25})$$

that in the frequency domain becomes:

$$-\omega^2 m x(\omega) + k(1 + i\phi(\omega))x(\omega) + i\omega\beta x(\omega) = F_{th}(\omega) \quad (\text{A.26})$$

As usual, the system transfer function will be:

$$H(\omega) = \frac{1}{m(\omega_0^2 - \omega^2) + i\beta\omega + i\omega_0^2 m \phi(\omega)} \quad (\text{A.27})$$

Using the fluctuation-dissipation theorem we will have:

$$x_{therm}^2(\omega) = \frac{4K_B T (\omega\beta + \omega_0^2 \phi(\omega)m)}{\omega [m^2(\omega_0^2 - \omega^2)^2 + (\omega\beta + m\omega_0^2 \phi(\omega))^2]} \quad (\text{A.28})$$

In order to evaluate the  $Q$  value we consider the power spectrum at the half of the maximum value solving the equation:

$$(\omega_0 - \omega)^2 = \frac{1}{4m^2}(\beta + m\omega_0\phi)^2 \quad (\text{A.29})$$

whose solutions are:

$$\omega_1 = \omega_0 + \frac{1}{2m}(\beta + m\omega_0\phi) \quad (\text{A.30})$$

and

$$\omega_2 = \omega_0 - \frac{1}{2m}(\beta + m\omega_0\phi) \quad (\text{A.31})$$

then:

$$Q = \frac{\omega_0}{\Delta\omega} = \frac{\omega_0}{\omega_1 - \omega_2} = \frac{m\omega_0}{\beta + \omega_0\phi(\omega_0)m} \quad (\text{A.32})$$

The same result can be obtained taking into account the equation (A.4):

$$\frac{1}{Q} = \frac{1}{Q_{int}} + \frac{1}{Q_{visc}} \quad (\text{A.33})$$

an by using the (A.24) and (A.14):

$$Q_{int} = \frac{1}{\phi(\omega_0)}$$

$$Q_{visc} = \frac{\omega_0 m}{\beta}$$

it is easy to find again the result of the equation (A.32).

# Appendix B

## Optical levers

Despite the simplicity of their working principle, optical levers offer the undoubt advantage to be a non-contact position detection system and a sensitivity that frequently can satisfy the experiment requirements. In the simplest form, an optical lever is composed by means of a specular surface we wish to monitor the position (or a mirror connected to the surface) an optical beam (provided for instance by a laser) and a photodiode able to detect the beam position impinging on its window (quadrant photodiode or PSD). A simple scheme is depicted in figure (B.1).

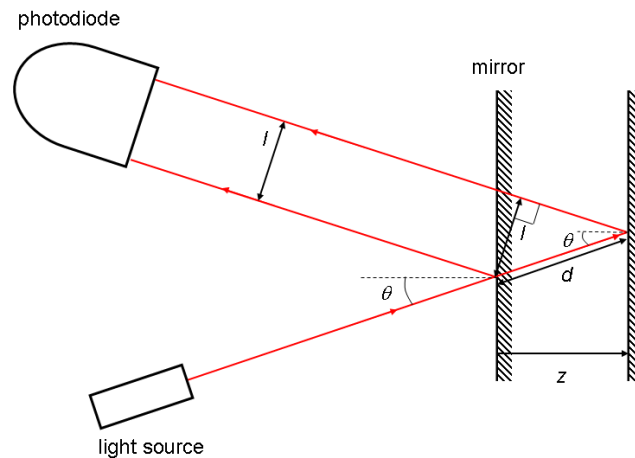


Figure B.1: Mirror translation as detected by means of an optical lever.

If we call  $z$  a mirror translation, the corresponding beam displacement detected by a photodiode will be  $l$ .

From the figure (B.1) it is very easy to find that  $z = d \cos \theta$  and  $l = d \sin 2\theta$  where  $\theta$  is the incidence angle. Then, the mirror translation  $z$  is related to the signal  $l$  provided by the photodiode as:

$$z = \frac{l \cos \theta}{\sin 2\theta} = \frac{l \cos \theta}{2 \sin \theta \cos \theta} = \frac{2l}{\sin \theta} \quad (\text{B.1})$$

Let now consider a mirror rotation of an amount  $\theta$  around an axis passing to the beam impinging point and orthogonal to the beam plane as depicted in figure (B.2). The simple application of the Snell-Descartes reflection law, will lead to a  $2\theta$  deviation of the reflected beam after the rotation with respect to the not rotated one. The corresponding impinging point displacement on the photodetector will depend by the detector-mirror distance and by the angles between the photodiode window and the beams.

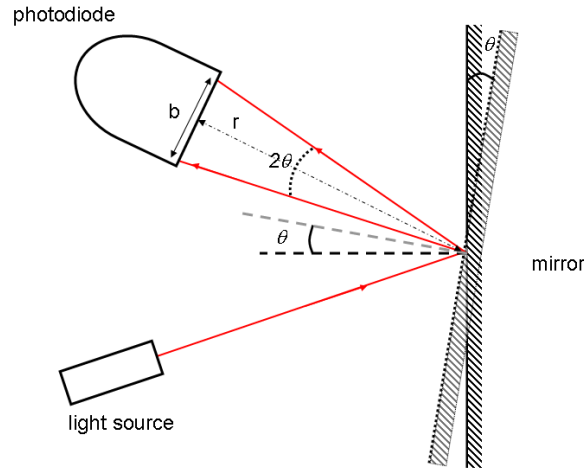


Figure B.2: Mirror rotation as detected by means of an optical lever.

If it is possible to consider small angle  $\theta$  and beams almost orthogonal to the photodiode, the corresponding beam displacement  $b$  on the photodiode will be:

$$b = 2r \tan \theta \quad (\text{B.2})$$

where  $r$  is the distance between the beam impinging point and the photodetector.

A more realistic case will be a combination of mirror rotation and translation.

In order to show the effects of this mirror roto-translation it convenient to adopt the *ray transfer matrix method* or *ABCD matrix description* often used in paraxial<sup>1</sup> optics.

In this description each ray is characterized by a couple of elements:

$$\begin{pmatrix} x \\ \theta \end{pmatrix} \quad (\text{B.3})$$

where  $x$  and  $\theta$  are the ray distance from the optical axis and its inclination angle respectively. At the same way, each medium is described by means of a  $2 \times 2$  matrix (that give the name to this description).

We want to show that there are specific photodiode-mirror distances that allow the photodiode to detect only translation or only rotation of the mirror. In other words, it is possible to disentangle the mirror motion in its rotational motion and its translational motion by means of a correct choice of the optical element distances.

For our purpose, we are interested to a free propagation for a generic distance  $d$  and the propagation through a thin lens of focal length  $f$ . The corresponding matrices are respectively:

$$\begin{pmatrix} 1 & d \\ 0 & 1 \end{pmatrix} \quad (\text{B.4})$$

and

$$\begin{pmatrix} 1 & 0 \\ -\frac{1}{f} & 1 \end{pmatrix} \quad (\text{B.5})$$

Let call  $a$  the distance mirror-lens and  $b$  the distance lens-detector as showed in figure (B.3). We are interested to the relation between the optical vector describing the beam on the mirror  $(x_M, \theta_M)$  and the optical vector describing the beam on the detector  $(x_D, \theta_D)$ .

By using the ray transfer matrices it is possible to write:

$$\begin{pmatrix} x_D \\ \theta_D \end{pmatrix} = \begin{pmatrix} 1 & b \\ 0 & 1 \end{pmatrix} \cdot \begin{pmatrix} 1 & 0 \\ -\frac{1}{f} & 1 \end{pmatrix} \cdot \begin{pmatrix} 1 & a \\ 0 & 1 \end{pmatrix} \cdot \begin{pmatrix} x_M \\ \theta_M \end{pmatrix} \quad (\text{B.6})$$

---

<sup>1</sup>In the paraxial approximation all rays are assumed to be at a small angle and a small distance relatively to the system optical axis.

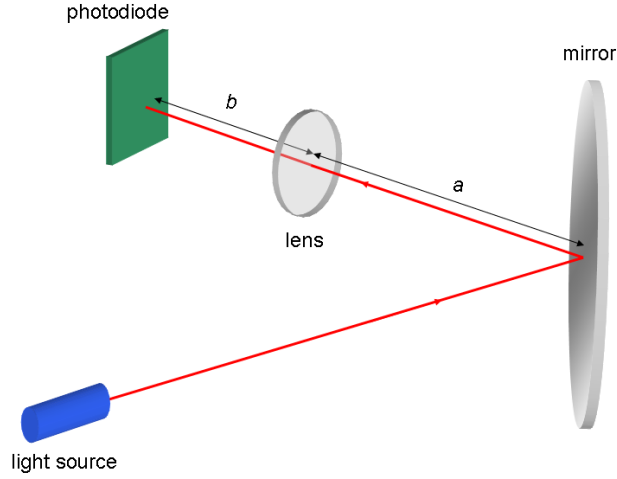


Figure B.3: Distances among elements of an optical lever.

Then:

$$\begin{pmatrix} x_D \\ \theta_D \end{pmatrix} = \begin{pmatrix} 1 - \frac{b}{f} & a + b - \frac{ab}{f} \\ -\frac{1}{f} & 1 - \frac{a}{f} \end{pmatrix} \cdot \begin{pmatrix} x_M \\ \theta_M \end{pmatrix} \quad (\text{B.7})$$

In particular we will have:

$$x_D = \left(1 - \frac{b}{f}\right) x_M + \left(a + b - \frac{ab}{f}\right) \theta_M \quad (\text{B.8})$$

The (B.8) is then composed by a first term which is proportional to the beam coordinate on the mirror  $x_M$  and a second term related to its angular tilt  $\theta_M$ .

This means that placing the photodiode at a distance  $b = f$  from the lens, the first term in the (B.8) vanishes and we have  $x_D = f\theta$ . Therefore, this case corresponds to detect mirror tilt only.

Instead, by placing the photodiode at distance  $b = -\frac{af}{f-a}$  the (B.8) will be reduced to  $x_D = \left(\frac{f}{f-a}\right) \theta_M$  because of the second term vanishing. Therefore, this case corresponds to detect a mirror translation.

In order to detect simultaneously translation and rotation of the mirror it is possible to place a beam splitter after the lens and place two different photodiodes at different distances that will be able to detect separately rotation

and translation.

# Acknowledgments

It is a pleasure to thank the people who have contributed each in their own way in the work that has led to this thesis. First of all I would like to thank my parents for supporting me during this years (and not only) and Antonella (for supporting me each day).

I would like to thank Prof. Leopoldo Milano for the opportunity he gave me to join the Naples VIRGO group.

My deepest gratitude is to my supervisor Prof. Rosario De Rosa. His inspiration and dedication to the research activity has been an example and his deep knowledge of different fields, stimulated me throughout the whole research. For all this I am much obliged to him.

Further I would like to thank all the members of my laboratory.

My thoughts go to Fabio, Simona, Maria, Luca, Luciano, Saverio, Silvia, Mariafelicia, Gerardo, Fabrizio, Silvio, Fausto and Daniele. With some of them I've shared laboratory experiences, with all of them I spent pleasant time here in Naples or in Cascina. My laboratory life would have been poorer without all the people of my group.

Among my laboratory members, Antonino deserves a special mention. He's a friend before to be a colleague. It has been an unexpected luck to be together again. Part of my work would have been impossible without him. I have been happy to share my desk with him.

Further I thank everyone, I have not mentioned earlier, who contributed in any positive way.

# Bibliography

- [1] C.W.Misner, K.S.Thorne, J.Wheeler, Gravitation, San Francisco (1973).
- [2] S. Weinberg, Gravitation and Cosmology, New York (1972).
- [3] P. R. Saulson, Fundamentals of Interferometric Gravitational Wave Detectors, World Scientific (1994).
- [4] R. A. Hulse, J. H. Taylor, Discovery of a pulsar in a binary system, ApJ 195 51-53 (1975)
- [5] J.M. Weisberg, J.H. Taylor, Relativistic Binary Pulsar B1913+16: Thirty Years of Observations and Analysis, arXiv:astro-ph/0407149v1 (2004)
- [6] R. Prix, Gravitational Waves from Spinning Neutron Stars, Neutron Stars and Pulsars, ed. W. Becker, Springer-Verlag (2009), p. 651
- [7] LIGO and Virgo Scientific Collaborations, Search for gravitational-wave bursts associated with gamma-ray bursts using data from LIGO Science Run 5 and Virgo Science Run 1, The Astrophysical Journal, 715:14381452, 2010 June 1
- [8] LIGO and Virgo Scientific Collaborations, An upper limit on the stochastic gravitational-wave background of cosmological origin, Nature, 460 (2009), 990-994
- [9] W.M.Folkner et al.: LISA Mission Concept Study, JPL Publication 9716 (1998); see also <http://lisa.jpl.nasa.gov>
- [10] T. Accadia *et al.* "Status and perspectives of the Virgo gravitational wave detector " *J. Phys.: Conf. Ser.* vol.203, 012074, 2010.
- [11] LIGO Laser Interferometer Gravitational-Waves Observatory. [Online]. Available: <http://www.ligo.caltech.edu>

- [12] GEO600 The German-British Gravitational Wave Detector. [Online]. Available: <http://geo600.aei.mpg.de/>
- [13] M. Ando *et al* "Current status of the TAMA300 gravitational-wave detector" *Class. Quantum Grav.* 22 S881 2005.
- [14] A. Giazotto, *Proceedings of 7th Conference on General Relativity and Gravitational Physics*, eds. U. Bruzzo, R. Cianci and E. Massa, pp. 449-63, World Scientific, Singapore (1987).
- [15] D. Shoemaker *et al* *Phys.Rev. D* 38, p.423-32 (1988).
- [16] R. Weiss MIT Quart. Progress Report No. 105 (1972).
- [17] M. Bernardini *et al.* *Class. Quantum Grav.* 15 1-24 (1997).
- [18] P. Lorrain, "Double-pendulum vibration isolator or seismograph" *Rev. Sci. Instrum.* 48, 1397-9 (1977).
- [19] H. Goldstein, *Classical Mechanics* Addison-Wesley, Reading, 1980. In order to allow for measurements with the
- [20] G. Saul, *et al.*, Source Book on Maraging Steels, American Society for Metals, Cleveland, (1979).
- [21] A. Takamori *et al.* *Nuclear Instruments and Methods in Physics Research A* 582 683692 (2007).
- [22] G. Losurdo *et al.* "An inverted pendulum preisolator stage for the VIRGO suspension system" G. Losurdo *Rev. Sci. Instr.* vol.72 p.3653, 2001.
- [23] F. Acernese *et al.* "First locking of the Virgo central area interferometer with suspension hierarchical control" *Astroparticle Physics* vol.20, pp.629640, 2004.
- [24] H. Tariq *et al.* "The linear variable differential transformer (LVDT) position sensor for gravitational wave interferometer low-frequency controls" *Nuc. Instr. and Meth. A* vol.489, pp.570-576, 2002.
- [25] G. Persichetti, A. Chiummo, F. Acernese, F. Barone, R. De Rosa, F. Garufi, L. Milano, S. Mosca "Model Independent Numerical Procedure for the Diagonalization of a Multiple Input Multiple Output Dynamic System" *Real Time Conference, 17th IEEE-NPSS Conference Proceedings* (2010).

- [26] J. Liu, L. Ju and D. G. Blair *Phys. Lett. A* 228 234-249 (1997)
- [27] R. De Rosa, F. Garufi, L. Milano, S. Mosca, G. Persichetti "Characterization of electrostatic actuators for suspended mirror control with modulated bias" *J. Phys.: Conf. Ser.* 228 012018 (2010).
- [28] F. Acernese, F. Barone, R. De Rosa, L. Milano, K. Qipiani, and F. Silvestri "Digital control system for mechanical damping of suspended mass" *Proc. SPIE* vol.5052, 451, 2003.
- [29] C. Wang, H. Tariq, R. DeSalvo, Y. Iida, S. Marka, Y. Nishi, V. Sannibale, A. Takamori "Constant force actuator for gravitational wave detectors seismic attenuation systems (SAS)" *Nuclear Instruments and Methods in Physics Research A* 489, 563569, 2002
- [30] G. Losurdo, et al. "Inertial control of the mirror suspensions of the VIRGO interferometer for gravitational wave detection" *Rev. Sci. Instrum.* vol.72, pp.3653-3661 ,2001.
- [31] A. Gennai, S. Mancini, T. Maiani, and D. Passuello, *VIRGO Internal Report* No. VIR-NOT-PIS-1390-101, 1997.
- [32] G. Losurdo, *Ph.D. thesis, Scuola Normale Superiore, Pisa, 1998;*  
<http://www.virgo.infn.it/documents/ftpvirgo/archive/thesis/dottlosurdo.ps>.
- [33] E. S. Fergusson *US Nat. Museum Bull.*, No. 228, p. 185 (1962).
- [34] A. Bertolini et al. *Nuclear Instrument and Method*, No. 556, p. 616 (2006).
- [35] J. Liu *PhD Thesis*, University of Western Australia , (2000).
- [36] F. Acernese ,R. De Rosa, G. Giordano, R. Romano and F. Barone "Mechanical Monolithic Sensor for low frequency seismic noise measurement" *Proc. SPIE* Vol 6529 65292B-1 (2007).
- [37] F. Acernese, R. De Rosa, G. Giordano, R. Romano and F. Barone "Mechanical monolithic accelerometer for suspension inertial damping and low frequency seismic noise measurements" *J. Phys.: Conf. Ser.* 122 012012 (2008).
- [38] G. Giordano *Ph.D. thesis, Scuola di Dottorato in Rischio Sismico, Napoli, 2008.*
- [39] Comsol<sup>©</sup> Multiphysics user's Guide (2007).

- [40] Y. M. Tseytlin "Notch flexure hinges: an effective theory" *Rev. Sci. Instrum.* Vol. 73, No. 9, pp. 3363-3368 (2002).
- [41] C. M. Wu et al. *Metrologia* 33 533 (1996).
- [42] D. István *Measurement* 37 95 (2005).
- [43] P. R. Saulson, *Phys. Rev. D* 42, 2437 (1990).
- [44] Y. Nakayama et al., *Performances test of STS-2 seismometers with various data loggers*, in proceedings of IWAA2004, CERN, Geneva, 4-7 October (2004).
- [45] A. Bertolini et al. *Nuclear Instruments and Methods in Physics Research A* 564 pp.579586 (2006).
- [46] J. Berger, P. Davis, *Ambient Earth Noise: A Survey of the Global Seismographic Network, in 2005 IRIR 5-Year Proposal*, 38 (2005).
- [47] G. Persichetti, F. Acernese, R. De Rosa, G. Giordano, R. Romano, S. Vilasi, F. Barone "A New Architecture for the Implementation of Force-Feedback Tunable Mechanical Monolithic Horizontal Sensor" *Real Time Conference, 17th IEEE-NPSS Conference Proceedings* (2010).
- [48] P. Amico et al. "Mechanical quality factor of mirror substrates for VIRGO" *Class. Quant. Grav.* 19 1663-1668 (2002).
- [49] I. Fiori et al. "Magnetic Noise Coupling", *Noise Meeting* 29 Sept 2005.
- [50] L. Holloway, et al. "A coil system for virgo providing a uniform gradient magnet field. *Physics Letters A*, 171 pp.162-166, (1992).
- [51] V. P. Mitrofanov, N. A. Styazhkina, and K. V. Tokmakov. "Relation between mechanical barkhausen noise and magnetomechanical internal friction" *Journal De Physique* 12 C8407C8412 (1987).
- [52] H. Sakamoto, M. Okada, and M. Homma "Theoretical analysis of barkhausen noise in carbon steels" *IEEE Transactions on Magnetism* 23 pp.22362238 (1987).
- [53] S. Grasso et al "Electrostatic systems for fine control of mirror orientation in interferometric GW antennas" *Physics Letters A* 244 pp.360-370 (1998).
- [54] I. Ricciardi *Ph.D. thesis, Scuola di Dottorato in Rischio Sismico, Napoli*, (2006).

- [55] R. Weiss. Note on Electrostatics in the LIGO Suspensions. *LIGO document* T960137-00-E (1996).
- [56] V.B. Braginsky, O.G. Ryazhskaya, S.P. Vyatchanin. Notes about Noise in Gravitational Wave Antennae Created by Cosmic Rays. *LIGO document* G050457-00-R (2005).
- [57] V.P. Mitrofanov, L.G. Prokhorov, and K.V. Tokmakov. Variation of electric charge on prototype of fused silica test mass of gravitational wave antenna. *Phys. Lett. A* 300, 370 (2002).
- [58] M. J. Mortonson, C. C. Vassiliou, D. J. Ottaway, D. H. Shoemaker, and G. M. Harrya, *Rev. Scientific Instruments* 74 4840 (2004).
- [59] M. Hewitson, K. Danzmann, H. Grote, S. Hild, J. Hough, H. Luck, S. Rowan, J.R. Smith, K.A. Strain and B. Willke, *Class. Quantum Grav.* 24 6379 (2007).
- [60] S. Mosca *Ph.D. thesis, Scuola di Dottorato in Fisica Fondamentale ed Applicata*, Napoli, (2009).